Structure-function relationships of molybdenum-based oxide nitrides as model catalysts in selective oxidation of propene

vorgelegt von

Diplom-Chemiker

Sven Kühn

geb. in Berlin

Von der Fakultät II - Mathematik und Naturwissenschaften

der Technischen Universität Berlin

zur Erlangung des akademischen Grades

Doktor der Naturwissenschaften

Dr.rer.nat.

genehmigte Dissertation

Promotionsausschuss:

Vorsitzender: Prof. Dr. rer. nat. Thomas Friedrich

Berichter/Gutachter: Prof. Dr. rer. nat. Thorsten Ressler

Berichter/Gutachter: Prof. Dr. rer. nat. Peter Strauch

Tag der wissenschaftlichen Aussprache: 12. Mai 2016

Berlin 2016

Zusammenfassung

Molybdänoxide sind gut geeignete Modellkatalysatoren für die selektive Oxidation von Propen zu Acrolein. Das Ziel dieser Arbeit war die Erstellung von Beziehungen zwischen katalytischer Aktivität und Sauerstoffmobilität. Dafür wurde das Anionengitter von Molybdänoxiden durch die Substitution von Sauerstoffionen durch Stickstoffionen modifiziert. Basierend auf früheren Untersuchungen sollte die katalytische Aktivität und thermische Stabilität von Molybdänoxidnitriden erhöht werden.

Im ersten Teil der Arbeit wurde kommerziell erhältliches MoO_3 mechanisch in einer Planetenkugelmühle bearbeitet, um die Kristallinität zu verändern. Im Anschluss wurden die Molybdänoxide und die jeweiligen Oxidnitride mittels *ex situ* Methoden untersucht. Diese Untersuchungen ergaben detaillierte Informationen über den Einfluss des Stickstoffeinbaus auf die elektronische Struktur und die elektrischen Eigenschaften. Die optische Bandlücke von MoO_3-Oxidnitriden war deutlich erniedrigt. Der Stickstoffeinbau führte zu einer starken Erhöhung der Leitfähigkeit. Zusätzlich ergaben FTIR- und DR-UV-Vis-Spektroskopie Erkenntnisse über verschiedene Prozesse des Stickstoffeinbaus während der Ammonolyse. Sauerstoffionen wurden hauptsächlich durch NH_X Gruppen substituiert. Untersuchungen der katalytischen Aktivität zeigten einen Einfluss auf die Bildung von Acrolein und CO_X. *In situ* Spektroskopie ermöglichte eine Korrelation zwischen der zunehmenden thermischen Stabilität von MoO_3-Oxidnitriden und der Kristallitgröße, die aus den (0*k*0) Reflexen (XRD) berechnet wurde.

Der zweite Teil der Arbeit behandelte die Modifikation des Anionengitters von $(MoV)_5O_{14}$, welches ein relevanteres System für die selektive Propenoxidation ist. Erstmals wurden Vanadium-Molydbänoxidnitride mit Mo_5O_{14}-Struktur sowie unterschiedlichen Stickstoffgehalten hergestellt. *Ex situ* Untersuchungen ergaben, dass der Stickstoff ohne eine Änderung der mittleren Valenz der Metallzentren eingebaut wurde. Zusätzlich wurde die Bildung von Sauerstoffleerstellen durch Leitfähigkeitsmessungen bekräftigt. Signifikante Unterschiede in den Leitfähigkeiten blieben nach dem Stickstoffausbau erhalten. TPR Experimente zeigten eine erhöhte Verfügbarkeit von Sauerstoff der Mo_5O_{14}-Oxidnitride. Diese verbesserte Verfügbarkeit stand im Zusammenhang mit der verbesserten Leitfähigkeit. Die katalytische Aktivität wurde bei verschiedenen Temperaturen untersucht. Die Selektivität bezüglich Acrolein stieg mit erhöhtem Stickstoffgehalt an, während sich die Bildung von CO_X verringerte.

Abstract

Molybdenum-based oxides represent well-known model catalysts for the selective oxidation of propene to acrolein. The objective of this work was elucidating relationships between catalytic performance and oxygen mobility. Therefore, the anion lattice of molybdenum oxides was modified by substituting oxygen ions with nitrogen ions. On the basis of previous studies the thermal stability and catalytic activity of molybdenum oxide nitrides were improved.

In the first part of this work commercially available MoO_3 was mechanically activated in a planetary mill to vary the crystallinity. Afterwards, ball-milled MoO_3 and its corresponding oxide nitrides were characterized by *ex situ* methods. This characterization yielded a detailed knowledge of the influence of varying crystallinity and incorporation of nitrogen on electronic structure and electrical properties. The optical band gap of MoO_3-type oxide nitrides was significantly decreased compared to corresponding oxides. The incorporation of nitrogen led to a strong increase of conductivity. Additionally, FTIR and DR-UV-Vis spectroscopy revealed different processes of nitrogen incorporation during ammonolysis of MoO_3. Oxygen ions were mainly substituted by NH_X species. Investigations on catalytic performance showed an influence on formation of acrolein and CO_X. *In situ* spectroscopy resulted in a correlation between increasing thermal stability of MoO_3-type oxide nitrides and increasing crystallite size from (0*k*0) reflection peaks (XRD).

The second part of this work deals with the modification of anion lattice of $(MoV)_5O_{14}$ representing a more relevant system for selective propene oxidation. Vanadium-molybdenum oxide nitrides with Mo_5O_{14}-structure and different nitrogen contents were prepared for the first time. *Ex situ* investigations showed that incorporating nitrogen in the structure of Mo_5O_{14} proceeded without changing the average valence of the metal centers. Additionally, impedance spectroscopy corroborated the formation of oxygen vacancies. Significant changes in conductivities remained after removal of nitrogen. TPR measurements were carried out to investigate oxygen mobility. The enhanced reducibility of oxide nitrides was correlated with the increased conductivity. Catalytic performance was studied at various temperatures. Selectivity towards acrolein increased with increasing nitrogen content while formation of CO_X decreased.

Contents

Abbreviations

a.c.	alternating current
AHM	ammonium heptamolybdate
BET	Brunauer-Emmet-Teller
Chap.	Chapter
CPE	constant phase element
d.c.	direct current
DR-UV-VIS	diffuse Reflectance UV-Vis Spectroscopy
e.g.	or example (Latin “exempli gratia”)
EIS	electrochemical impedance spectroscopy
et al.	and others (Latin “et alii”)
EXAFS	extended X-Ray absorption fine structure
FID	flame ionization detector
FIR	far infrared
FT	Fourier transformed
FTIR	Fourier transform infrared spectroscopy
FWHM	full width at half maximum
GC	gas chromatography
HASYLAB	Hamburg Synchrotron Radiation Laboratory
IUPAC	International Union of Pure and Applied Chemistry
IVCT	intervalence charge transfer
KM	Kubelka-Munk
LMCT	ligand to metal charge transfer
m/e	mass-charge ratio
MIR	mid infrared
MLCT	metal to ligand charge transfer

MS	mass spectrometry
PSD	position-sensitive-detector
RT	room temperature
SKM	Schuster-Kubelka-Munk
SLA	single-line analysis
TCD	thermal conductivity detector
TGA	thermogravimetric analysis
TPR	temperature-programmed reduction
UV	ultraviolet
Vis	visible
WH	Williamson-Hall
wt.%	weight percent
XAFS	X-ray absorption fine structure
XANES	X-ray absorption near edge structure
XAS	X-ray absorption spectroscopy
XRD	X-ray diffraction

1 Introduction

1.1 Motivation

The chemical industry is the third largest industry in Germany. With an annual sales of 184 billion Euro this corresponds to the largest chemical industry in the European Union [1]. Approximately 90% of all chemical processes uses catalysts [2]. Selective oxidation processes like the functionalization of hydrocarbons represent one of the largest segments of modern chemical industry. None of these reactions run at maximum selectivity due to the formation of unwanted by-products. Hence, an improvement in selectivity of only one percentage might be associated with a considerable increase in profit. This improvement might be achieved by the development of new catalysts. Selective oxidation of propene to acrolein is such an important reaction which is processed with conversion of propene over 90% and a selectivity of 80-85% [3]. Acrolein is a raw material for synthesis of acrylic acid which is an important fine chemical for production of superabsorbent for hygiene materials [4].

In the last years the application of *in situ* analytical methods has become a powerful tool to obtain a detailed understanding of the function of a heterogeneous catalyst. With the help of this knowledge the structure or properties like conductivity of a catalyst can be related to its catalytic activity. Hence, determining the important factors for activity and selectivity by elucidating structure-function relationships can result in a rational design of improved catalysts [5–7]. Compared to classical trial-and-error approach the rational catalyst design constitutes an alternate approach for the development of new or improved catalytic systems. A combination of analytical techniques might lead to these structure-function relationships. Therefore, structure analytical methods can be combined with analysis of product gas phase. Hence, the combination of complementary techniques is one of the main challenges in the research of heterogonous catalysis to compare the characterization results under reaction conditions [8].

Most industrial processes using heterogeneous catalysts are carried out over polycrystalline catalysts [9]. Many of these catalysts consist of several cooperating phases.

Industrial catalysts exhibit a high chemical and structural complexity. Hence, the impact of single structural motifs or bulk properties on functionality can hardly be determined. Simplification of complex catalysts can lead to deeper insight in structure-function relationships. The simplified model catalyst systems exhibit reduced complexity. The industrial selective oxidation of propene to acrolein proceeds over a Mo-Bi-Fe-O catalyst while a Mo-V-O catalyst is used for the following oxidation to acrylic acid [10]. Thus, it seems plausible that molybdenum based oxides represent a simple approach to create such model systems. Indeed, MoO_3 is a well-investigated model system for selective oxidation of propene [11–13]. Model catalysts can be developed by preparing highly dispersed metal oxides on a support material to obtain local structural motifs and a high surface area. Otherwise, the influence of typical bulk properties as the role of lattice oxygen is still unraveled [14]. However, the importance of bulk diffusion of oxide ions is expected to be a crucial factor for the design of new industrial catalysts [15]. It is obvious that these characteristics or the evolution of bulk defects of a catalyst are not available by the use of supported model catalysts. Therefore, bulk structural investigations of model catalysts under reaction conditions represent a further necessity to obtain a detailed knowledge of the structure and defects. These studies might promote the rational design of catalysts by elucidating structure-function relationships in cooperation with investigations of supported metal oxides [16].

1.2 Molybdenum oxide catalysts in selective oxidation of propene to acrolein

It is assumed that selective oxidation of propene to acrolein proceeds according to a redox mechanism ("Mars-van-Krevelen mechanism", **Figure 1-1**) [17]. In a first step propene is adsorbed at the surface of MoO_3 on coordinately unsaturated Mo sites. After adsorption of propene the hydrogen atom in α-position to the double bond is abstracted. An allylic intermediate is formed by this abstraction. Afterwards, nucleophilic attack of lattice oxygen ions O^{2-} on the (010) planes result in formation of σ bond between lattice oxygen and the allylic intermediate. After insertion of the nucleophilic lattice oxygen into the hydrocarbon the formed oxygenated product desorbs. In the last step of the catalytic cycle the catalyst is re-oxidized by gas-phase oxygen. The re-oxidation of the catalyst can

occur at a different reactive site of the catalyst. It is suggested that bulk oxygen diffusion might play an important role for catalytic activity [11,14,18].

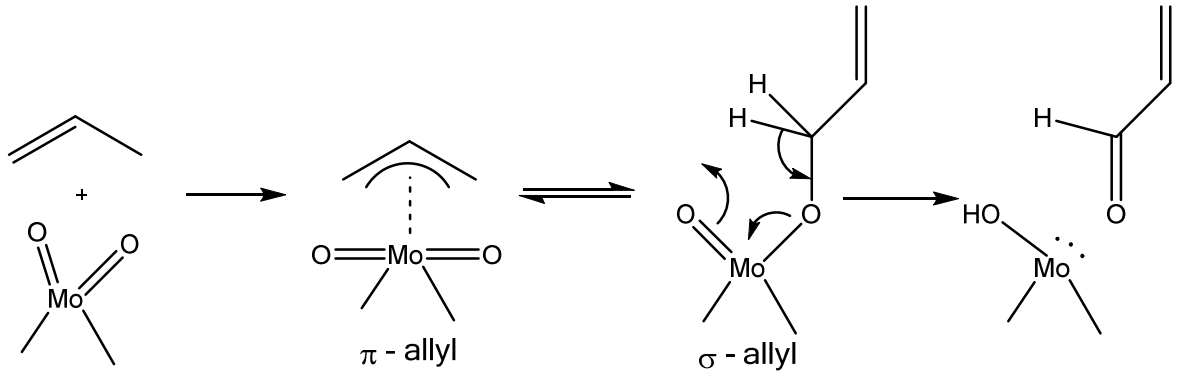

Figure 1-1: *Schematic presentation of selective oxidation of propene to acrolein over a molybdenum oxide based catalyst [13].*

Several different bulk model catalysts for selective oxidation of propene are known from the literature [19–21]. The reduced chemical and structural complexity of binary oxides like α-MoO_3 make them the most simple model system for elucidating structure-activity correlations. Orthorhombic α-MoO_3 (*Pbnm*) is the stable modification of MoO_3 at room temperature [22]. The Mo cations are coordinated by six oxygen anions. Those distorted octahedrons are arranged corner- and edge-sharing in layers along the *b*-axis. The layers are linked by van-der-Waals forces. The distorted octahedrons are due to different Mo-O distances between 1.67 Å and 2.33 Å [23]. In addition, a monoclinic and a hexagonal modification of MoO_3 exist.

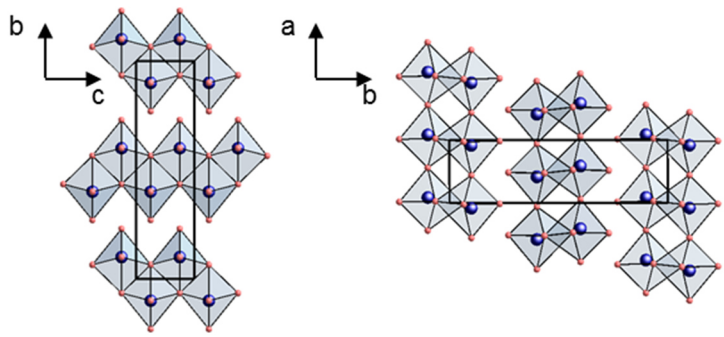

Figure 1-2: *View on the bc and ab plane of α-MoO_3 indicating the connections of MoO_6 octahedrons and evolution of layered structure.*

Model catalysts with Mo_5O_{14} structure represent more complicated model system compared to MoO_3. The Mo_5O_{14} exhibit an increased structural complexity. The tetragonal Mo_5O_{14} structure is depicted in **Figure 1-3** as a network of MoO_6 octahedrons and MoO_7 pentagonal bipyramids (*P4/mbm*) [24]. Each bipyramid shares edges with five octahedrons. These cluster of bipyramids and octahedrons are linked by additional corner sharing octahedrons. Along the *c*-axis the polyhedrons are stacked on the top. The respective polyhedrons share its corners forming a three-dimensional tunnel structure with five- and sixfold channels [25]. Different metal cation are used for stabilizing the tunnel structure of Mo_5O_{14} by partial substitution (e.g. vanadium [26], tungsten [27], niobium [28], titanium [29], tantalum [25]). Multiple substitutions by different cations can lead to Mo_5O_{14} structure which represents an important structural motive for heterogeneous catalysts. Depending on the type of substitution the molybdenum based oxide can be applied for many reactions [30].

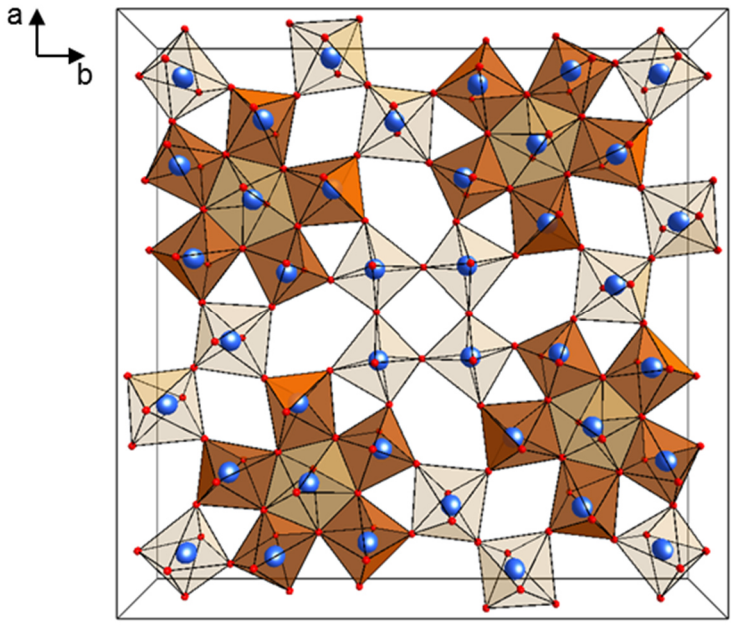

Figure 1-3: *View on the ab-plane of Mo_5O_{14} structure. Different characteristic structural motifs are marked.*

The addition of tellurium and niobium to a molybdenum oxide based catalyst can lead to highly active M1 phase (**Figure 1-4**). The structure of M1 is related to that of Mo_5O_{14}. It consists of a polygon network of MO_6 (M = Mo, V) octahedral and NbO_7 pentagonal bipyramids. Hexagonal and heptagonal channels are formed into layers in the *ab*-plane

which are partially filled with TeO units [31,32]. Despite the high catalytic activity and selectivity of the M1 phase the increased complexity of the structure represents a challenge for fundamental studies on structure-function relationships.

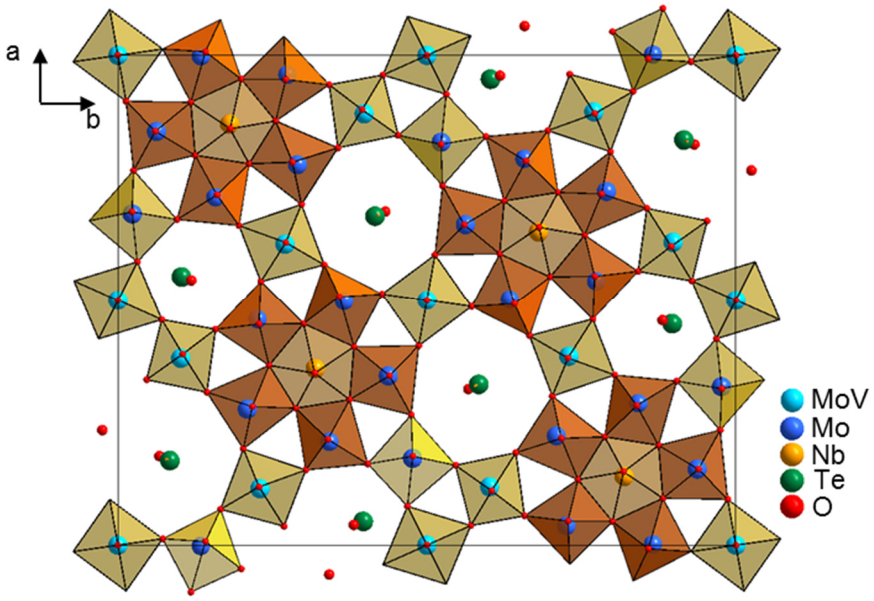

Figure 1-4: *Schematic presentation of the M1 phase by a view on ab plane. Characteristic structural motifs including similar structural motifs of Mo_5O_{14} are indicated.*

1.3 Oxygen mobility of molybdenum oxides in selective oxidation reactions

α-MoO_3 is one of the best investigated model systems for selective oxidation of propene due to its less complicated structure compared to industrial catalysts. Former isotope exchange experiments of α-$Mo^{16}O_3$ and $^{18}O_2$ showed that lattice oxygen is involved in selective oxidation of propene to acrolein [33,34]. The loss of oxygen from MoO_3 was suggested to lead to an Mo-Mo bond across the oxygen vacancy [14]. Further investigations of the defect structure of α-MoO_3 under propene oxidation conditions revealed a slightly decreased average Mo valence which might be attributed to the formation of share-structural defects [16,35]. The $Mo_{18}O_{52}$-type structure represents a suitable reference for formed shear defects. Additionally, after selective oxidation of the reactant with nucleophilic lattice oxygen the resulting oxygen vacancy might not be re-oxidized immediately at the active site of the catalyst [33]. For re-oxidation the oxygen

vacancy migrates towards re-oxidation site where dioxygen is adsorbed at the surface. Adsorbed dioxygen is transferred into O^{2-} and incorporated in the catalyst to fill the oxygen vacancy (**Figure 1-5**). The required four electrons are given by the solid [36]. Hence, conductivity might be an important parameter for investigations on the electron transfer. The intermediate formed oxygen species O^- have strong electrophilic character which might be responsible for conversion of propene to total oxidation products CO_x [18]. The role of lattice oxygen and redox properties of the catalyst represent two of seven important principles for selective oxidation proposed by Grasselli [33]. Subsequently, diffusion of oxygen vacancies and mobility of lattice oxygen is expected to play an important role for catalytic performance.

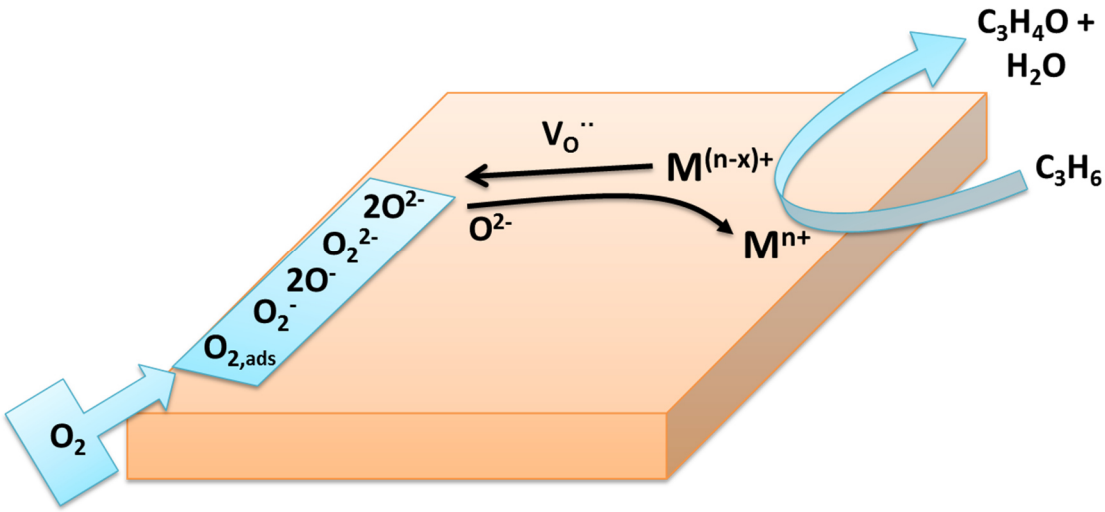

Figure 1-5: *Schematic presentation of redox mechanism ("Mars-van-Krevelen") for selective oxidation of propene to acrolein (adapted from [3,33]). After the reduction of metal oxide the oxygen vacancy migrates to re-oxidation site of the catalyst to be replenished oxygen.*

MoO_3 is well-known for its structure sensitivity in selective oxidation reactions. Crystals with specific orientations exhibited a significant dependence of catalytic performance on the ratio of (100) and (010) faces in MoO_3. Acrolein was formed on (100) lateral plane while formation of total oxidation products CO_X occurred at (010) basal plane. Hence, the type of products of selective oxidation of propene is strongly dependent on the habit of crystallites. Haber related this dependence to electrophilic and nucleophilic oxygen species forming oxidation products [37]. A similar type of structure

sensitivity was also observed for selective oxidation of methanol to formaldehyde and ethanol to acetaldehyde [38].

With respect to suitable model systems for elucidating the effect of oxygen mobility on catalytic performance it is desirable to preserve the crystallographic structure of the catalyst. Different crystallographic structures might exhibit different catalytic performances particularly with regard to structure sensitivity of MoO_3 [21]. An additional possibility to modify oxygen mobility constitutes the formation of oxygen vacancies with preserved crystallographic structure [39]. Cation substitution is an effective method for generating oxygen vacancies. Oxygen vacancies can be formed in zirconium dioxide by doping with calcium oxide. Hence, this method might lead to a variation of density of vacancies and diffusibility of oxygen ions. Molybdenum oxides might be doped with other transition metals like tungsten, niobium or vanadium. However, addition of these transition metals to molybdenum oxides can lead to various structures. Additionally, the oxides of these transition metals are also active in selective oxidation reaction of light alkenes. The catalytic performance of molybdenum oxides might also be affected by addition of tungsten, niobium or vanadium [20,40,41]. Therefore, modification of the cation lattice to modify oxygen mobility with preserved crystallographic structure seems to be less suited.

The modification of the anion lattice by incorporation of nitrogen represents an alternate method for generating oxygen vacancies [42]. Oxide nitrides are suitable model systems for studies on heterogeneous catalysts. Zirconium oxide nitrides, for instance, have been shown to be active catalysts for ammonia decomposition [43]. N-doped TiO_2 represents a widely investigated model system for photocatalytic reactions due to changed optical and electronic properties [44,45]. Often the incorporation of nitrogen is accompanied by a preservation of crystallographic structure [46]. Recent studies have shown that nitrogen can be incorporated in the anion lattice of α-MoO_3 without changing the crystallographic structure [47]. Resulting oxide nitrides represent suitable model system for studying correlations between oxygen mobility and catalytic performance [48]. Mild ammonolysis resulted in a much improved reducibility which can be attributed to an increased oxygen mobility. In addition, the corresponding oxide nitrides of α-MoO_3 exhibited an enhanced electronic conductivity [49]. The increased conductivity led to

significantly improved capability retention during first time investigations as anode material for lithium ion batteries [50]. However, correlations between catalytic performance and electrical properties could not be elucidated because of the low thermal stability of the corresponding oxide nitrides. Furthermore, MoO_3 is not the most relevant system for studies on selective oxidation of propene due to its low catalytic activity and selectivity towards acrolein. Hence, possible influences of electrical properties on catalytic performance could not be determined.

1.4 Outline of the work

The objective of this work was enhancing the usage of molybdenum oxide nitrides as a model catalyst for selective oxidation of propene. Therefore, the thermal stability and catalytic activity of molybdenum oxide nitrides have to be improved. Based on previous studies two approaches were developed to elucidate relationships between catalytic performance and oxygen mobility. On the one hand commercially available MoO_3 was mechanically activated by treatment in a planetary mill to vary the crystallite size. Mechanical activation seems to be a promising approach due to the structure sensitivity of MoO_3 in selective oxidation of propene. Afterwards, the investigations of ball-milled MoO_3 and its corresponding oxide nitrides focused on determination of crystallinity. In addition, the variation of crystallinity should be correlated with changes in electronic structure and properties (**Chap. 3**). The reducibility was determined as one crucial property changed by incorporation of nitrogen. Hence, **Chap. 4** deals with the impact of ball-milling and subsequent ammonolysis on reducibility. Investigations of their catalytic properties together with *in situ* characterization were carried out with a focus on thermal stability of MoO_3-type oxide nitrides (**Chap. 5**). The second approach included the extension of range of oxide nitrides to more relevant structures in propene oxidation. Model catalysts with the Mo_5O_{14}-structure constitute more complex systems compared to MoO_3. The preparation and structural characterization of (MoV) oxide nitrides with Mo_5O_{14}-structure are presented. Consequently, the structure of Mo_5O_{14}-type oxide nitrides was characterized in detail by different methods to analyze influences of nitrogen incorporation on long-range and short-range structure. The structural characterization also aimed at studies on compensation of additional negative charge of nitrogen ions

compared to oxygen ions. Furthermore, effects of ammonolysis of mixed molybdenum oxides on oxygen mobility and catalytic performance in selective oxidation of propene were studied (**Chap. 6** and **Chap. 7**). Apart from these effects, a particular focus was placed on thermal stability of Mo_5O_{14}-type oxide nitrides using complementary *in situ* analytical methods.

2 Characterization methods

2.1 X-ray diffraction (XRD)

Investigations on bulk materials used as heterogeneous catalysts are often carried out by X-ray powder diffraction (XRD). In addition to determining crystal structure XRD provides the possibility to characterize disorder in materials which might influence catalytic properties of materials [51,52]. XRD is based on elastic scattering of X-ray photons from the electron bound to atoms. The intensity of scattered X-rays is measured as a function of the diffraction angle. The phenomenon of X-ray diffraction can be described by the Bragg equation establishing a relationship between the lattice plane spacing *d*, and the angle θ between incident X-rays and the lattice plane [53]:

$$n\lambda = 2d_{hkl} \cdot sin\theta. \tag{2-1}$$

Sharp intensity maxima only occur at special angles where **eq. (2-1)** is fulfilled and X-ray photons interfere constructively. The lattice planes are characterized by the Miller indices *hkl*. Hence, each diffraction peak is described by an index triplet *hkl* according to the Bragg relationship.

The profile of diffraction peaks (FWHM and peak shape) contains information about the real structure of the sample. Crystallite size as well as lattice strain cause broadening of diffraction peaks. In reciprocal space the diffraction conditions are defined as a geometrical relation (**Figure 2-1**). The scattering vector $\underline{d}^*$ is created by the vectors of incident and diffracted X-rays $\underline{\nu_0}$ and $\underline{\nu}$. Diffraction takes place when scattering vector $\underline{d}^*$ connects its origin with another (*hkl*) point. For an ideal and infinite crystal the diffracted intensity is almost confined to a small region around each point in reciprocal space and results in small FWHM due to instrumental effects. In contrast crystallite domains of real samples have a finite extension. Thus, the length of scattering vector varies for each diffraction peak depending on the crystallite size. Hence, diffraction can take place at slightly varied diffraction angles resulting in line broadening of the diffraction peak.

Most crystalline samples contain distortions caused by imperfections of the periodic crystal structure. The profile of the diffraction peak can be influenced in different ways by

lattice strain. On the one hand a macroscopically homogenous strain results in a shift of diffraction peaks. Introducing this type of strain expressed by $\varepsilon = \Delta d/d$ in the differentiated Bragg equation results in

$$\Delta 2\theta = -2\varepsilon \cdot tan\theta. \tag{2-2}$$

On the other hand an inhomogeneous lattice strain causes a broadening of observed diffraction peaks. In this case the incident X-ray beam is diffracted at slightly different angles. It is also possible that both kind of strain can be observed in a sample. Different methods of determining size and strain are explained below.

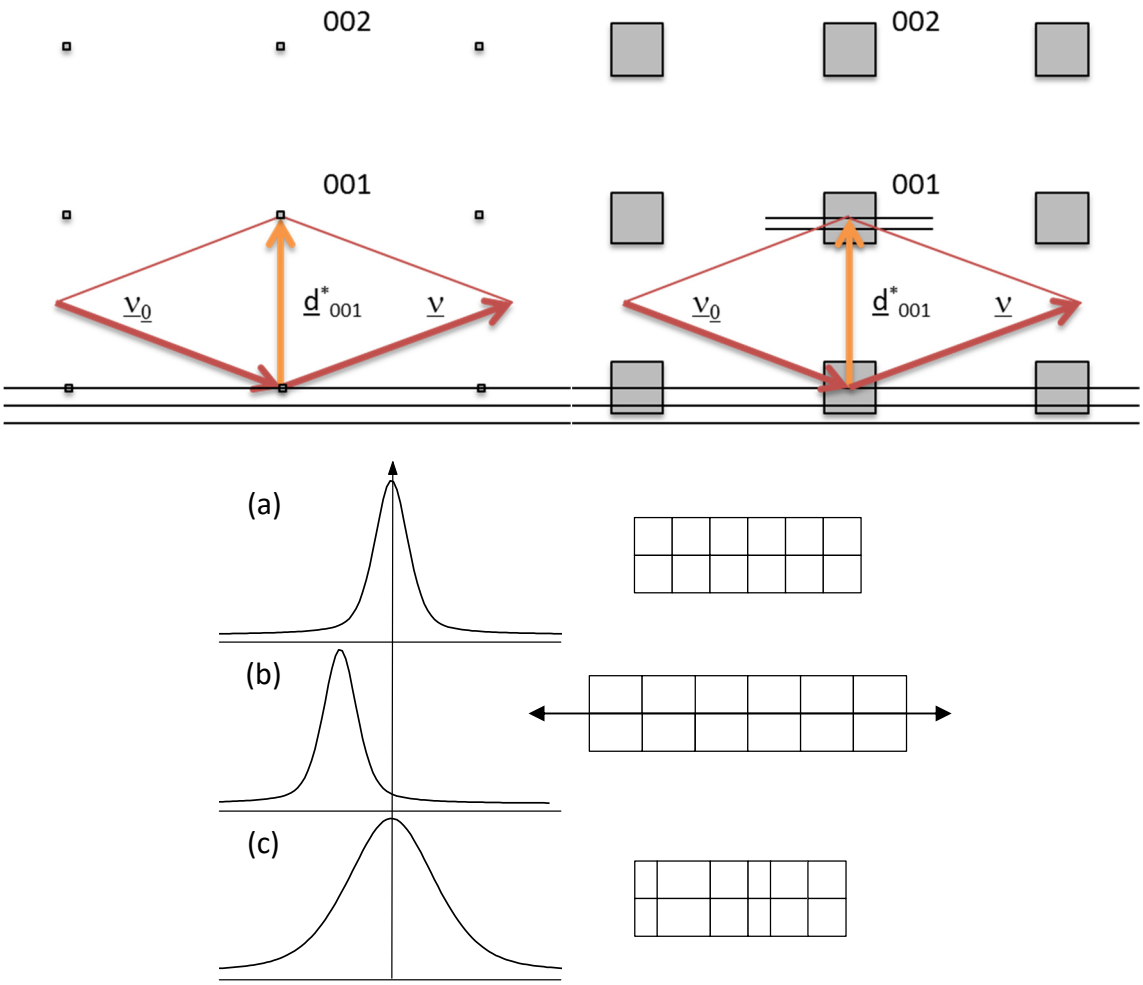

Figure 2-1: *Top: Schematic representation of (001) diffraction condition in reciprocal space for a perfect crystal (left) and for crystatalline domains (right). Bottom: XRD peak profile for zero strain (a), macrostrain (b), microstrain (c)* [51].

2.2 X-ray absorption spectroscopy (XAS)

X-ray absorption spectroscopy (XAS) is often used in heterogeneous catalysis because it allows the analysis of the local structure around an absorber atom [54]. Therefore a long-range structure of the catalyst is not required. For crystalline solids XAS represents a complementary method for X-ray diffraction to analyze the structure of a catalyst [55,56]. The sample is placed between two ion chambers and illuminated by an X-ray beam. The ion chambers measure the intensity of the X-ray beam before and after transmitting the sample. After passing the sample the intensity of the incident X-ray beam (I_0) is attenuated according to Lambert's law:

$$I = I_0 exp(-\mu d). \tag{2-3}$$

The decrease of intensity of X-ray beam depends on the thickness of the sample *d* and the linear absorption coefficient μ referring to the type of atoms and the density of a material. Reaching the binding energy of a core-electron a step-increase in absorbance occurs, the so called absorption edge. The electron is excited to an empty state above the Fermi level. The absorption edge is denoted by the order of increasing energy as K, L_I, L_{II} or L_{III}. This denotation corresponds to the ground stated of the electron 1s, 2s, $2p_{1/2}$, $2p_{3/2}$.

The XAS spectra can be subdivided in two regions. The part within about 50 eV of the absorption edge is called X-ray absorption near-edge spectrum (XANES) followed by the extended X-Ray absorption fine structure (EXAFS) at higher energies. **Figure 2-2** shows a schematic representation of processes in XANES and EXAFS region of an X-ray absorption spectrum. XANES spectra contain information about the electronic structure as the oxidation state and site symmetry of metal centers. XANES is based on the excitation of an electron from a core level to an unoccupied state close to the Fermi level. Transitions from s orbital to higher p orbital around the K edge or from p orbitals to d orbitals around the L edges are can occur. These transitions obey required selection rules: $\Delta l = \pm 1$, $\Delta j = \pm 1$, $\Delta s = 0$ [57]. Dipole transitions of electrons of the 1s orbital are forbidden for centrosymmetric configurations. Hence, only absorption centers in non-centrosymmetric coordination show intense pre-edge features. Such non-centrosymmetric coordinations

are tetrahedral geometry or distorted octahedral structures. The so-called “fingerprint” region of the XANES spectra after the absorption edge can be interpreted with the help of a set of reference spectra. This fingerprint region is due to transitions to higher unoccupied state or multiple scattering effects of the photoelectron by the first coordination shell.

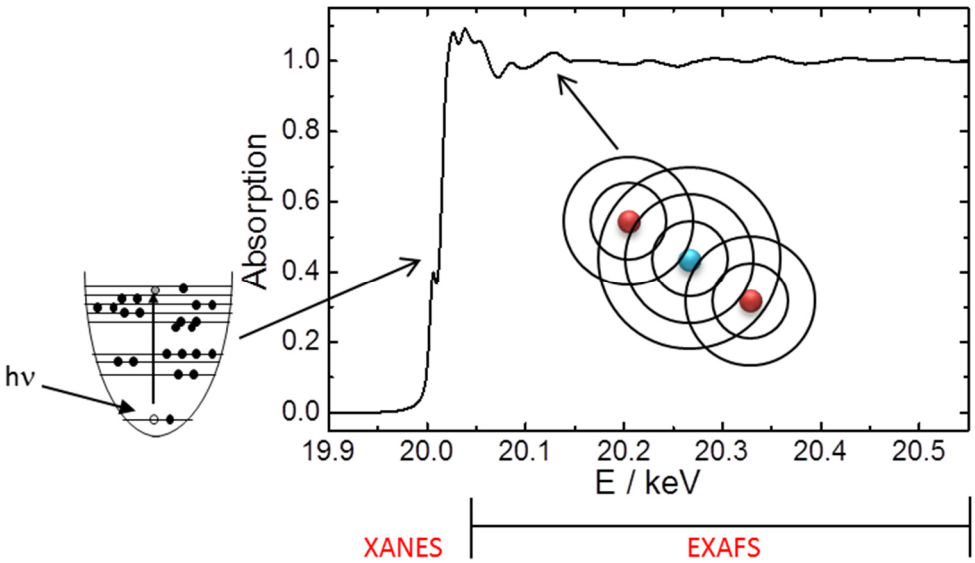

Figure 2-2: *Schematic representation of X-ray absorption spectrum with processes at the absorption edge. In the XANES region an electron is excited to a higher unoccupied state while the scattering of a photoelectron at neighboring atoms results in the EXAFS region.*

The oscillations of the absorption coefficient in the EXAFS region are caused by scattering of a photoelectron at neighboring atoms. The photoelectron from the absorber atom interacts with the electron density of neighboring atoms. The outgoing photoelectron wave is scattered back when reaching a neighboring atom. Hence, the incoming electron waves interfere with the outgoing photoelectron wave of the absorber atom. This interference results in an oscillating absorption coefficient and fine structure of the spectrum. The resulting spectrum is the sum of the contributions of all absorbing sites and backscattering neighbors. The EXAFS modulations can be described by the EXAFS function $\chi(k)$ as a function of wavenumber k:

$$\chi(k) = \sum_{j=1}^{i} A_j(k) \sin\left(2kR_j + \varphi_j(k)\right) \tag{2-4}$$

The EXAFS function represents a single scattering plane-wave approximation [58]. The amplitude of each scattering contribution $A_j(k)$ is given by

$$A_j(k) = N_j \frac{s_0^2(k) exp\left(-2R_j/\lambda(k)\right)}{kR_j^2} e^{-2k^2\sigma_j^2} F_j(k) \tag{2-5}$$

where S_0^2 describes a correction for relaxation processes in the absorber atom, σ^2 is the disorder parameter describing the mean-squared displacement of atoms, and $F_j(k)$ is the backscattering amplitude in the jth shell. The intensity decreases with the distance R_j. The term N_j refers to the number of atoms. The Fourier transformed $\chi(k)$ contains information corresponds to a pseudo radial function between the absorbing atom and near atoms in a range limit of 4-5 Å [59]. The transform is usually multiplied by k^1 or k^3 to emphasize light or heavy atoms. Theoretical scattering paths can be calculated from suitable theoretical models by software programs like FEFF. The theoretical parameters of the scattering paths can be refined to experimental data. Thus, information about the coordination number, disorder parameters and distance determined from the $FT(\chi(k))$.

2.3 Electrochemical impedance spectroscopy (EIS)

Electrochemical impedance spectroscopy (EIS) is a well-established method for investigating electrochemical processes and determining electrical conductivity of samples [60]. Additionally, results of EIS measurements are of interest in characterizing heterogeneous catalysts especially in selective oxidation reactions [61].

Electrical impedance is the ratio of voltage and current in an a.c. circuit. If a current signal is measured as the response to an alternating voltage signal the impedance can be expressed in terms of a magnitude Z_A and a phase shift ϕ.

$$Z = \frac{V(t)}{I(t)} = Z_A \frac{\sin(\omega t)}{\sin(\omega t + \phi)}. \tag{2-6}$$

According to Euler's relationship impedance can also be expressed as a complex function. Hence, the impedance is represented as a complex number i.e. a combination of real (*Z'*) and imaginary (*Z''*) part:

$$Z = Z_A e^{j\phi} = Z_A(\cos\phi + j\sin\phi) = Z' + jZ''. \tag{2-7}$$

Experimental data of impedance measurements can be approximated by the impedance of an equivalent circuit consisting of different circuit elements [62,63]. An overview of often used circuit elements is given in **Table 2-1**. The ohmic resistance is independent of frequency while capacitor and inductor only influence the imaginary part. However, real samples often exhibited inhomogeneities which might lead to differences from ideal capacitors in equivalent circuit. These non-ideal capacitors can be described by a constant-phase element (*CPE*). The phase angle of a *CPE* is ac frequency independent. The deviation of ideal capacitor is given by exponent α. For the case of α = 1 the *CPE* is a pure capacitor.

Table 2-1: *Overview of basic elements for equivalent circuits in EIS [63].*

Component	Resistance	Capacitor	Inductor	Constant phase element
Impedance	$Z = R$	$Z = (j\omega C)^{-1}$	$Z = j\omega L$	$Z = (Q(j\omega)^{\alpha})^{-1}$
Nyquist plot	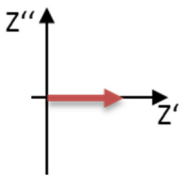	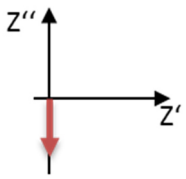	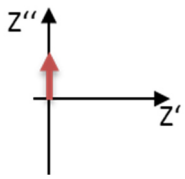	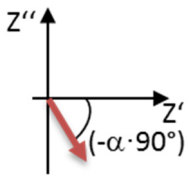
Phase angle	$\phi = 0°$	$\phi = -90°$	$\phi = 90°$	$\phi = (-\alpha \cdot 90°)$

An often used equivalent circuit and its schematic Nyquist-plot is shown in **Figure 2-3**. According to Kirchhoff's law the impedance of a series arrangement is the sum of single impedances. The impedance of a parallel arrangement is given by the sum of the inverse single impedances. Hence, resistance R_1 is frequency independent while the parallel *RC* arrangement results in semicircle. The impedance of equivalent circuit can be expressed by

$$Z(\omega) = R_1 + \left(\frac{R_2}{1 + jR_2\omega C}\right). \tag{2-8}$$

Nyquist presentation is the simplest way to determine the required equivalent circuit and resistances. Nevertheless, the information about frequency is lost. The Bode plot is an alternate presentation containing frequency information by plotting $|Z|$ and ϕ as a function of lg(ω).

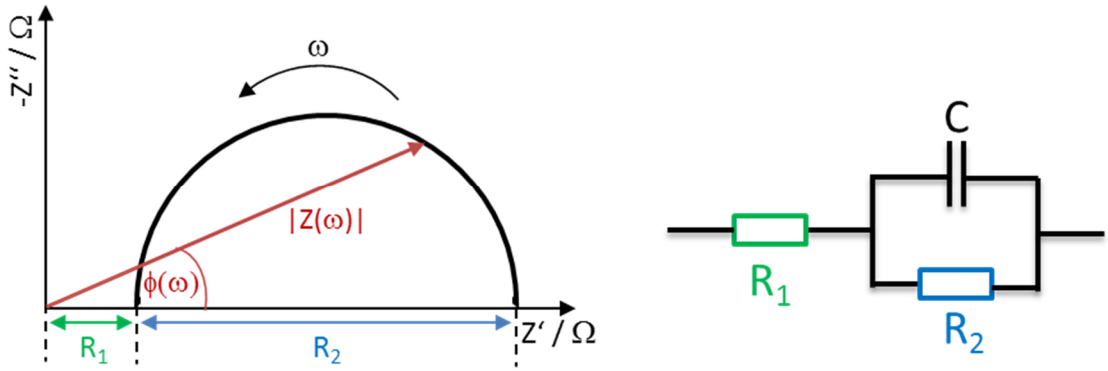

Figure 2-3: *Left: Schematic Nyquist-plot for parallel RC circuit with series resistor. Right: Equivalent circuit for shown Nyquist-plot.*

2.4 Diffuse Reflectance UV-Vis Spectroscopy (DR-UV-VIS)

Spectroscopy in the ultraviolet (UV) and visible (Vis) region of the electromagnetic spectrum is a widely used technique for characterization of heterogonous catalysts [64]. Investigations on electronic transitions such as ligand to metal (LMCT), metal to ligand (MLCT) charge transfer or d-d transitions can be carried out. In the case of powdered catalysts it is necessary to use diffuse reflectance instead of transmission spectroscopy. Theory of this method is discussed in detail by Kortüm [65]. Besides the diffuse reflection of light, several other processes like multiple scattering or total reflection occur. The Schuster-Kubelka-Munk (SKM) theory is an approach to describe the scattered light by two fluxes in opposite direction [66]. According to the SKM approximation the diffuse reflectance is linked to the absorption K and scattering coefficients S via the Kubelka-Munk function $F(R_\infty)$:

$$F(R_\infty) = \frac{(1 - R_\infty)^2}{2R_\infty} = \frac{K}{S}. \tag{2-9}$$

The diffuse reflection R_∞ is calculated from the experimentally, determined reflection of the sample divided by the reflection of a non-absorbing reflectance standard. Materials like MgO, $BaSO_4$ or Spectralon® are often used as reflectance standards. Following requirements have to be fulfilled so that **eq. (2-9)** is valid:

- monochromatic irradiation
- infinite layer thickness
- low concentration of absorbing centers
- homogenous distribution of sample
- absence of fluorescence.

The diffuse scattered light is usually measured using an integrating sphere which is coated with $BaSO_4$. Alternately, a Praying mantis™ reaction chamber can be used for *in situ* experiments. The diffuse reflected light is collected by two ellipsoidal mirrors. The design of Praying Mantis™ leads to high reduction of specular reflection [67].

2.5 Catalytic characterization

Catalytic characterization was performed using a laboratory fixed bed reactor consisting of a SiO_2 tube. Reactants are passed through the catalyst bed. Reaction products can be analyzed by using gas chromatography (GC) and/or mass spectrometry (MS) [68,69]. GC is a common method for separation and quantitative analysis of different components of a mixture [70]. Separation is based on the interaction between two phases in the separation column. One of these phases is the mobile phase consisting of an inert carrier gas. The sample is injected in the mobile phase and transported along the stationary phase in the separation column. Individual components of the sample are temporarily dissolved in the stationary phase or adsorbed at the surface. The detailed intermolecular interactions depend strongly on the chemical properties of the components and the stationary phase. Different strength of interactions of each compound of the sample results in different migration velocities. After passing the separation column at different retention times each component can be analyzed as a discrete signal by a detector. Flame ionization detectors (FID) and thermal conductivity detector (TCD) were used in this work. An overview of additionally widely used detectors

can be found in literature [71]. FID represents a universal detector for carbon containing components with a wide range of linearity and high sensitivity. Molecules of the eluted sample are ionized by an oxyhydrogen flame. The resulting ions and electrons generates a current between the detector electrodes adjacent to the flame [72]. In the TCD the thermal conductivity of the gas mixture and carrier gas reference is measured. Differences in thermal conductivity due to components of the sample are recorded.

2.6 Fourier transform infrared spectroscopy (FTIR)

Fourier transformed infrared spectroscopy (FTIR) was one of the first spectroscopic techniques which found a general acceptance in catalysis. In addition to identifying adsorbed species on the surface of the catalyst, FTIR is useful to identify different phases of the catalyst [57]. Lattice vibrations can be excited by absorption of photons in the middle IR range (400 – 4000 cm^{-1}). Molecules and atoms in solids possess discrete levels of vibrational energy. The potential energy of a vibration can be described by a harmonic oscillator and the corresponding energy levels are given by

$$E = \left(n + \frac{1}{2}\right) h\nu = \left(n + \frac{1}{2}\right) \hbar \sqrt{\frac{k}{\mu}} \tag{2-10}$$

with the force constant of the bond k and the reduced mass μ. Hence, vibrational frequencies increase with increasing bond strength. Different types of vibration can be distinguished, e.g. symmetric or asymmetric stretch vibrations, bending vibrations. However, vibrational transitions only occur if the dipole moment of the molecule changes during the vibration and the vibrational quantum number changes by one unit [73]. Solid samples are often pressed into pellets with KBr or CsI as diluent. The position of vibrational modes in spectra of solids can differ from those of liquid samples due to intermolecular interactions [74].

2.7 X-ray fluorescence spectroscopy (XRF)

X-ray fluorescence spectroscopy (XRF) represents a widely used analysis technique for qualitative and quantitative analysis of metal oxide catalysts. The method is based on the interaction of core shell electrons with X-rays creating characteristic fluorescence radiation for each element. Chemical composition of the sample can be identified by detecting the energy or wavelength of these emitted fluorescence photons. Metal oxide catalysts can be analyzed without being destroyed. Additionally, the procedure is advantageous for elements with high atomic numbers [75,76].

An inner electron is removed from the core shell when the sample is irradiated with X-ray photons. Electrons from a higher energy level fill the hole in the core shell while emitting fluorescence radiation. The emitted energy corresponds to the energy difference of both energy levels and depends on the atomic number of the element. The relationship of the energy and atomic number can be described by Moseley's law

$$E = h\nu = hR_{\nu}(Z-\sigma)^2\left(\frac{1}{n_f^2}-\frac{1}{n_i^2}\right) \tag{2-11}$$

with the Rydberg frequency R_{ν}, Planck constant h, atomic number of the analyzed element Z, a shielding constant σ and the main quantum numbers of the initial and final energy state n_i as well as n_f. The described fluorescence process competes with the so-called Auger process. In this case the released energy when the electron returns to the ground state is transferred to another electron from a higher energy state. Hence, the electron is emitted as an Auger electron. **Figure 2-4** illustrates the different processes which can occur after irradiation with X-rays. The probability of emitting a fluorescence photon or an Auger electron depends on the atomic number of the element. For lighter elements the Auger process primarily occurs.

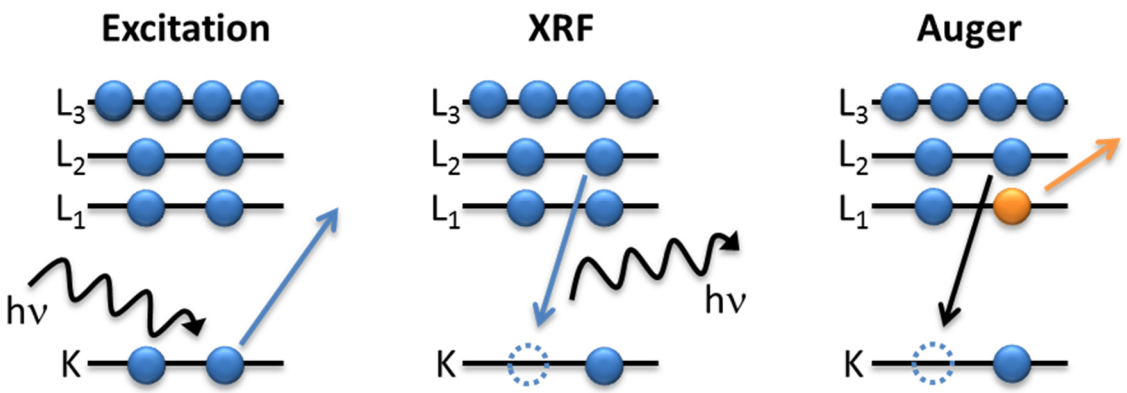

Figure 2-4: *Schematic representation of electron excitation by an X-ray photon (left) and relaxation processes by emitting an X-ray fluorescence photon (middle) or an Auger electron (right)* [77].

2.8 Nitrogen physisorption

Determination of surface area is an important requirement in characterization of catalysts. Nitrogen physisorption represents a technique for determination of surface area of solids. Physisorption denotes an interfacial phenomenon whenever gas (adsorptive) is linked by van der Waals interaction with the surface of a solid (adsorbent). The amount of adsorbed gas *n* can be expressed as a function of the relative equilibrium pressure

$$n = f\left(\frac{p}{p_0}\right)_T \tag{2-12}$$

with saturation pressure of the adsorptive p_0. Resulting isotherms are sectioned into six classes by IUPAC [78]. Only type II is relevant for this work which is typical for non-porous and macroporous materials. An unrestricted monolayer-multilayer transition can be observed. The specific surface area a_{BET} can be calculated by the Brunauer-Emmer-Teller (BET) method from measurements of the isotherms [79]:

$$a_{BET} = n_m N_A \sigma \tag{2-13}$$

Accordingly, the specific surface area can be obtained from the capacity of the monolayer, n_m, the area occupied by the adsorbate molecule, σ, and the Avogadro constant N_A.

3 Preparation and characterization of ball-milled molybdenum oxide and its oxide nitrides

3.1 Introduction

Molybdenum oxide MoO_3 represents a well-known model catalyst for partial oxidation of propene to acrolein [11,16,80]. The reduced chemical and structural complexity of binary oxides like α-MoO_3 makes it the most simple model system for elucidating structure-activity correlations. Recent studies have shown that nitrogen can be incorporated in the anion lattice of α-MoO_3 without changing the crystallographic structure. Resulting oxide nitrides represent suitable model system for studying correlations between oxygen mobility and catalytic performance [48]. However, only little effects on catalytic performance were detected due to low thermal stability of oxide nitrides and catalytic activity of MoO_3.

Ball-milling of orthorhombic α-MoO_3 resulted in changes of crystallite size, defect structure and redox properties [81–84]. Different strong modification of crystallite sizes was determined for various crystallographic orientations. In addition, morphology and crystallinity of MoO_3 significantly affected the catalytic properties of MoO_3 [38]. Combining the concepts of ball-milling and ammonolysis might lead to more active model catalysts. Variation of crystallinity of MoO_3 might also enable conclusions about structural effects on thermal stability of MoO_3-type oxide nitrides. A detailed knowledge of structure is indispensable to elucidate correlations between lattice oxygen mobility, electrical properties, crystallite size, and catalytic activity. Therefore, a detailed characterization of bulk structural properties of ball-milled MoO_3 and its corresponding oxide nitrides was performed by XRD, FTIR and DR-UV-Vis. Additionally, the electrical properties were investigated by impedance spectroscopy in different oxygen/nitrogen atmospheres.

3.2 Experimental

3.2.1 Sample preparation

Molybdenum oxide (MoO_3, Chempur, 99+ %) was dried at 383 K. Afterwards, MoO_3 was milled in a planetary mill with 150 rpm over different periods of time. An agate container with 5 agate balls was used for the milling process. For each approach an initial weight of 3 g MoO_3 was placed in the planetary mill. After 20, 60, 120, 180 and 240 minutes the ball-milling process was stopped, leading to the notification *MO*, *MO60*, …, *MO240*.

MoO_3-type oxide nitrides were produced by ammonolysis of 400 mg of ball-milled MoO_3 using a tube furnace with silica tube and direct gas supply [85]. Ammonolysis was carried out at 498 K for 5 hours. The respective gas flow of 10 l/h NH_3 (N38, Air Liquide, 99.98%) was adjusted by mass flow controllers (Bronkhorst). Ammonolysis products were denoted *MON*, *MON60*,…, *MON240*. Elemental analysis provided information about the nitrogen content in the prepared samples. Ammonolysis of MO resulted in an incorporation of 0.4 wt% nitrogen while ammonolysis of all ball-milled MoO_3 samples led to oxide nitrides with 1.0 wt% nitrogen content.

3.2.2 Sample characterization

X-Ray diffraction (XRD)

Ex situ XRD measurements were recorded on a STADI P diffractometer in transmission mode using Cu $K_{\alpha 1}$ radiation and a position-sensitive-detector (PSD). A Ge-crystal was used as monochromator. Measurements were performed in a range of 10 – 80° 2θ in steps of 0.1° with a sampling time of 90 s/step. Rietveld refinements were carried out by using the FullPROF program [86,87]. Single reflection refinements for size-strain analysis were conducted by using the software package WinXAS v3.2 [88]. Fourier profile analysis were carried out using the program BREADTH to reveal distribution functions of column lengths [89,90].

Diffuse Reflectance UV-Vis spectroscopy (DR-UV-Vis)

DR-UV-Vis measurements were conducted on a two-beam spectrometer (V670, JASCO) using an integration sphere coated with barium sulfate. Powder samples were measured in the spectral region of 220–2000 nm. Boron nitride (Alfa Aesar, 99.5%) was used for sample dilution and as reflectance standard for baseline correction. The DR-UV-Vis spectra were transferred into the Kubelka-Munk function, $F(R_\infty)$ according to **eq. (2-9)**.

Impedance spectroscopy

Impedance spectra of mixed molybdenum oxides and oxide nitrides were obtained by measuring the magnitude $|Z|$ and the phase ϕ of an alternating current as a response of an applied alternating potential (impedance analyzer N4L: IAI+PSM1735). The real part Z' and the imaginary part Z'' of the impedance were calculated from these results. The impedance was measured as a function of frequency (1 Hz - 10 MHz) and temperature. Oxides and oxide nitride samples were pressed to pellets with a diameter of 5 mm (initial weight 60 mg, 750 MPa pressure) and placed between two Au disc electrodes for impedance measurements. Measurements were carried out in a temperature range up to 700 K with flowing gas mixtures. Gas mixtures of oxygen and nitrogen were adjusted by mass flow controllers (Bronkhorst) with a total flow of 85 ml/min.

Fourier-transformed infrared spectroscopy (FTIR)

A Magna System 750 (Nicolet) was used to measure infrared spectra of the samples in a wavenumber range of 50 – 4000 cm^{-1}. Samples were diluted with CsI (1:300) and pressed into pellets of 13 mm in diameter.

Elemental Analysis

Elemental contents of C, H and N were determined by using an analyzer (FlashEA 1112 NC, ThermoFinnigan/ThermoElectron) with CHNS-O configuration. Measurements were carried out after ammonolysis of ball-milled MoO_3.

3.3 X-ray diffraction (XRD)

3.3.1 Rietveld refinements

XRD powder patterns of MoO_3 after different times of ball-milling and its corresponding oxide nitrides are shown in **Figure 3-1**. MoO_3 crystal structure was preserved during ball-milling and adjacent ammonolysis. A line broadening of the X-ray diffraction peaks after ball-milling and ammonolysis was observed. Line broadening can be due to a decrease in particle size or increase in lattice strain. Size-strain analysis will be described in **chap. 3.3.3**.

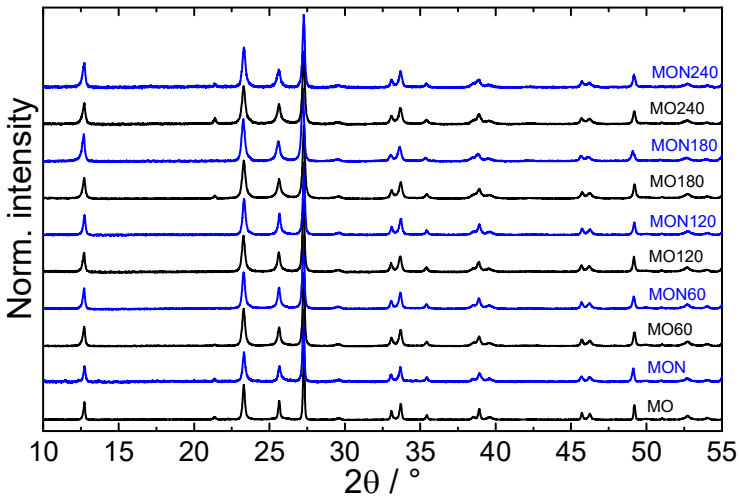

Figure 3-1: XRD powder patterns of ball-milled MoO_3 (black) and its corresponding oxide nitrides (blue). Milling time was increased from bottom to top.

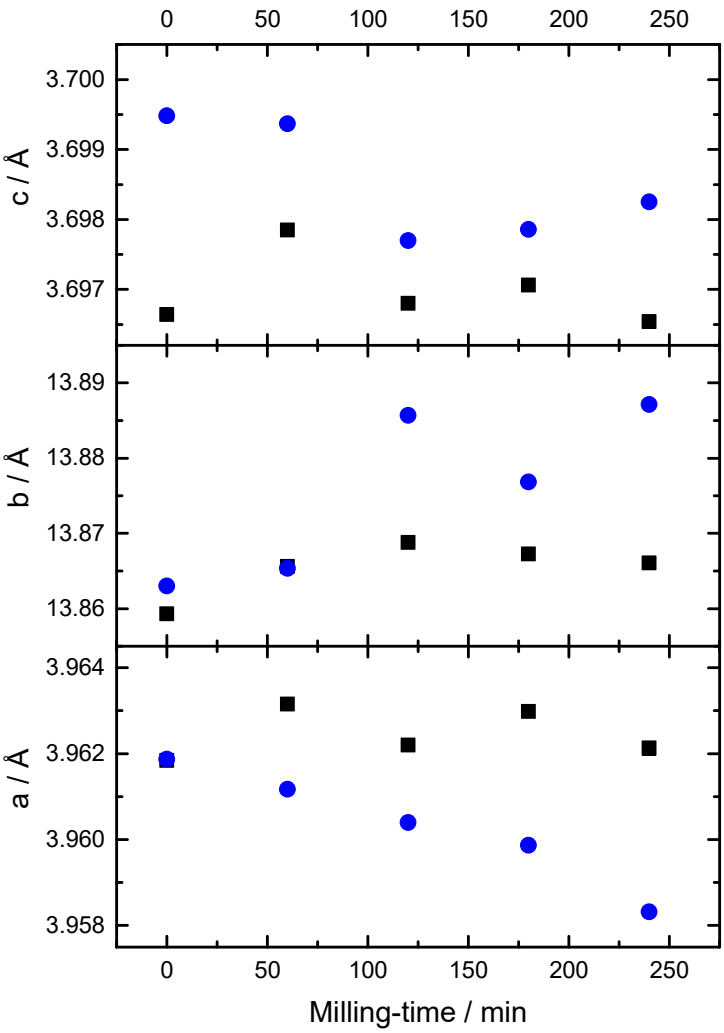

Figure 3-2: *Lattice parameters of MoO_3 (black squares) and its oxide nitrides (blue circles) as a function of milling time.*

A Rietveld refinement of the MoO_3 crystal structure to all XRD patterns was carried out [91]. A pseudo-Voigt function convoluted with an axial divergence asymmetry function was used for Rietveld refinement. The asymmetry function was used to account peak asymmetry at low diffraction angels [92]. Results of Rietveld refinements are listed in **Table A 1-1** and **Table A 1-2**. The evolution of lattice parameters of all samples as a function of milling-time is shown in **Figure 3-2**. Lattice parameters were not significant influenced by ball-milling. Only a slight increase of the *b* parameter was observed after short time of milling. However, ammonolysis of ball-milled MoO_3 affected the lattice parameters. While the *a* parameter decreased during ammonolysis, the *b* and *c*

parameters were slightly increased after ammonolysis. The decrease of the *a* parameter was more intensive for longer milled MoO_3-type oxide nitrides. The increase of the *b* parameter after ammonolysis was more distinct when MoO_3 was ball-milled at least 120 minutes. Otherwise, the increase of the *c* parameter showed the opposite evolution. Similar increasing and decreasing trends of lattice parameter after incorporation of nitrogen ions were observed when hydrogen molybdenum bronzes H_xMoO_3 were formed [93]. Additionally, a slight increase in cell volume was also found for other transition metal oxides nitrides [94,95].

3.3.2 Derivation of approaches for size-strain analysis

Single-line analysis (SLA)

The profile of diffraction peaks contains information of crystallite size and lattice strain as explained in **chap. 2.1**. Analysis of peak shape can be carried out by several different methods. The application of whole powder fitting methods is often not functional to separate size and strain broadening. For *in situ* measurements high quality data might not be achievable [96]. Instead, the analysis of integral breadths represents a simple way for determining size and strain. In addition, MoO_3 is known for anisotropic lattice strain and its structure sensitivity for propene oxidation [38,97]. Hence, refinements of profile functions to single diffraction peaks might result in differentiation of various *hkl*.

A diffraction line profile *h* is conceived as a convolution of an instrumental profile *g* with the sample profile *f*. All profiles can be described by Voigt functions which are convolutions of Gaussian and Cauchy (also called Lorentzian) functions. The Voigt function *V(x)* is given by

$$V(x) = I_0 \frac{\beta}{\beta_C \beta_G} \int C(z) G(x - z) dz \tag{3-1}$$

with Cauchy and Gaussian components *C* and *G*. An alternate profile function for refinement procedures with suitable results is the pseudo-Voigt function. The pseudo-Voigt function *pV(x)* is defined as linear combination of a Cauchy and Gaussian function

$$pV(x) = I_0[\eta C(x) + (1-\eta)G(x)] \tag{3-2}$$

with mixing parameter η [98]. The pseudo-Voigt function represents a simple approximation for the Voigt profile function. The time of refinement decreases strongly by waiving multiple numerical convolutions [99]. After elimination of instrumental broadening the Cauchy and Gaussian components of the integral breadth β_C and β_G can be extracted from the mixing parameter η by using empirical evaluation of $\beta_{C/G}/\beta$ [100]:

$$\frac{\beta_C}{\beta} = 0.017475 + 1.500484 \cdot \eta - 0.534156 \cdot \eta^2 \tag{3-3}$$

$$\frac{\beta_G}{\beta} = 0.184446 + 0.812692\sqrt{1 - 0.998497 \cdot \eta} - 0.659603 \cdot \eta + 0.445542 \cdot \eta^2 \tag{3-4}$$

It is assumes that microstrain is represented by Gaussian component. The finite crystallite size influences the Cauchy component. Hence, calculation of crystallite size D and lattice strain ε of a single diffraction line can be carried out by following equations:

$$D = \frac{\lambda}{\beta_C \cos\theta} \tag{3-5}$$

$$\epsilon = \frac{\beta_G}{4\tan\theta} \tag{3-6}$$

Column length/crystallite size distribution

The structure of a solid is also characterized by its crystallite size distribution which can be determined by Fourier analysis of diffraction patterns. The peak broadening is described by so-called column-length distribution $p_V(L)$. Therefore, it is assumed that the crystallites are composed of thin columns parallel to the scattering vector. A given diffraction peak is the sum of the individual intensities diffracted by each column. Number of finding a distinct column-length L is the distribution function $p_V(L)$ [101]. In principle, the Fourier coefficients can be expressed by

$$A(L) = exp(-2L\beta_L - \pi L\beta_G^2). \quad (3\text{-}7)$$

These Fourier coefficients are the product of size and distortion coefficients $A^S(L)$, $A^D(L)$. At least two order of a diffraction peak of the considered (*hkl*) plane must be available to obtain $A^S(L)$ and $A^D(L)$. The Cauchy and Gaussian components of integral breadths were calculated by approximations given by eq. (3-3) and (3-4) in the case of refinement of a pseudo-Voigt function. The volume-weighted average column length $\langle L \rangle_V$ is twice the area under $A^S(L)$ curve. Additionally, the area-weighted average column length $\langle L \rangle_A$ is given by the root of a linear regression of the initial slope at $L \rightarrow 0$. Both can be converted into average crystallite sizes. The second derivation of the size coefficients results in the volume-weighted column-length distribution function [89]:

$$p_V(L) = \frac{d^2 A^S(L)}{dL^2} = A^S(L)[(2\pi L\beta_{SG}^2 + 2\beta_{SL}^2)^2 - 2\pi\beta_{SG}^2]. \quad (3\text{-}8)$$

3.3.3 Size-strain analysis of ball-milled MoO_3 and oxide nitrides

Crystallite sizes of various diffraction peaks with various *hkl* indices were calculated using the SLA method described in **chap. 3.3.2**. Crystallite sizes of molybdenum oxides and its oxide nitrides are shown in **Figure 3-3** as a function of milling time. Crystallite sizes of non-milled MoO_3 differed from about 50 nm obtained from (020) diffraction peak to about 160 nm of (200) diffraction peak. Ball-milling led to a significant decrease of all crystallite sizes. The most intensive influence after 60 min was observed for the (200) diffraction peak which correlated to the extension of the crystallite along a-axis. According to the literature the decrease in crystallite sizes was reduced for longer milling-time [81]. Additionally, after 180 min of ball-milling the crystallite sizes remained almost constant in a range from about 20 nm to about 50 nm. The calculation of crystallite sizes of the same diffraction peaks after ammonolysis resulted in a similar distribution of crystallite sizes. Compared to the oxides, the evolution of crystallite sizes as a function of milling time exhibited a similar trend.

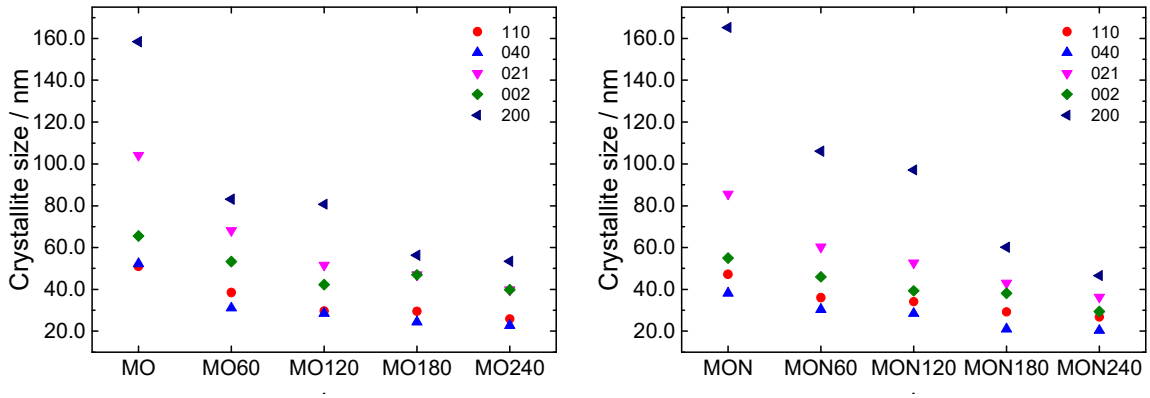

Figure 3-3: *Evolution of crystallite sizes of different reflections as a function of milling time estimated from single-line analysis. Left: Ball-milled MoO_3, right: MoO_3-type oxide nitrides.*

Single-line analysis resulted in various ranges of crystallite sizes. Hence, a more detailed analysis of (0*k*0) reflections was carried out using Fourier analysis of respective profiles. After subtraction of instrumental broadening the Fourier coefficients were calculated. The normalized Fourier size coefficients $A^S(L)$ are shown in **Figure 3-4** as a function of column length *L*. Increasing milling-time of MoO_3 led to a decrease in area under $A^S(L)$ curve. Additionally, an increase of the slope of linear range at low column lengths was determined. An area-weighted average crystallite size of 35 nm of non-milled MoO_3 was determined while a volume-weighted crystallite size of 69 nm was calculated. The difference in both crystallite sizes is a known effect of the calculation method [101]. According to **eq. (3-8)** the distribution functions of Fourier size coefficients were calculated. Ball-milling of MoO_3 resulted in a shift of the maximum of the distribution function to lower column length. In addition, the number of higher column lengths decreased with milling-time. The evolution of calculated crystallite sizes with various milling-times from SLA method was corroborated. The range of values of found column lengths decreased after ball-milling of MoO_3. Hence, milling process led to a homogenization of crystallite size distribution. Calculating Fourier size coefficients and distribution functions of MoO_3-type oxide nitrides resulted in similar trends and can be found in the appendix (**Figure A 1-1**). The results of size-strain analysis are summarized in **Table 3-1**.

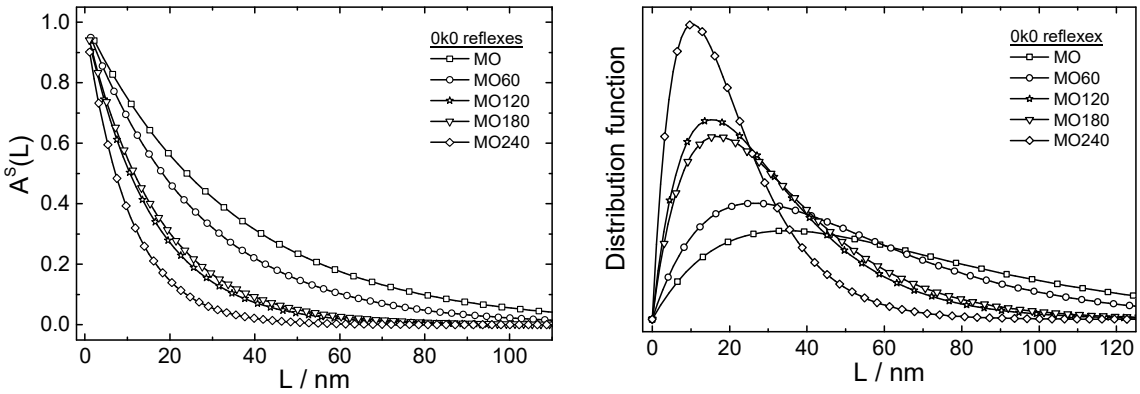

Figure 3-4: *Left: Fourier size coefficients as a function of column length calculated from 0k0 diffraction peaks. Right: Distribution function of averaged distances in real space of MoO_3 before and after ball-milling calculated from 0k0 diffraction peaks.*

Table 3-1: *Results of crystallite size analysis of MoO_3 samples and its corresponding oxide nitrides. .*

	D_{SLA} (040) /nm	$\langle D \rangle_A$ /nm	$\langle D \rangle_V$ /nm
MO	52.2	34.6	69.2
MO60	35.4	26.4	52.8
MO120	28.5	15.3	30.7
MO180	21.1	16.8	33.5
MO240	22.7	10.4	20.8
MON	38.2	24.2	49.7
MON60	30.4	20.4	40.9
MON120	28.5	18.8	37.4
MON180	21.1	12.5	25.1
MON240	20.3	13.8	27.5

In addition to changes of crystallite size variation of lattice strain can also lead to diffraction line broadening. Lattice strain of diffraction peaks with various *hkl* indices was calculated using single line analysis (**Figure 3-5**). A significant influence of ball-milling on lattice strain was not observed. Hence, ball-milling of MoO_3 only led to changes in crystallite sizes according to results of SLA. Incorporation of nitrogen in MoO_3 resulted in a significant increase in lattice strain. The influence on lattice strain was independent of

(*hkl*) plane. Each investigated reflection correlated to lattice strain along one axis. In agreement with evolution of lattice parameters each direction of the orthorhombic crystal system was affected by ammonolysis.

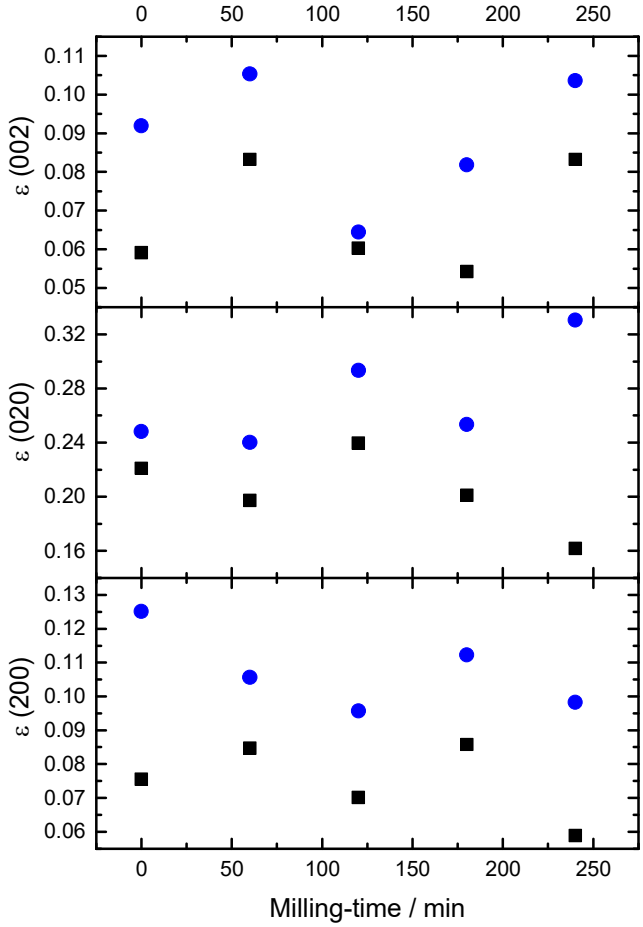

Figure 3-5: *Lattice strain of ball-milled MoO_3 and its oxide nitrides as a function of milling-time calculated by single-line analysis of different reflections.*

3.4 Fourier-transform infrared spectroscopy (FTIR)

FTIR spectra of ball-milled MoO_3 and its corresponding oxide nitrides are shown in **Figure 3-6**. The characteristic metal-oxygen vibration modes were detected below 1000 cm^{-1}. After ball-milling and ammonolysis no additional metal-oxygen vibration modes were observed. Hence, the preservation of crystal structure during preparation shown by XRD was confirmed. The peak positions were determined by analyzing second and fourth derivatives of each spectrum and are summarized in **Table A 1-3**.

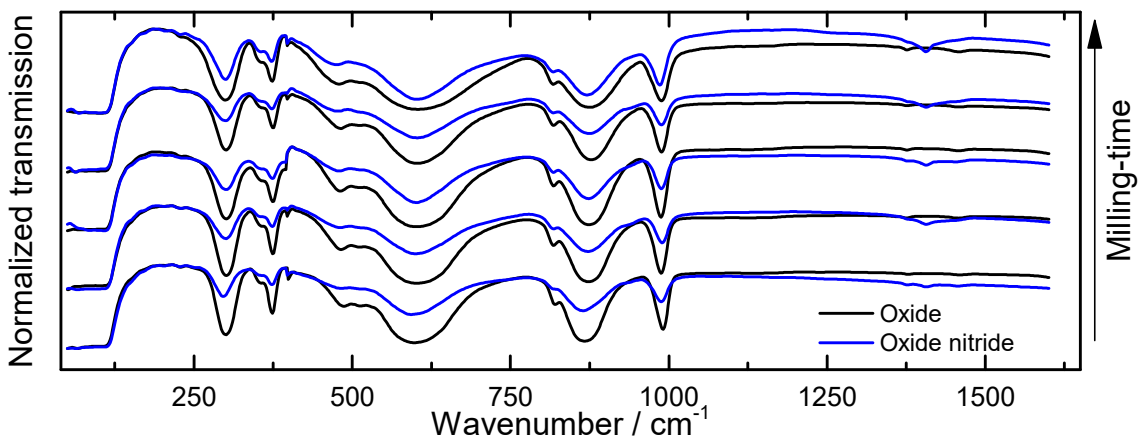

Figure 3-6: *FTIR-spectra of ball-milled MoO_3 (black) and its corresponding oxide nitrides (blue). Milling-time was increased from bottom to top.*

In the MIR region (400 – 4000 cm^{-1}) four strong absorption bands and one weaker absorption bands were distinguished and attributed to various stretching vibration modes [102]. The absorption band at 989 cm^{-1} was due to stretching vibrations of terminal molybdenum-oxygen bonds (νMo=O). The absorption bands at 818 cm^{-1} and at about 875 cm^{-1} were induced by stretching vibrations of oxygen atoms in a Mo-O-Mo bridge (νOMo_2). The broad absorption band centered at about 600 cm^{-1} and the less intensive absorption band at about 482 cm^{-1} were assigned to the stretching vibration of oxygen atoms linked to three molybdenum atoms (νOMo_3). In addition, the band positions assigned to different deformation modes were determined in die FIR region (200 – 400 cm^{-1}). In compliance with stretching vibration modes the deformation modes were class-divided into deformations of terminal molybdenum-oxygen bonds (δMo=O), oxygen atoms linked to two or three molybdenum atoms (δOMo_2 or δOMo_3) [103]. Ball-milling of MoO_3 affected a shift of peak positions of νOMo_3 and νOMo_2 modes to higher wavenumbers.

The incorporation of nitrogen ions led to a shift of peak positions of δOMo_3 and δO=Mo to lower wavelengths. Band shift to lower wavenumbers corresponds to a weakening of bond strength. Hence, decreasing metal-oxygen bond strength may lead to increased oxygen mobility [104]. Weakening of bond strength might also be accompanied by increasing metal-oxygen distances which was in agreement with results of Rietveld

refinements (**chap. 3.3.1**). **Figure 3-7** shows a schematic presentation of MoO_6 octahedron of α-MoO_3 including the relation between crystallographic directions and different types of molybdenum-oxygen bonds. An increase in molybdenum-oxygen distance might lead to an elongation of unit cell in the respective direction. Hence, a significant increase of *b* parameter after ammonolysis was determined by XRD Rietveld refinements. The *b* parameter was also related to metal-oxygen bonds with terminal and triple linked oxygen atoms. In addition, a slight increase of the *c* parameter (XRD) was observed after ammonolysis. Only metal-oxygen bonds with triple linked oxygen atoms (OMo_3) were found along *c*-axis. These oxygen atoms belong to the edge-sharing site of octahedron and are next to interlayer space of α-MoO_3. Furthermore, the terminal oxygen atoms along *b*-axis are next to the interlayer space. In summary, the molybdenum-oxygen bonds adjacent to interlayer space were mainly influenced by incorporation of nitrogen. NH_3 might diffuse into layers of α-MoO_3 and decomposed into reactive species during ammonolysis [49]. The terminal oxygen was the most accessible oxygen species for being substituted by reactive species of NH_3.

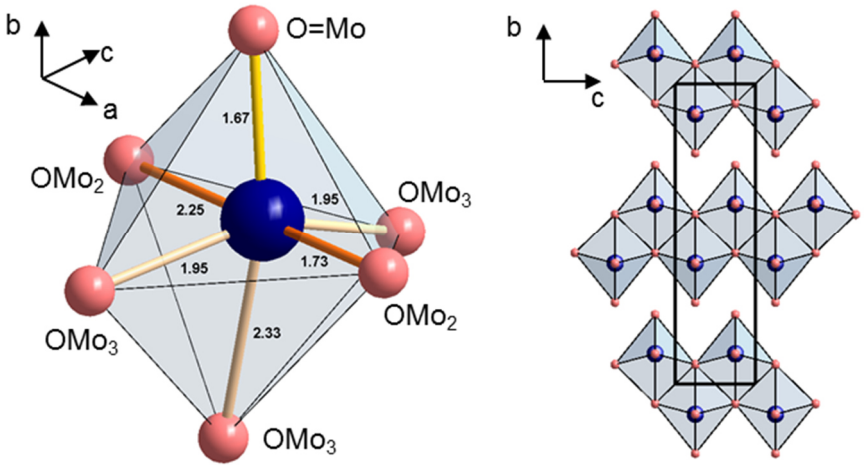

Figure 3-7: *Left: Schematic presentation of MoO_6 octahedron of α-MoO_3 including atom distances. The different type of molybdenum-oxygen bonds are marked according to classification in FTIR spectra (Terminal O=Mo, oxygen atoms linked to two or three molybdenum atoms) [102]. Right: View on the and bc plane of α-MoO_3.*

In **Figure 3-8** the FTIR spectra of ball-milled MoO_3 and its corresponding oxide nitrides are shown in a wavenumber range from 1250 – 4000 cm^{-1}. The spectra of all samples showed absorption bands at about 1378, 1460 and 1625 cm^{-1} which was attributed to OH vibration modes [105]. According to Mestl the band at 1625 cm^{-1} was due to deformation of H_2O molecules in a network of H bridges while the band at 1460 cm^{-1} was assigned to OHO bending vibrations of molybdenum hydrates [83]. The characteristic OH stretching regime was reproduced at higher wavenumbers. A combination mode of absorption bands at 2840, 2871, 2923 and 2956 cm^{-1} was determined [74]. Additionally, a broad absorption band between 3200 and 3650 cm^{-1} was observed which was assigned to OH groups and adsorbed water. Molybdenum oxide is well-known for formation of various hydrates $MoO_3 \cdot xH_2O$ (x = 1/3, 1/2, 1 and 2) [102]. Otherwise, the insertion of hydrogen is also often combined with formation of hydrogen molybdenum bronzes H_xMoO_3. In the literature formation of H_xMoO_3 with little amounts of hydrogen led to significant changes in FTIR spectra. New absorption bands were observed of H_xMoO_3 while intensity of characteristic metal-oxygen absorption bands of α-MoO_3 decreased [106,107]. Hence, the occurrence of OH vibration modes in FTIR spectra of ball-milled MoO_3 might be due to molybdenum hydrates. **Figure 3-8** shows the intensity of absorption bands at 1378, 1460 and 2923 cm^{-1} normalized to the intensity of terminal stretching molybdenum-oxygen vibration mode (νMo=O). This normalization was chosen due to changing concentrations of absorbing centers. The normalized intensity of absorption bands was increased after ball-milling of MoO_3. The decreased crystallite size of MoO_3 after ball-milling led to an enhanced accessibility for hydrogen atoms. Additionally, the mechanical activation of MoO_3 caused a more stable incorporation shown by a slight shift of absorption bands to higher wavenumbers.

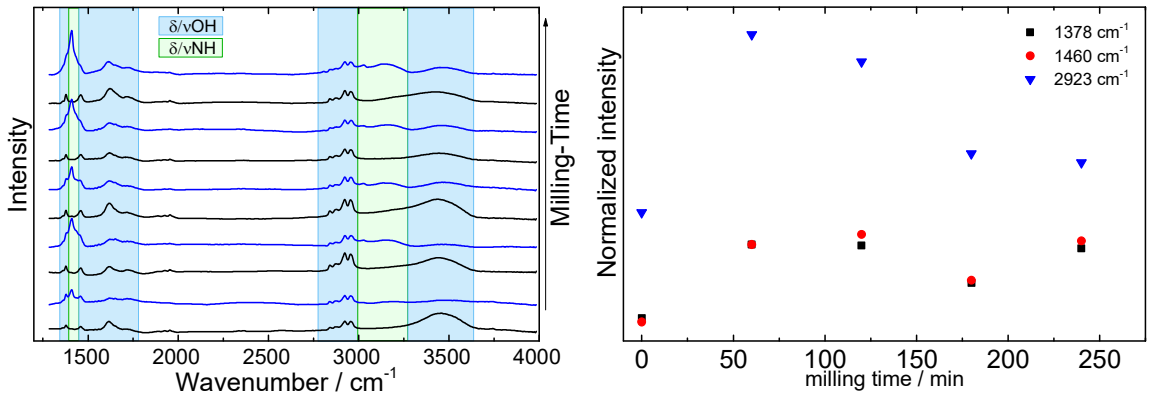

Figure 3-8: *Left: FTIR spectra ball-milled MoO_3 (black) and its corresponding oxide nitrides (blue). Milling-time was increased from bottom to top. The regions of deformation and stretching vibration modes of O-H (blue rectangle) and N-H (green rectangle) are marked. Right: Normalized intensity of different O-H vibration modes. Band intensities were normalized to intensity of band at 989 cm^{-1}.*

After ammonolysis of ball-milled MoO_3 the same OH vibration modes were determined. However, the maximum of the broad absorption band was shifted to higher wavenumbers by at about 10-20 wavenumbers. This shift was increased after longer milling of MoO_3. In addition, two new absorption bands at about 1407 and 3160 cm^{-1} were formed by ammonolysis [49]. Both absorption bands were attributed to vibration modes of NH groups. Compared to non-milled MoO_3-type oxide nitrides the bands of the spectra of ball-milled MoO_3-type oxide nitride were more intensive. Subsequently, the higher intensity confirmed the results of elemental analysis. The reactivity for incorporation of nitrogen was increased by ball-milling. Significant absorption bands of NH groups indicated that nitrogen ions was mainly incorporated as $(NH)^{2-}$. If NH_3 reacted during ammonolysis with oxygen ions from the solid, nitrogen ions were incorporated in the anion lattice. The effective negative charge in the Kröger-Vink notation was compensated by formation of water and oxygen vacancies (**eq. (3-9)**) [108]. According to **eq. (3-10)** the binding energy, $\Delta E^{b}_{NH_O^X}$, was found to be exothermic for several investigated oxides. Hence, the coexistence of N_O' and $OH_O^{\cdot}$ led to strengthened formation of NH_O^X [109]. The existence of $OH_O^{\cdot}$ was shown by different OH vibration

modes. However, the formation of NH_O^X could also be formulated without formation of oxygen vacancies (**eq. (3-11)**).

$$2NH_3(g) + 3O_O^X = 2N_O' + V_O^{\cdot\cdot} + 3H_2O \tag{3-9}$$

$$N_O' + OH_O^{\cdot} = NH_O^X + O_O^X \tag{3-10}$$

$$2NH_3(g) + 2O_O^X = NH_O^X + 2H_2O \tag{3-11}$$

3.5 Diffuse Reflectance UV-VIS spectroscopy (DR-UV-Vis)

The DR-UV-Vis spectra of all MoO_3 samples and its corresponding oxide nitrides are shown in **Figure 3-10**. According to the literature the energy of the optical band gap was determined by plotting $(F(R_\infty) \cdot E)^2$ as a function of energy. Afterwards, the root of a linear regression in linear range of absorption edge revealed the energy of optical band gap [110]. Energies of the optical bandgaps of all samples are shown in **Figure 3-9**. The energy of optical band gap slightly increased with milling time of MoO_3 from 3.3 eV to 3.5 eV due to decreased crystallite size. Incorporation of nitrogen ions in the anion lattice of MoO_3 led to a significant decrease in band gap energy which was independent of milling time. MoO_3 is a wide-gap semiconductor and the width of the forbidden band is related to the position of *2p* levels of oxygen and *4d* levels of molybdenum. After ammonolysis nitrogen ions were incorporated and conferred additional levels to the valence band. The lower electronegativity of nitrogen compared to oxygen effected a difference in energy level of *2p* orbitals of oxygen and nitrogen ($E_{2p}(O)$ = -14.8 eV, $E_{2p}(N)$ = -13.4 eV at the top of the valence band) [45]. As a result, the width of the band gap was lowered by incorporation of nitrogen ions.

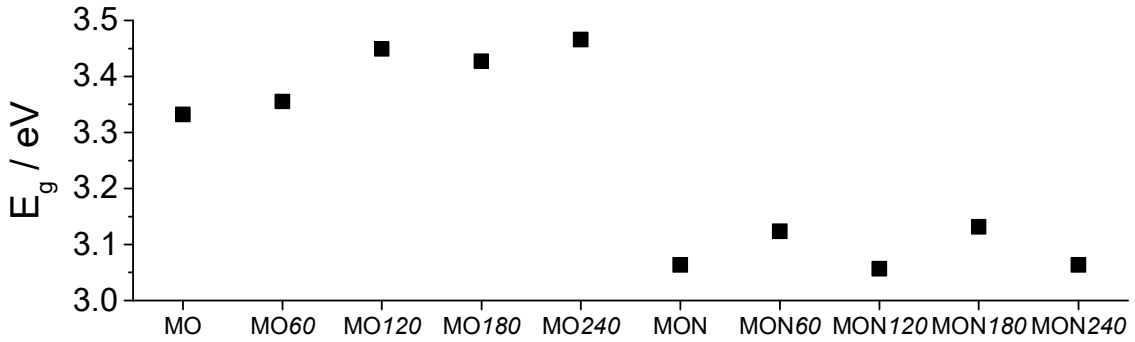

Figure 3-9: *Energy of optical band gap of all samples.*

In the low energy range below 3 eV non-milled MoO_3 (*MO*) showed a low absorption with a weak maximum at 2.08 eV. Absorption of *MO* increased with decreasing energy. After milling the absorption below 3 eV increased while the evolution of spectra was similar to that of *MO*. The absorption band at 2.08 eV can be attributed to an inter-valence-charge-transfer (IVCT) [23]. Dieterle et al. explained the existence of IVCT by formation of defects caused by oxygen vacancies. The increasing absorption around 1.5 eV was discussed as IVCT or polaron conductance along Mo^{5+}-O-Mo^{6+} chains. Apparently, it might be assumed that the formation of Mo^{5+} centers was due to breaking most stressed molybdenum-oxygen bonds by mechanical activation [82,111]. The electronic structure of MoO_3 is dependent on the oxidation state of molybdenum centers. Formation of Mo^{5+} centers resulted in a partially occupied 4d level within the band gap of MoO_3 [112]. A schematic presentation of energy levels for optical transitions in MoO_3 is given in **Figure 3-12**. In addition, the formation of MoO_{3-x} defect structures is often combined with formation of shear structures [113]. The absorption in this energy range increased significantly after ammonolysis. In compliance with previous work no distinct absorption maxima could be determined. A similar effect has been described for intensive colored zirconium oxide nitrides [42]. Additionally, the significant increase indicated more intensive IVCT and polaron transfers due to formation of defect structures.

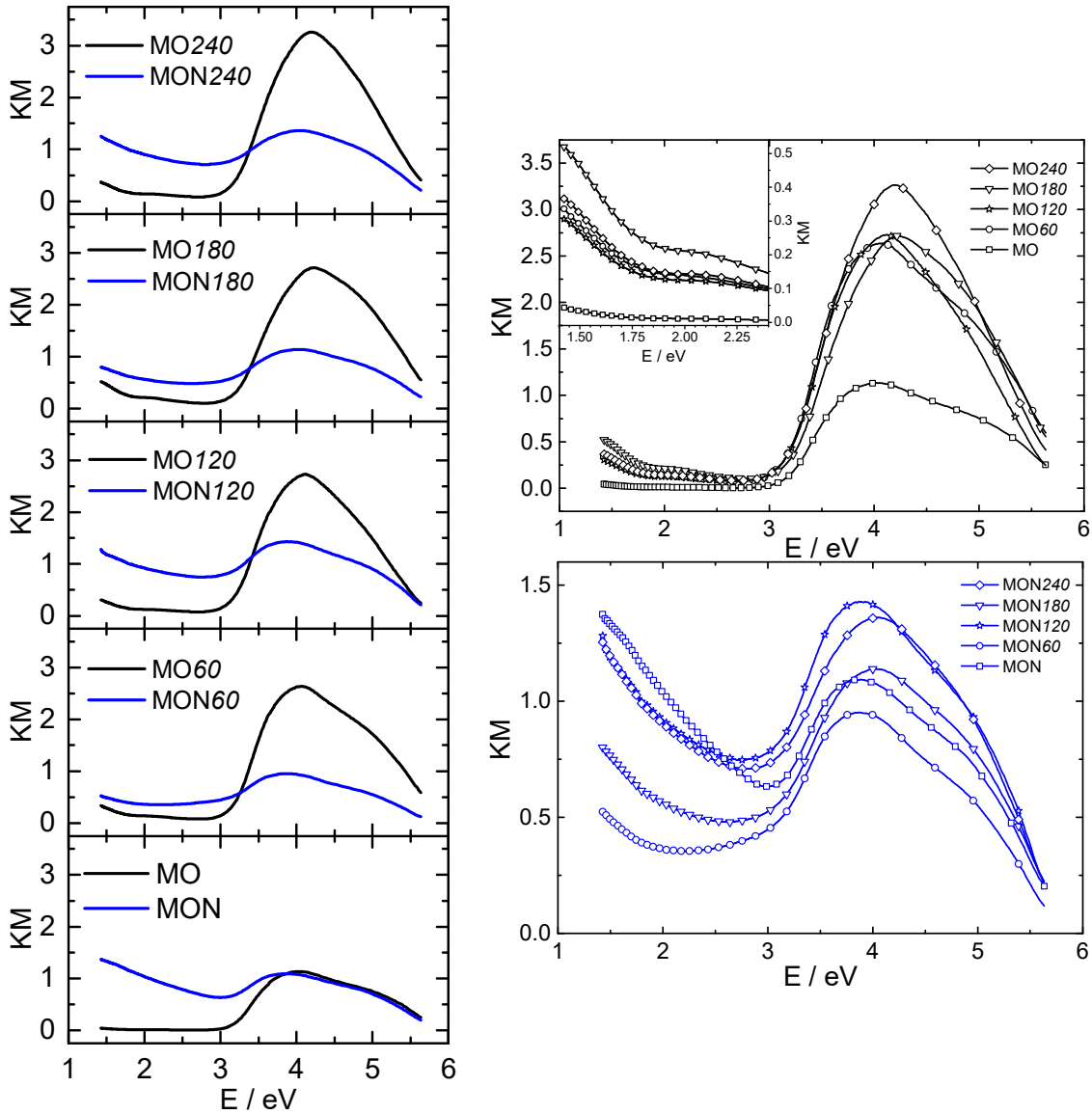

***Figure 3-10**: DR-UV-VIS spectra of ball-milled MoO_3 (black) and its oxide nitrides (blue). Milling time was increased from bottom to top.*

Table 3-2: *Positions of characteristic features (eV) of the DR-UV-Vis spectra of ball-milled MoO_3 and its oxide nitrides in the energy range above absorption edge.*

	Maximum absorption	I	II	III	IV	V
MO	4.03	3.57	3.73	4.16	4.44	4.76
MO60	4.10	3.58	3.79	4.18	4.46	4.75
MO120	4.12	3.58	3.80	4.17	4.45	4.75
MO180	4.20	3.58	3.70	4.19	4.42	4.75
MO240	4.21	3.58	3.79	4.21	4.48	4.76
MON	3.87	3.58	3.78	4.18	4.47	4.77
MON60	3.87	3.58	3.78	4.18	4.46	4.76
MON120	3.89	3.58	3.78	4.18	4.46	4.75
MON180	4.03	3.57	3.76	4.17	4.42	4.75
MON240	4.04	3.58	3.79	4.20	4.45	4.76

All spectra showed a strong absorption above 3 eV which can be attributed to interband (valence band to conduction band) and exciton transitions [114]. The positions of 5 absorption bands in the energy range above 3 eV could be determined by analyzing second and fourth derivatives of each spectrum. The respective band positions are summarized in **Table 3-2**. MoO_3 exhibits absorption bands around at 3.7, 4.3 and 4.5 eV [115]. Additionally, Tinet et. al determined a broad absorption band containing three peaks at 3.6, 4.9 and 5.4 eV [116]. The determined band positions were in good agreement with the reported band positions and were assigned to exciton formation in MoO_3. Excitons are a bound state formed by electron-hole pairs in a semiconductor. Spectra of these exciton transitions are extremely sensitive to crystallinity and morphology [82]. Absorption bands at around 3.7 (II), 4.2 (III) and 4.5 eV (IV) shifted to higher energies after ball-milling (**Figure A 1-2**). Additionally, maximum of absorption at about 4 eV shifted to higher energies. This shift might be attributed to changes in crystallite size. A correlation between energy of maximum absorption and crystallite size calculated from SLA of (020) diffraction peak was established (**Figure 3-11**). Furthermore, protons might also be incorporated by ball-milling at unsaturated molybdenum centers and affect excitons bands. Two bands were determined for $MoO_3 \cdot H_2O$ at 3.64 eV and 4.42 eV which are close

to experimentally determined absorption bands. The absorption band at about 3.5 eV was also assigned to excitons from Mo^{5+} enters which is in agreement with the analysis of the low energy range of spectra [82]. Already short time of ball-milling of MoO_3 resulted in a significantly increased intensity of absorption above 3 eV. Mainly, the intensity of absorption bands at 3.5, 4.2 and 4.8 eV were affected. The increase of intensity might be attributed to formation of defects (e.g. shear defects) or changes in crystallite size.

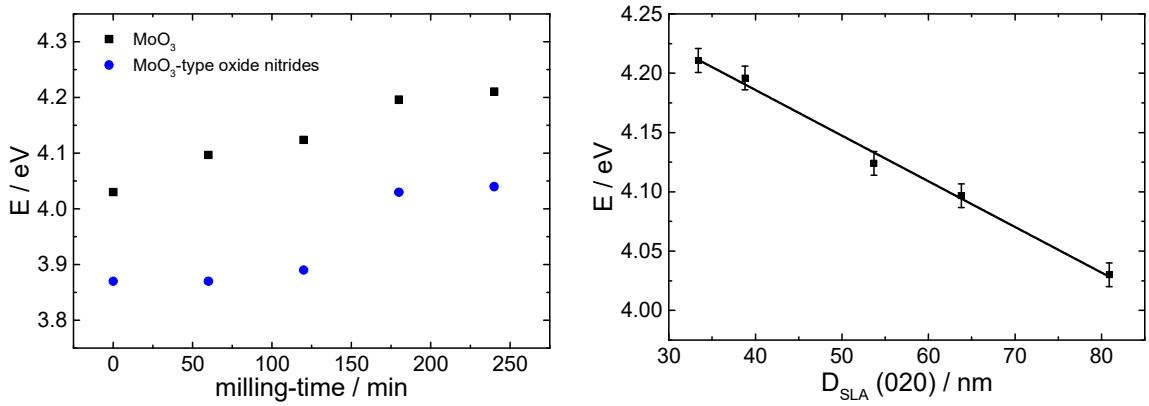

Figure 3-11: *Left: Position of maxima of DR-UV-Vis spectra of ball-milled MoO_3 and its oxide nitrides as a function of milling-time. Right: Dependency of maxima of DR-UV-Vis spectra on crystallite size calculated from (020) diffraction peaks using SLA.*

After ammonolysis the same absorption maxima was determined. The maximum absorption of each spectrum shifted to lower energies while the evolution as a function of milling time was preserved. This shift might be explained in a similar way as the decrease of absorptions edge. Incorporation of nitrogen ions led to formation of additional levels in the valence band. Hence, the energy for exciton transitions decreased. A slight shift of single absorption bands was observed. In addition, ammonolysis led to a decrease in intensity of absorption bands. Size analysis of XRD diffraction patterns revealed an invariant crystallite size after ammonolysis. Hence, the variation of intensity might not be due to changes in crystallite size. Thus, the formation of defects like oxygen vacancies might cause an increase of intensity after ball-milling. In agreement with analysis of FTIR spectra the additional negative charge of nitrogen ions was mainly compensated by incorporation of $(NH)^{2-}$. This type of charge compensation was not accompanied by the formation of oxygen vacancies.

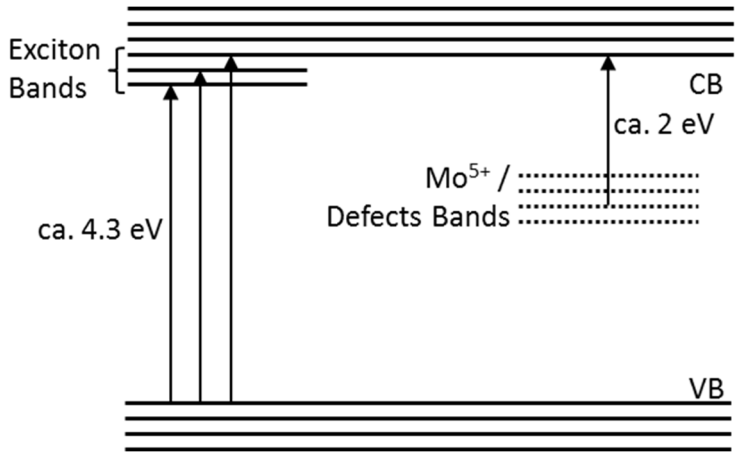

Figure 3-12: *Schematic presentation of energetic levels for optical transitions in MoO_3* [82,115].

3.6 Electrical properties

Electrical properties of ball-milled MoO_3 and its corresponding oxide nitrides were measured by impedance spectroscopy. Impedance spectroscopy represents a suitable method for characterizing electrical properties of nitrogen-substituted MoO_3 [48,117]. Nyquist presentation (negative imaginary part of impedance Z'' vs. real part of impedance Z') resulted in slightly depressed semicircles. The ohmic resistances were determined by refining the impedance of an equivalent circuit to the experimental spectra. A parallel connection of an ohmic resistor R and a constant phase element (*CPE*) was used as equivalent circuit [118]. Using a *CPE* described the deformed semicircles in the experimental data and represents a widely-used empirical model. The d.c. conductivity σ can easily be calculated from the ohmic resistance. The evolution of conductivity of molybdenum oxides is shown in **Figure 3-13**. Above 600 K MoO_3 showed an increasing conductivity indicating the semiconducting behavior of MoO_3. Ball-milling of MoO_3 led to a slight decrease of conductivity. Nevertheless, the evolution of conductivity was similar to that of non-milled MoO_3. From an Arrhenius type presentation of conductivities above 600 K of all samples activation energies for conduction processes were calculated. The activation energies were calculated from the slope of linear fits according to

$$ln\,\sigma = A + \frac{E_A}{k_B T} \tag{3-12}$$

with the Boltzmann constant k_B. Activation energy of 0.83 eV was determined for the non-milled MoO_3 which was in good agreement with previous reports from the literature [48,119]. Ball-milling of MoO_3 slightly influenced the activation energy in the same temperature range. All ball-milled MoO_3 exhibited activation energy of about 1 eV from 600 K – 700 K.

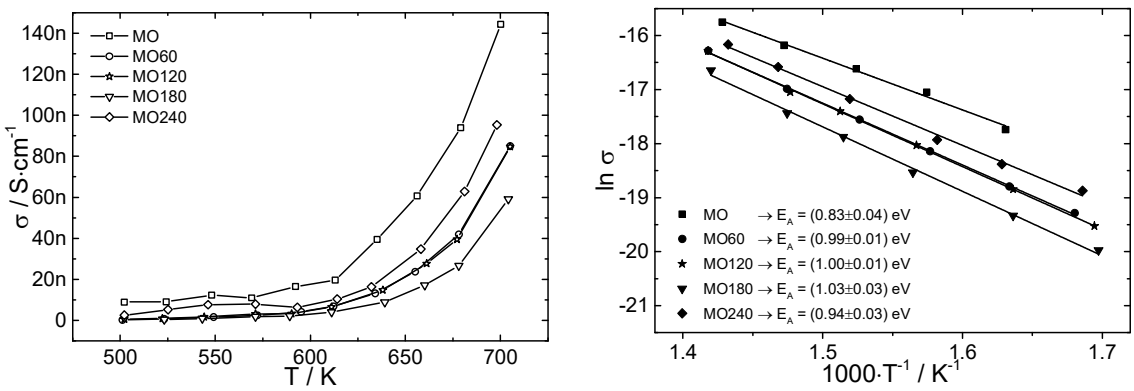

Figure 3-13: *Left: Evolution of conductivity during thermal treatment of ball-milled MoO_3 with different milling-times in air. Right: Arrhenius type presentation of conductivities of ball-milled MoO_3. Activation energies of conduction process are indicated.*

Figure 3-14 shows the evolution of conductivity of MoO_3-type oxide nitrides during thermal treatment in air. Similar to ball-milled MoO_3 the corresponding oxide nitrides exhibited a semiconducting behavior up to about 450 K indicated by increasing conductivity. Conductivity of non-milled MoO_3-type oxide nitride was increased by a factor of 100 compared to ball-milled MoO_3-type oxide nitrides. However, up to 450 K the conductivity of ball-milled MoO_3-type oxide exceeded that of its respective oxides by a factor of 100. Above 450 K MoO_3-type oxide nitrides exhibited decreasing conductivity due to the removal of nitrogen. After removal of nitrogen the conductivity increased again. Thermally treated MoO_3-type oxide nitrides showed similar conductivities as the respective oxides above 625 K. Conductivities increased slightly with increasing temperature. The similar evolution of conductivity as the conductivity of ball-milled MoO_3

indicated a complete removal of nitrogen. The color of the samples changed from dark blue to light gray during thermal treatment in oxidizing atmosphere. The color of MoO_3 can be related to the existence of defects as oxygen vacancies or Mo^{5+} centers. Defect-rich MoO_3 exhibited a blue color while white MoO_3 is defect-poor [120]. Hence, the removal of nitrogen was associated with deletion of defects in the samples.

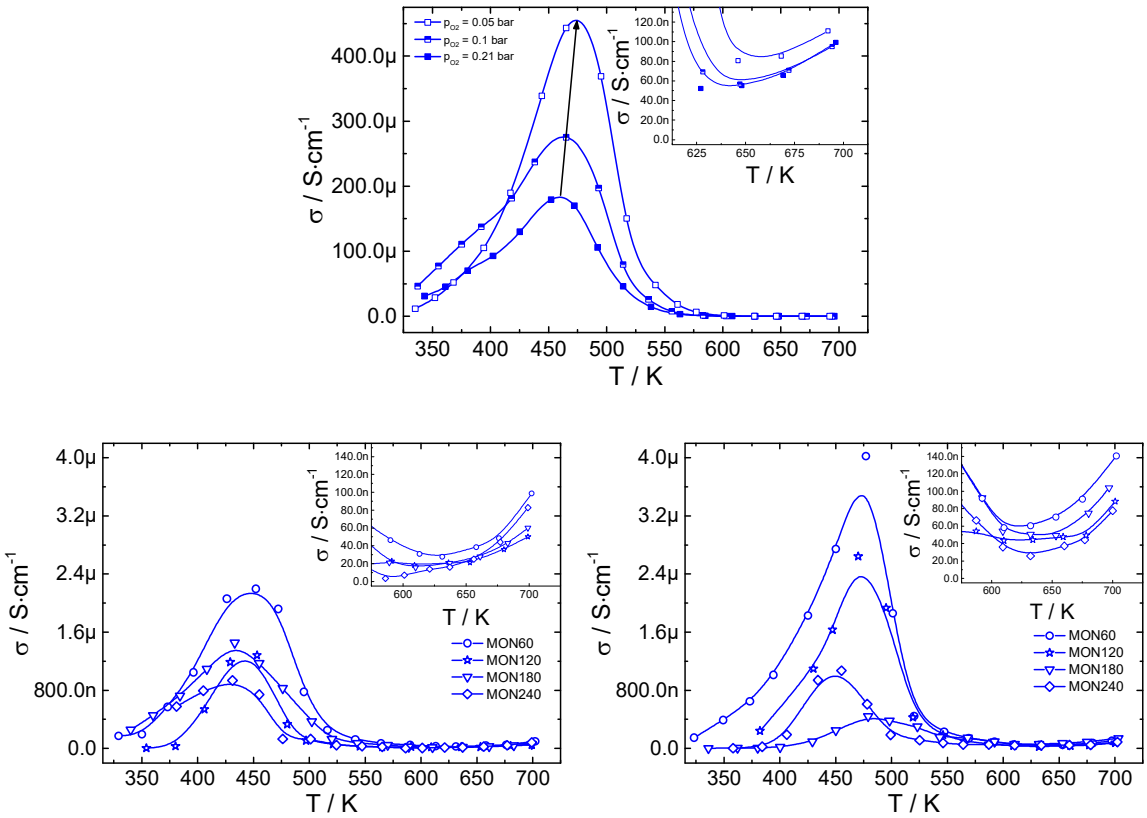

Figure 3-14: *Evolution of conductivity during thermal treatment of MoO_3-type oxide nitrides in different oxygen-nitrogen mixtures (left) and ball-milled MoO_3-type oxide nitrides in air (right).*

Additionally, the influence of oxygen partial pressure on electrical properties was investigated by impedance spectroscopy. The evolution of conductivity of non-milled MoO_3-type oxide nitride during thermal treatment was additionally determined at $p_{O2} = 0.1$ bar and $p_{O2} = 0.05$ bar. The resulting evolution was similar to that in air. However, the maximum of conductivity shifted to higher temperatures and conductivity increased significantly. Hence, the removal of nitrogen started at higher temperatures.

The shift of on-set of nitrogen removal might be due to higher thermal stability with decreasing oxygen partial pressure. Conductivities of ball-milled MoO_3-type oxide nitrides during thermal treatment in 5% oxygen in nitrogen are shown in **Figure 3-14**. Here, conductivities also increased with decreasing oxygen partial pressures. This dependence on oxygen partial pressure revealed that investigated MoO_3-type oxide nitrides showed a n-type semiconducting behavior [121]. MoO_3 is also a well-known n-type semiconductor [122]. Hence, in spite of formation of defects and resulting changes of band structure by ammonolysis of MoO_3 the incorporation of nitrogen did not affected the type of electronic conductivity. The on-set temperature of nitrogen removal shifted to higher temperatures with decreasing oxygen partial pressure. In addition, the end of nitrogen removal was assigned to the minimum between 600 K and 650 K. The determined temperature range of nitrogen removal was correlated to the calculated crystallite sizes from (020) diffraction peaks (**Figure 3-15**). Crystallite sizes were calculated by single-line analysis (**chap. 3.3.3**). Increasing crystallite size led to an increase of on-set and ending temperatures of nitrogen removal. Hence, thermal stability of MoO_3-type oxide nitrides was strongly dependent on crystallite sizes and oxygen partial pressure. The decrease of oxygen partial pressure led to an increase of on-set and ending temperatures of nitrogen removal by about 20-30 K. Furthermore, the temperature range of nitrogen removal might be associated with rate of nitrogen removal. **Figure 3-16** shows the correlation between the extent of this temperature range and crystallite sizes from (020) diffraction peak. The increase of crystallite size calculated from (020) diffraction peak led to a slower removal of nitrogen. The (020) plane was parallel to layers of MoO_6 octahedron. Hence, the calculated crystallite size from (020) diffraction peak gave information of the length of space between the layers (**Figure 1-2**). Increasing the length of interlayer space led to more complicated way of diffusion of nitrogen atoms out of the crystallite.

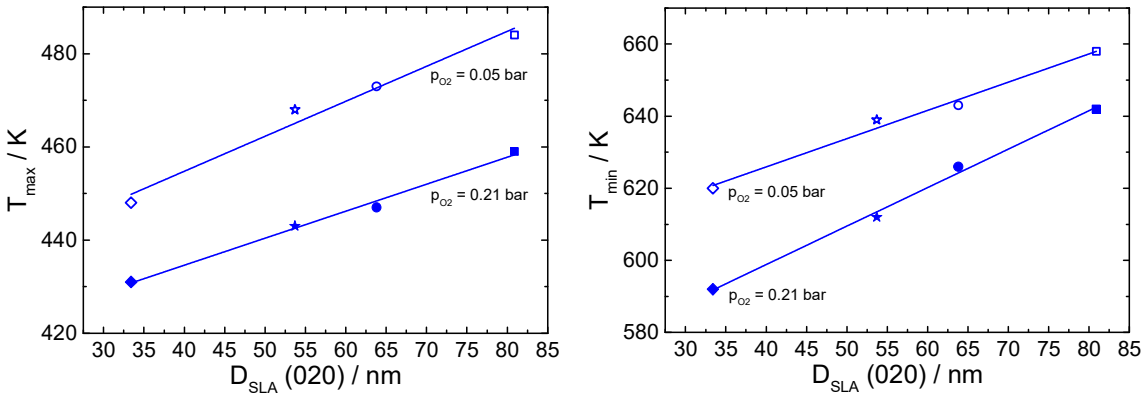

Figure 3-15: *Start temperature (left) and final temperature (right) of nitrogen removal as a function of crystallite size estimated from (020) diffraction peak by single-line analysis.*

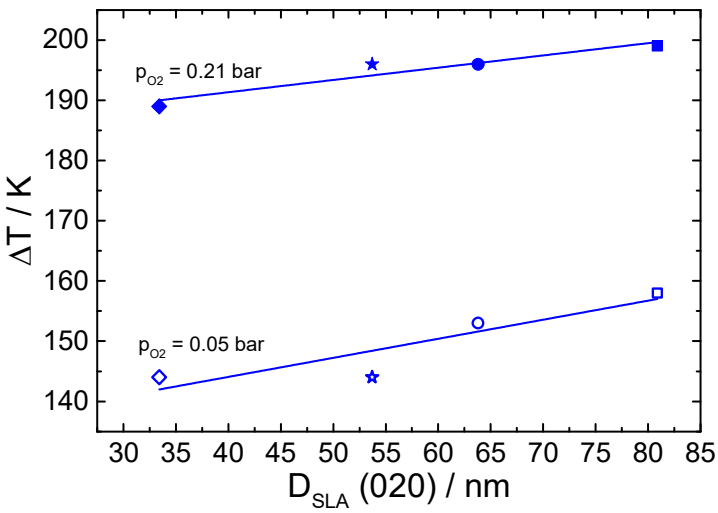

Figure 3-16: *Temperature range for nitrogen removal of MoO_3-type oxide nitrides as a function of crystallite size from (020) diffraction peak in different oxygen partial pressures.*

3.7 Conclusions

Ball-milling of commercially available MoO_3 resulted in a decreasing crystallite size. A homogenization of crystallite sizes was shown by determining the column-length distribution functions from the diffraction patterns of all oxides. Single-line analysis of X-ray diffraction powder patterns revealed an irregular decrease of crystallite size estimated from reflections with different crystallographic direction. Conversely, lattice strain was not significantly influenced by ball-milling. In addition, ball-milling also led to formation of defects as oxygen vacancies or Mo^{5+} centers. Additional energy levels were formed above the valence band MoO_3. Absorption bands in the low energy range of DR-UV-VIS spectra were assigned to IVCT and polaron transitions. Analysis of FTIR spectra of ball-milled MoO_3 revealed the formation of molybdenum oxide hydrates and adsorbed water.

Ammonolysis of ball-milled MoO_3 led to incorporation of nitrogen in the anion lattice of MoO_3 while the crystal structure was preserved. In contrast to ball-milling the ammonolysis slightly increased lattice strain without affecting crystallite size. FTIR spectra were recorded to compare characteristic vibrational modes before and after ammonolysis. Analysis of FTIR band positions revealed that preferably metal-oxygen bonds next to interlayer space of MoO_3-structure were weakened. Apparently, ammonia diffused into the layers of MoO_3 during ammonolysis. Afterwards, oxygen ions were substituted by nitrogen ions. Additionally, FTIR spectra showed the existence of NH_O^X which might be formed by reaction of N_O' and $OH_O^{\cdot}$ (**Figure 3-17**). Ammonolysis of ball-milled MoO_3 was accompanied by a change in color from light-gray to blue. The optical band-gap of ball-milled MoO_3 was significantly decreased after incorporation of nitrogen. The color indicated formation of additional defects. The strongly increase of absorption in low energy range of DR-UV-Vis spectra corroborated this assumption. Absorption in the low energy range was mainly assigned to IVCT and polaron transitions.

Electrical properties of ball-milled MoO_3 and its corresponding oxide nitrides were investigated by impedance spectroscopy. The formation of defects by ammonolysis resulted in a strong increase of conductivity. Furthermore, the thermal stability of MoO_3-

type oxide nitrides in different oxygen/nitrogen atmospheres was analyzed. The removal of nitrogen was related to a significant decrease of conductivity. After removal of nitrogen the samples showed a similar behavior as ball-milled MoO_3. A correlation between thermal stability, crystallite size from (020) diffraction peak and oxygen partial pressure was established. Increasing the size of interlayer space of the MoO_3 structure resulted in more stable corresponding oxide nitrides during thermal treatment. The thermal stability was also increased by decreasing the oxygen partial pressure.

Changing the gas atmosphere can also influence the thermal stability of MoO_3-type oxide nitrides. With respect to application as model catalysts it might be suggested that addition of propene to the gas phase also influence thermal stability. This might be due to reducing properties of propene. Reducing agents can counteract replenishing defects as oxygen vacancies or Mo^{5+} centers. Nevertheless, electrical properties could not be investigated under reaction conditions due to used instrumental setup. Hence, using of further *in situ* analytical methods will be required. DR-UV-Vis spectroscopy seems to be a suitable method for *in situ* determination of defects which can be correlated to stability of MoO_3-type oxide nitrides (**chap. 5.4**).

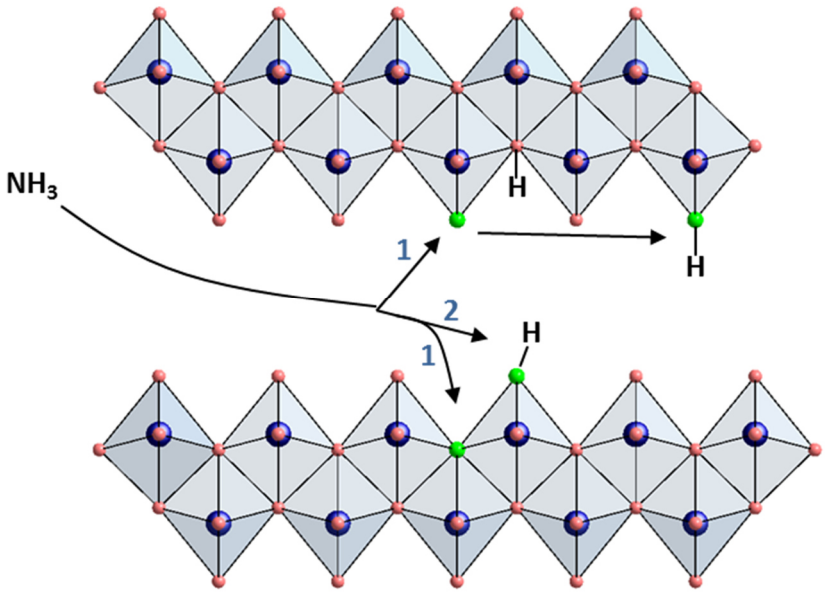

Figure 3-17: *Schematic presentation of ammonolysis processes of ball-milled MoO_3. Nitrogen ions might be incorporated as 1) N_O' (**eq. (3-9)**) or 2) NH_O^X (**eq. (3-11)**). NH_O^X might also be formed by reaction of N_O' and $OH_O^{\cdot}$ (**eq. (3-10)**).*

4 Reducibility of ball-milled molybdenum oxide and oxide nitrides

4.1 Introduction

Selective oxidation of propene proceeds according to a redox mechanism ("Mars-van-Krevelen mechanism") [17]. During the catalyst's cycle the catalyst is partial reduced followed by re-oxidation with gas-phase oxygen [18]. Accordingly, availability of lattice oxygen plays an important role. The metal-oxygen bond strength gives information about the availability of lattice oxygen. The suitability of a catalyst as a function of metal-oxygen bond strength can be described by the Sabatier principle. The idea is that the metal-oxygen bond strength of the best catalysts must be of intermediate strength. If the Me-O bond strength is too weak, the reactant will be over-oxidized. Conversely, strong Me-O bond strength leads to an unreactive catalyst. This principle leads to a volcano-type dependency of suitability of a catalyst on metal-oxygen bond strength [33,123].

The ease of extraction of lattice oxygen from a catalyst can be investigated by studies on the reducibility of the catalyst [21]. Hence, the reducibility of the metal oxide catalyst might play an important role for its activity [124]. Recent studies have shown that incorporation of nitrogen ions in the anion lattice of α-MoO_3 resulted in an improved reducibility [48]. The successful incorporation of nitrogen ions in the anion lattice of α-MoO_3 samples with various crystallinities was described in a previous chapter. In this chapter the availability of lattice oxygen will be investigated by temperature-programmed reduction (TPR) experiments. Additionally, isothermal reduction experiments were carried out to elucidate the solid-state kinetics of the reduction of the catalyst. The calculation of apparent activation energies for reduction to MoO_2 might also give information about the reducibility of the samples. Besides the conventional reduction with hydrogen the model catalysts were reduced with propene which represents the reactant during treatment under reaction conditions.

4.2 Experimental

4.2.1 Temperature-programmed reduction (TPR)

Temperature-programmed reduction (TPR) experiments were carried out with a catalyst analyzer from BEL Japan Inc. equipped with a silica glass tube reactor. Samples were placed on silica wool inside the reactor next to a thermocouple. For TPR with hydrogen a gas flow (5% hydrogen in argon) of 60 ml/min was adjusted during reaction. Heating rates used were 5 K/min to 1023 K while hydrogen consumption was measured using a TCD. Additional measurements with 10 and 15 K/min were carried out to investigate the kinetics of reduction. For TPR with propene a gas flow of 40 ml/min (2.5% propene in helium) was adjusted. A second TPR was carried out after an interim temperature-programmed oxidation (TPO) in 5% oxygen in helium. The samples were heated to 773 K with 5 K/min during TPO. A non-calibrated mass spectrometer in a multiple ion detection mode (Pfeiffer Omnistar) at the cell outlet was used for time-resolved detection of gas phase composition. For all measurements 30 mg of samples were used.

4.2.2 X-ray diffraction for isothermal reduction with hydrogen

In situ XRD measurements were conducted on a STOE STADI P diffractometer (θ-θ geometry) using an Anton-Paar *in situ* cell. Isothermal reduction experiments were carried out at distinct temperatures (698 K, 723 K and 748 K). Measurements were performed in reflection mode in a range of 20 – 28.5 $°2\theta$ in steps of 0.03 $°2\theta$ with a sampling time of 4 s/step. A total flow of 100 ml/min was adjusted by mass flow controllers (Bronkhorst). The *in situ* cell was heated to reaction temperature with 10 K/min in helium gas flow. The gas phase composition was switched to 5% hydrogen in helium when isothermal measurements started. A non-calibrated mass spectrometer in a multiple ion detection mode (Pfeiffer Omnistar) at the cell outlet was used for continuously monitoring the gas phase composition.

4.2.3 X-ray diffraction for isothermal reduction with propene

In situ XRD experiments were performed on a STOE STADI P powder diffractometer (Bragg-Brentano geometry) equipped with a secondary monochromator (Cu-K_α radiation) and a scintillation counter operated in the stepping mode. The *in situ* cell consisted of a Bühler HDK S1 high temperature diffraction chamber. Experiments for analysis of phase composition during reduction were carried out in reflection mode in a range of 20 – 28.5 °2θ in steps of 0.04 °2θ with a sampling time of 4 s/step. Measurements for analysis of solid-state kinetics were performed in reflection mode in a range of 25.2 – 27.8 °2θ in steps of 0.046 °2θ with a sampling time of 9 s/step. In situ XRD measurements were conducted under atmospheric pressure with flowing reactants (100 ml/min, 7.5% propene in He). Isothermal reduction with propene was carried out at distinct temperatures (663 K, 673 K, and 683 K).

4.3 Temperature-programmed reduction (TPR) with hydrogen

The evolutions of hydrogen consumptions as a function of temperature during TPR of all MoO_3 samples and its oxide nitrides to 1023 K are shown in **Figure 4-1**. Ball-milling of MoO_3 resulted in different evolutions compared to non-milled MoO_3. Two peaks of hydrogen consumption were identified after ball-milling of MoO_3. Increasing milling time led to a significant shift of first peak to lower temperatures. Conversely, the shift of more intensive second peak was not distinct as the shift of the first peak. Ammonolysis of ball-milled MoO_3 resulted in a shift of most intensive TPR peak to lower temperatures while the onset of hydrogen consumption and the first TPR peak were not affected by ammonolysis. Additionally, peak broadening was observed after ammonolysis.

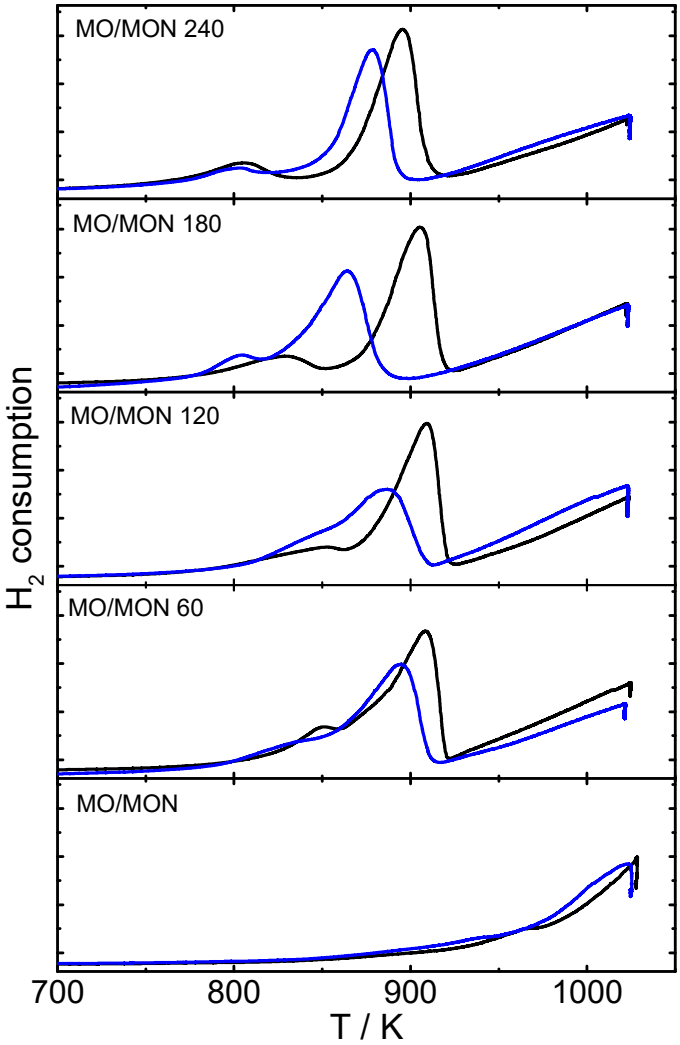

Figure 4-1: *Evolution of hydrogen consumption as a function of temperature during TPR in 5% hydrogen in argon of ball-milled MoO_3 (black) and respective $Mo(ON)_3$ (blue). Milling time of molybdenum oxide was increased from bottom to top.*

For a detailed analysis of the reduction mechanism, TPR of *MO240* was stopped at selected temperatures. The evolution of hydrogen consumption of *MO240* showed the most distinct separation of both peaks. Three XRD measurements were carried out (1) after TPR to the onset of hydrogen consumption, (2) maximum of first peak, and (3) minimum between both peaks (**Figure 4-2**). Four different phases were identified during reduction process. The orthorhombic and monoclinic modifications of Mo_4O_{11} could be observed besides educt MoO_3 and little peak of MoO_2. A quantification of phase compositions of XRD powder patterns revealed a formation of MoO_2 at the beginning of reduction (**Table 4-1**). Phase content of MoO_2 remained almost constant before hydrogen

consumption increased to second maximum. The first maximum of hydrogen consumption was assigned to the formation of Mo_4O_{11}. Orthorhombic Mo_4O_{11} might be formed by reaction of initially formed MoO_2 and MoO_3 above 698 K [125]. Orthorhombic Mo_4O_{11} was transferred into its monoclinic modification. Formation of Monoclinic η-Mo_4O_{11} was also reported in literature [126]. In contrast to previous reports the amount of η-Mo_4O_{11} could not be neglected. Quantitative analysis of XRD powder patterns revealed a phase content of 13%. Afterwards, reaction with hydrogen led to monoclinic MoO_2. In summary, reduction process was described by following reaction equations:

$$3MoO_3 + MoO_2 \rightarrow o - Mo_4O_{11} \tag{4-1}$$

$$o - Mo_4O_{11} \rightarrow m - Mo_4O_{11} + 3H_2 \rightarrow MoO_2 + 3H_2O \tag{4-2}$$

The specific hydrogen consumption was determined by integration of the TCD signal in a distinct temperature range. A calibration of hydrogen consumption for calculation of content of reduced species by 1 oxidation state was established by reducing transition metal oxide references. Afterwards, the content of reduced species during TPR of *MO240* was determined at the same temperatures at which the XRD measurements were carried out (**Table 4-1**). The quantitative results of hydrogen consumption were in good agreement with phase composition of XRD powder patterns. Hence, the quantitative evolution of hydrogen consumption underlined the proposed mechanism for reduction of MoO_3 with hydrogen.

Table 4-1: *Phase composition of XRD powder patterns (**Figure 4-2**) with average valence of molybdenum. Content of reduced species by 1 oxidation state was calculated from hydrogen consumption. Average valence of Mo is noted to each phase.*

	XRD				**H_2 consumption**
	MoO_3 (6)	**o-Mo_4O_{11} (5.5)**	**m-Mo_4O_{11} (5.5)**	**MoO_2 (4)**	**Reduced species by 1 oxidation state**
1	75 %	19 %	---	6 %	17 %
2	35 %	62 %	---	3 %	34 %
3	11 %	71 %	13 %	5 %	45 %

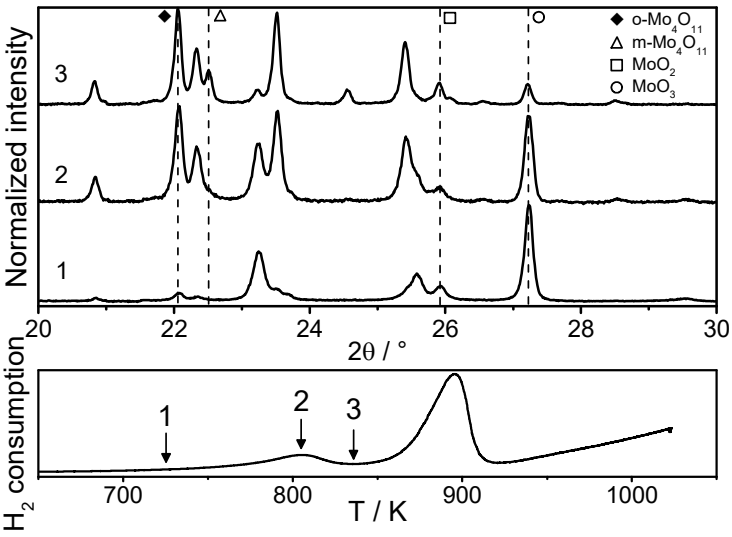

Figure 4-2: *XRD powder patterns (top) of MO240 after TPR in 5% H_2/Ar up to marked temperatures in evolution of hydrogen consumption (bottom). The identified phases are marked by symbols (○ MoO_3, ◆ o-Mo_4O_{11}, Δ m-Mo_4O_{11}, □ MoO_2)* [22,127–129].

TPR of ball-milled MoO_3 and its corresponding oxide nitrides was carried out with varying heating rates. The respective hydrogen consumptions of *MO180* and *MON180* are exemplary shown in **Figure 4-3**. The onset of hydrogen consumption was independent of heating rates while maxima of hydrogen consumption shifted to higher temperatures when heating rate was increased. Shift of the first maxima was similar for oxides and oxide nitrides. The Kissinger method was used to determine the apparent activation energies for the rate-determining step of reduction to MoO_2 [130]. The Kissinger method was used for the evaluation of apparent activation energies of TGA measurements. However, it can be adapted to the analysis of hydrogen consumptions of TPR profiles [131]. The relationship between heating rate and apparent activation energy is given by

$$-ln(\beta T_{max}^2) = -ln\left(\frac{AR}{E_A}\right) + \frac{E_A}{RT} \tag{4-3}$$

and apparent activation energies can be estimated from the slope by plotting $\ln(\beta/T^2_{max})$ vs. $1/T_{max}$.

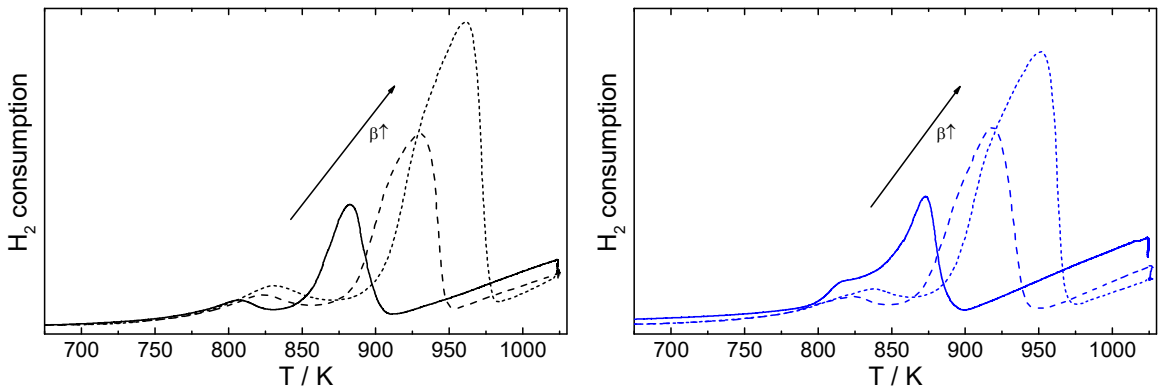

Figure 4-3: *Hydrogen consumption as a function of temperature during TPR with different heating rates of MO180 (left)* and *MON180 (right).*

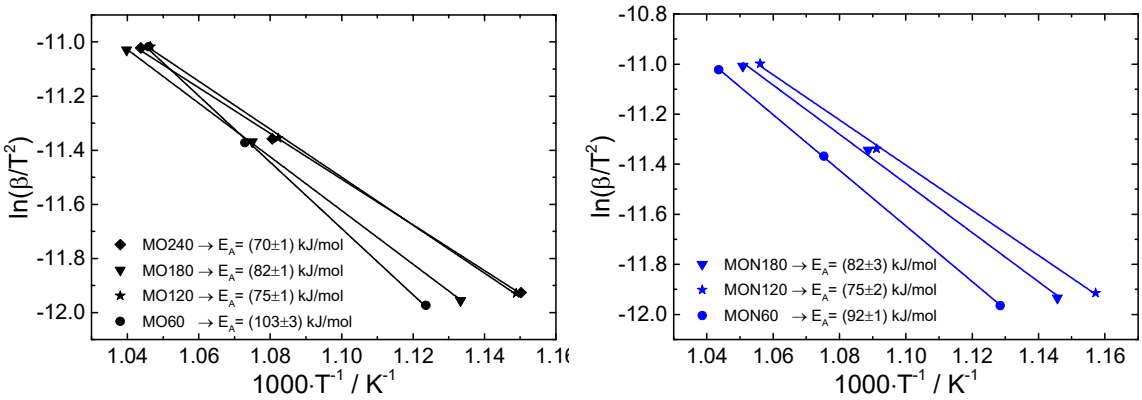

Figure 4-4: *Kissinger presentation of $ln(\beta \cdot T^{-2})$ as a function of T^{-1} of temperature-programmed reduction of ball-milled MoO_3 (left) and its oxide nitrides (right) with hydrogen. Apparent activation energies of reduction to MoO_2 were calculated from the slopes.*

The Kissinger presentation of all investigated oxides and oxide nitrides is shown in **Figure 4-4**. All Kissinger plots resulted in straight lines. Hence, the rate determining step $g(\alpha)$ did not change in the investigated temperature range. Apparent activation energies of the rate determining step were calculated from the slopes. Only *MON60* showed significant varied apparent activation energy after ammonolysis of the corresponding ball-milled oxide. The apparent activation energy was reduced by about 10 kJ/mol. Although the temperatures of maximal hydrogen consumption shifted to lower temperatures a change of apparent activation energies could not be determined. However, a dependency of milling-time on apparent activation energies was determined. The apparent activation energies decreased significantly when the milling-time was increased. Size-strain analysis

of ball-milled MoO_3 revealed a non-linear dependency of milling-time on crystallite sizes. A correlation between apparent activation energy of TPR of ball-milled MoO_3 with hydrogen and volume-weighted crystallite sizes was established (**Figure 4-5**). Such correlations for phase transitions are well-known from the literature [132]. Nevertheless, a more detailed analysis of this correlation was carried out by determining the reduction mechanism. Refinement a model of solid-state kinetics to experimental data of isothermal reduction might lead to mechanistic information.

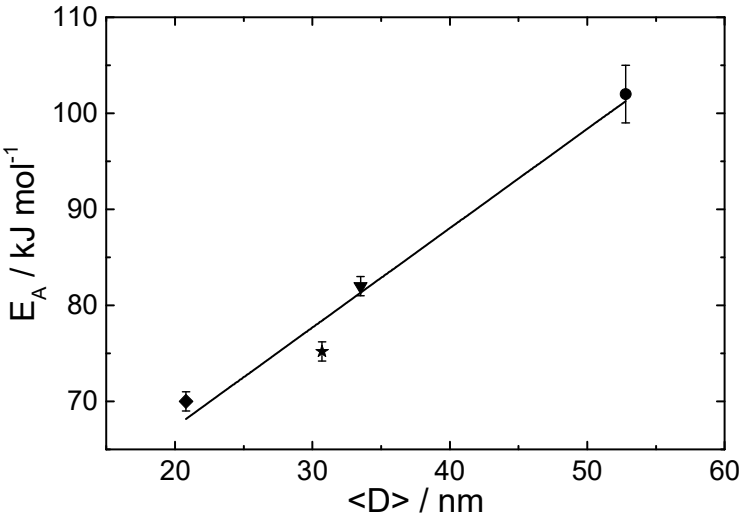

Figure 4-5: *Apparent activation energy of TPR with hydrogen of ball-milled MoO_3 as a function of volume-weighted crystallite size.*

4.4 Temperature-programmed reduction (TPR) with propene

The reducibility of selected ball-milled MoO_3 samples and its corresponding oxide nitride was investigated by temperature-programmed reduction with propene. After first TPR all samples were re-oxidized by TPO in 5% oxygen in helium. Afterwards, a second TPR was carried out to investigate the influence of a removal of nitrogen on reducibility. The evolution of conductivities during thermal treatment in 5% oxygen in helium was associated with the complete removal of nitrogen. **Figure 4-6** shows the evolution of ion currents *m/e* 18 (water) and *m/e* 52 (acrolein) during both TPR of all samples. Water and acrolein represent the major products of selective oxidation of propene. Its formation might give information about the availability of lattice oxygen of catalysts. The simultaneous formation of water and acrolein was observed in a temperature range from

643 K to 698 K and could be associated with the reduction of the samples. Ball-milled oxide nitrides showed an improved reducibility during first TPR with propene compared to the corresponding oxides. However, the maximum was independent of milling-time of MoO_3. Only the onset of reduction of *MO240* was slightly shifted to higher temperatures.

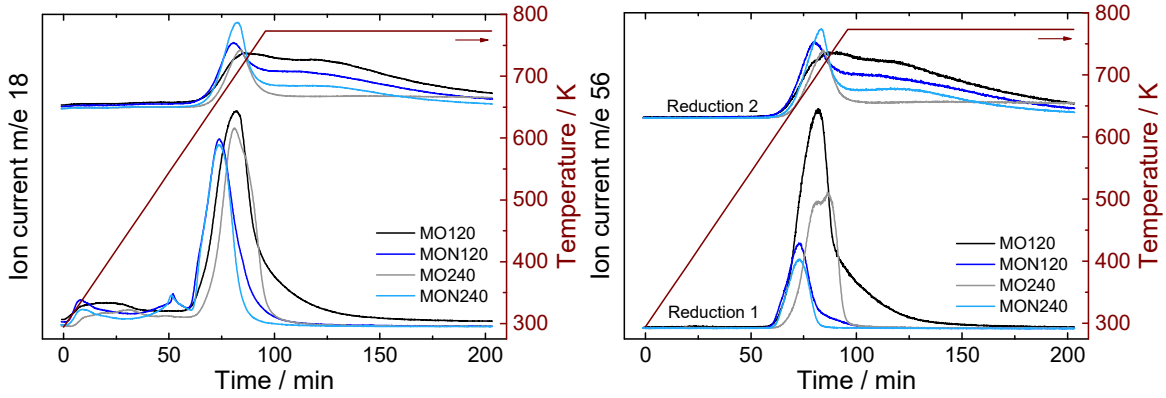

Figure 4-6: *Evolution of m/e 18 (left, H_2O) and m/e 56 (right, acrolein)* during TPR of *MO120, MO240 and its corresponding oxide nitrides with 2.5% propene in helium (bottom) and TPR after meanwhile oxidation of products of first TPR (top).*

The peak profile was significantly broadened during a second TPR with propene. All temperatures of the maximum of the peak were shifted to higher temperatures compared to first TPR. Nevertheless, a slight shift of temperatures of oxide nitrides to lower temperatures was determined. Hence, slight influences on reducibility were preserved despite interim oxidation of the samples. The observed shift to higher temperatures comparing both reductions might be explained by considering the photochromism of MoO_3. Different models were developed to explain the photochromism of MoO_3 [120]. Molybdenum oxides are well-known to form substoichiometric oxides (MoO_{3-x}) resulting in the formation of defects. Ball-milling and ammonolysis led to coloration of molybdenum oxide associated with formation of defects (**chap. 3.5**). Deb related the coloration of molybdenum oxide films to the formation of F-like centers. The trapped electrons in these centers might result in transitions in the visible region which were responsible for the color of the material. The formation of F-like centers was related to oxygen vacancies. Additionally, the formation of Mo^{5+} was observed [115]. Otherwise, ball-milling of MoO_3 was associated with reduction Mo^{6+} to Mo^{5+}. Corresponding IVCT transitions were detected in DR-UV-Vis spectra (**chap. 3.5**).

Nevertheless, both approaches resulted in formation of new bands above the valence band [82]. A schematic presentation is given in **Figure 3-12**. Upon heating the samples in oxygen, Mo^{5+} centers were oxidized to Mo^{6+}. The stoichiometry was restored by replenishing the defects. Consequently, the formation of defects like oxygen vacancies could be correlated to improved oxygen availability. However, TPO in 5% oxygen seemed not to be sufficient to destroy all additional defects caused by ammonolysis of ball-milled MoO_3.

The evolution of ion current *m/e* 18 during first TPR showed various peaks without simultaneous formation of acrolein at lower temperatures. Significant differences between ball-milled oxides and the corresponding oxide nitrides were determined. A more detailed characterization of thermal stability of oxide nitrides was carried out by analyzing ion currents *m/e* 14, 16, 17, 18 and 28 during first TPR (**Figure 4-7**). The first peak of *m/e* 18 at about 315 K was attributed to the removal of water which might be adsorbed at the surface of the samples. A broad maximum of *m/e* 16 and 17 was detected at about 400 K. In addition, a shoulder of both traces was determined at about 340 K. In this temperature range the removal of nitrogen occurred. The corresponding ion currents *m/e* 16 and 17 indicated the removal of NH groups. This was corroborated by FTIR spectra which showed N-H bending and stretching modes (**chap. 3.4**). Two different peaks indicated the existence of different NH species in MoO_3-type oxide nitrides. The shoulder at 340 K was assigned to removal of weak adsorbed NH_3 at the surface. However, the more intensive peak at about 400 K could be attributed to the removal of NH groups which were incorporated by substituting terminal oxygen ions in the layers of MoO_3. This assumption was in agreement with results of FTIR spectra and ammonolysis process of MoO_3 in the literature [49]. The corresponding peaks of *m/e* 16, 17 and 18 at about 530 K indicated the removal of water before nitrogen was removed at 590 K from the oxide nitrides. Hence, nitrogen ions might also be incorporated without formation of NH groups. The number of different nitrogen species incorporated in MoO_3 corroborated the proposed processes during ammonolysis of ball-milled MoO_3 illustrated in **chap. 3.7**. Apparently, nitrogen was fully removed during first TPR due to missing peaks of ion currents *m/e* 16 and 17 during TPO or following TPR. Additionally, a slight formation of

water was detected up to 450 K during TPR of ball-milled MoO_3. The possible existence of molybdenum oxide hydrates was suggested due to respective FTIR spectra.

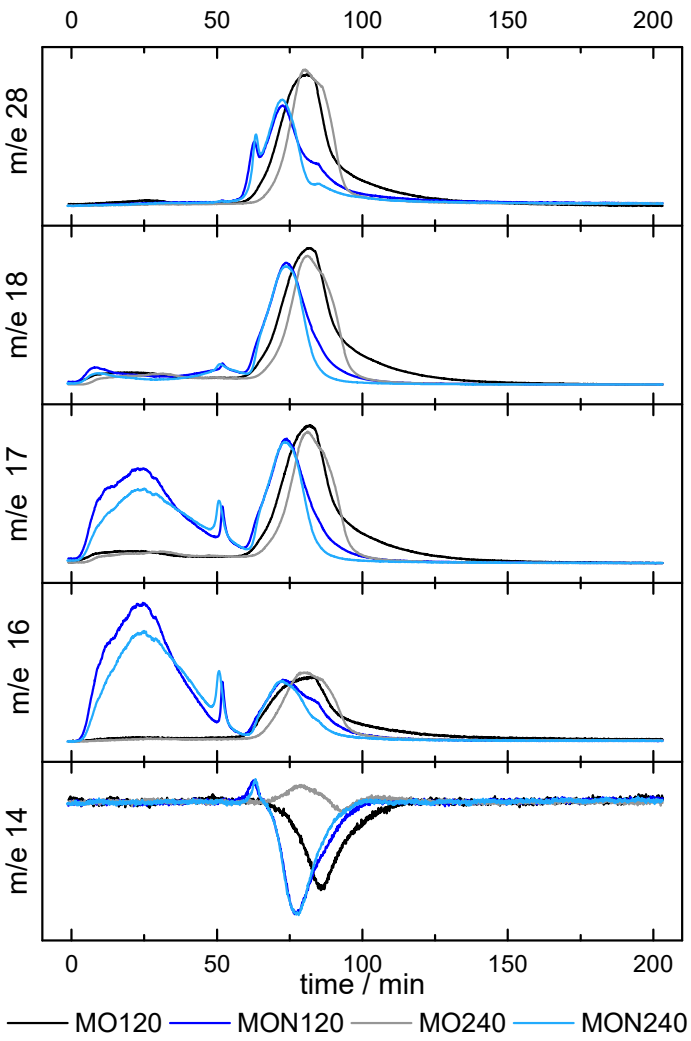

Figure 4-7: *Evolution of ion currents m/e 14, 16, 17, 18, 28 during TPR of MO120, MO240 and its corresponding oxide nitrides with 2.5% propene in helium up to 773K.*

4.5 Fundamentals of solid-state kinetic models

Analysis of solid-state reactions and their kinetics is important for understanding reaction mechanism [133,134]. In addition, investigations of reduction kinetics of solid oxides are of interest in research on heterogeneous catalysts [135]. The rate of a solid-state reaction can be generally described by

$$\frac{d\alpha}{dt} = k(T)f(\alpha) \tag{4-4}$$

with the absolute temperature *T*, the temperature-dependent rate constant *k(T)* and the reaction model *f(α)*. A suitable description of the temperature dependence of the rate constant is provided by the Arrhenius equation. Substitution of *k(T)* in **eq. (4-4)** yields

$$\frac{d\alpha}{dt} = Ae^{-(E_A/RT)}f(\alpha) \tag{4-5}$$

where *A* is the preexponential factor, E_a is the activation energy for the rate-determining step and *R* is the gas constant. **Eq. (4-5)** can be transferred in the integral reaction model *g(α)* by separating variables and integrating:

$$g(\alpha) = \int_0^{\alpha} \frac{d\alpha}{dt} = Ae^{-(E_A/RT)}t. \tag{4-6}$$

The analysis of reaction kinetic can be carried out by model-dependent or model-independent methods. The whole reaction kinetics are completely specified by the reaction model and the two Arrhenius parameters. These three parameters are often called the kinetic triplet which is not available by using model-independent methods. Without knowledge of these parameters no accurate description of kinetics can be established. Hence, a model is usually needed for complete description [136]. The model-dependent analysis results in single apparent activation energy for the rate-determining step. This activation energy is independent of degree of conversion. These used models represent theoretical descriptions to explain the experimental data [137]. Many models were proposed by assuming a certain mechanism for the rate-determining step. A classification of reaction models can be carried out based its mechanistic assumptions. These models can be divided in nucleation, diffusion, reaction order and geometrical contraction models. Based on the shape of respective α-traces, models can be classified as sigmoidal, acceleratory, linear or decelerator. Hence, the conversion fraction α is the needed parameter for analyzing the rate-determining step. The measured parameter of the analytical method must be able to be transformed in conversion fraction α. X-ray diffraction represents a suitable analytical method for studying solid-state kinetics [35,138]. The used models will be explained in detail in the following.

4.6 Isothermal reduction with hydrogen

Reducibility of ball-milled MoO_3 and its oxide nitrides during isothermal reduction with hydrogen was investigated by *in situ* XRD. Evolution of XRD powder patterns of *MO60* is shown in **Figure 4-8**. Formation of MoO_2 was observed and the intensity of three most intensive diffraction peaks of MoO_3 decreased. A small diffraction peak at 22.1 °2θ was attributed to most intense reflection of orthorhombic γ-Mo_4O_{11}. Intermediate formation of γ-Mo_4O_{11} during isothermal reduction was neglected. Otherwise, the formation of γ-Mo_4O_{11} was dependent on milling-time of MoO_3. In agreement with results of TPR with hydrogen the formation of γ-Mo_4O_{11} was most pronounced for *MO240*. A linear combination refinement of pure MoO_3 and MoO_2 resulted in extent of reduction α as a function of time (**Figure 4-9**). A linearization of the extent of reduction was carried out by using the integral form of contracting area model (R2) [137]:

$$g(\alpha) = 1 - (1 - \alpha)^{1/2} = kt. \tag{4-7}$$

A suitable linearization of evolutions of α-traces could not be achieved by the application of other nucleation or diffusion models. Reaction rate constants of each temperature were calculated from the slopes of linear regressions. The R2 model assumes a rapid nucleation on the surface of the particle. Regardless of the geometry of the particle the following relationship is applicable:

$$r = r_0 - kt. \tag{4-8}$$

R2 model simplifies the particle shape to a cylinder. A schematic drawing of R2 model and the nucleation process is given in **Figure A 2-1**. **Eq. (4-7)** can be derived from a relationship between conversion fraction and the volume of a cylinder hpr^2. A detailed derivation can be found elsewhere [137].

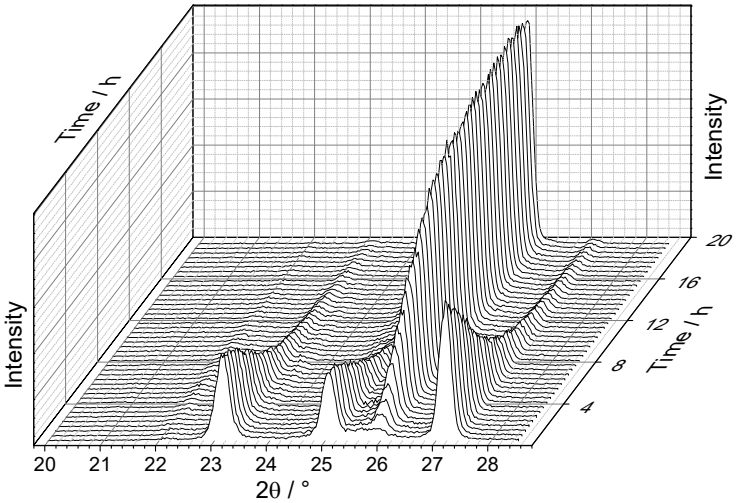

Figure 4-8: *Evolution of XRD powder patterns of MO60 during isothermal reduction in 5% H_2 / He at 748 K.*

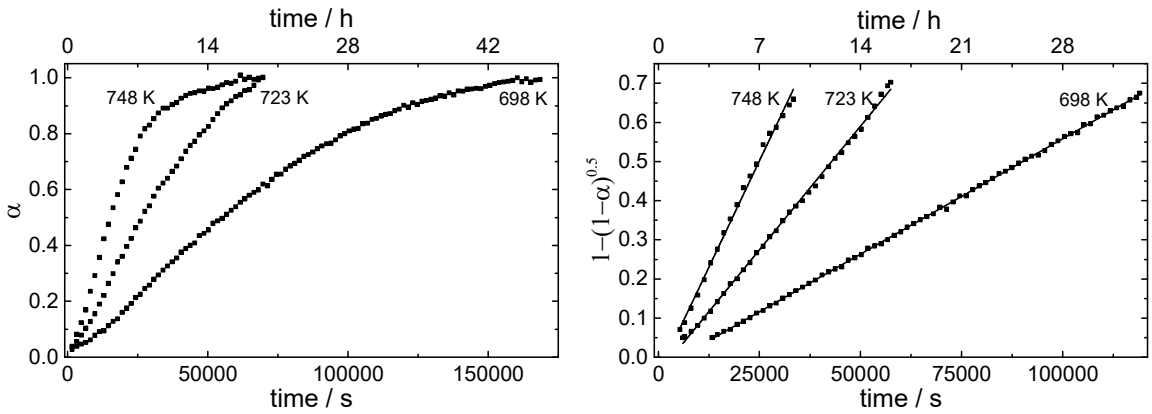

Figure 4-9: *Left: Evolution of conversion degree of MO60 during isothermal reduction at 698 K, 723 K and 748 K with hydrogen. Right: Plotting $1-(1-\alpha)^{0.5}$ as a function of time for calculation of reaction rate constants from the slopes of linear regressions.*

An Arrhenius-type presentation of reactions rate constants of isothermal reduction of ball-milled MoO_3 and its corresponding oxide nitrides is shown in **Figure 4-10**. The apparent activation energies of formation of MoO_2 were calculated from the slopes according to **eq. (4-3)**. The ammonolysis of ball-milled MoO_3 led to a decrease of apparent activation energies of about 10 kJ/mol. The decrease was consistent for all samples independent of milling-time.

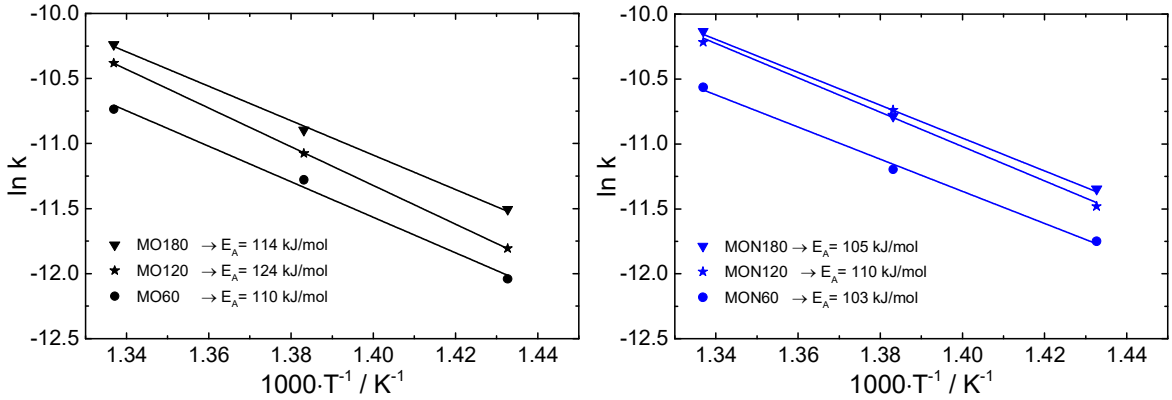

Figure 4-10: *Arrhenius-type presentation of reaction rate constants of isothermal reduction of ball-milled MoO_3 (left) and its oxide nitrides (right) with hydrogen. Apparent activation energies of reduction to MoO_2 were calculated from the slopes.*

4.7 Isothermal reduction with propene

In situ XRD experiments were carried out to investigate the reducibility of ball-milled MoO_3 and its corresponding oxide nitrides. The samples were isothermally reduced with propene at 663, 673 and 683 K. Evolution of *in situ* XRD powder patterns of *MO60* during isothermal reduction in 7.5% propene in He at 673 K is shown in **Figure *4-11***. The intensity of three characteristic diffraction peaks of MoO_3 decreased during isothermal treatment while most intensive diffraction peak of MoO_2 appeared. In contrast to isothermal reduction with hydrogen the formation of γ-Mo_4O_{11} was not observed. TPR experiments with hydrogen revealed an increased formation of γ-Mo_4O_{11} when molybdenum oxides were ball-milled for longer times. Only little diffraction peaks of γ-Mo_4O_{11} could be detected during isothermal reduction with propene of *MO240*. Subsequently, formation of γ-Mo_4O_{11} during isothermal reduction was neglected.

The parameters of *in situ* XRD experiments were optimized for analysis of solid-state kinetics to result in time measuring of 10 minutes for each pattern. Therefor the step width and angular range were reduced. A linear combination refinement of diffraction patterns of pure MoO_3 and MoO_2 resulted in extent of reduction α as a function of time. According to **eq. (4-7)** a linearization of extent of reduction was carried out by using the integral form of the contracting area model (R2) [137]. **Figure 4-12** shows the evolutions of extent of reduction and its linearization during isothermal reduction of *MO180* with

propene. The reaction rate was increased with temperature. The respective plots of $1-(1-\alpha)^{1/2}$ as a function of time could be well refined by a straight line. Compared to other typically used reaction models the application of R2-model led to the best goodness of fit. The reaction rate constants were calculated from the slope for each sample and temperature.

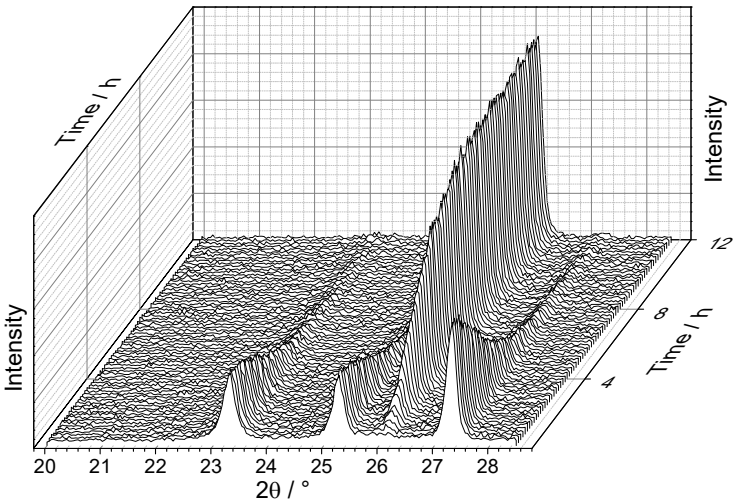

Figure 4-11: *Evolution of XRD powder patterns of MO60 during isothermal reduction in 7.5% propene in He at 673 K.*

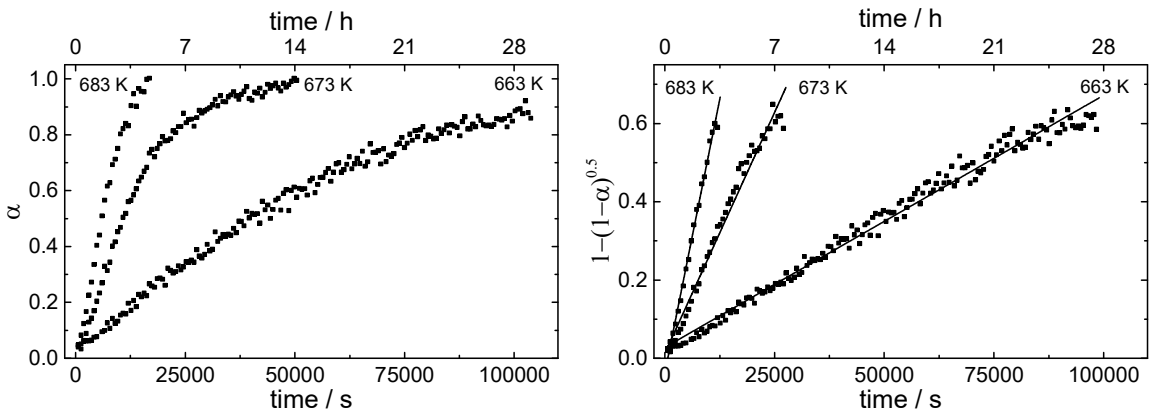

Figure 4-12: *Left: Evolution of conversion degree of MO60 during isothermal reduction at 698 K, 723 K and 748 K with propene. Right: Plotting $1-(1-\alpha)^{1/2}$ as a function of time for calculation of reaction rate constants from the slopes of linear regressions.*

The dependence of reaction rate constants on temperature during isothermal reduction of ball-milled MoO_3 and its corresponding oxide nitrides with propene is shown in **Figure 4-13**. The reaction rate constants were slightly increased after ammonolysis of

respective ball-milled MoO_3. Hence, the incorporation of nitrogen resulted in an improved reducibility with propene. The apparent activation energies for the rate-determining step of reduction from MoO_3 to MoO_2 were calculated from the slopes of Arrhenius-type presentations using **eq. (4-3)**. The resulting apparent activation energies were in a range of 339-480 kJ/mol for ball-milled MoO_3 and 310-353 kJ/mol for MoO_3-type oxide nitrides. The apparent activation energies decreased significantly with longer milling-time of MoO_3. A correlation between apparent activation energies of reduction to MoO_2 and area-weighted and volume-weighted crystallite sizes of ball-milled MoO_3 and MoO_3-type oxide nitrides was established (**Figure 4-14**). The decrease in crystallite size coincided with an increase of surface area. Crystallite size effects on reaction rate are well-known [137,139]. According to R2-model the reduction of MoO_3 to MoO_2 proceeded by a rapidly nucleation at the surface of the crystal. Increasing the surface area of the crystal led to an increase in reaction centers for adsorption of propene. Hence, the reduction may be facilitated resulting in decreased activation energy. Additionally, the rate of reaction of MoO_3 was increased by decreasing size of crystallites.

The incorporation of nitrogen in ball-milled MoO_3 resulted in a significant decrease of apparent activation energies of reduction to MoO_2. The decrease of apparent activation energies confirmed the enhanced reducibility shown by reduction with hydrogen. However, the decrease of apparent activation energies was more pronounced for the reduction with propene. The decrease of apparent activation energies was slightly dependent on crystallite sizes. Larger crystallites led to an intensified decrease of apparent activation energies. This dependence might be attributed to different stabilities of MoO_3-type oxide nitrides. Conductivity measurements revealed a higher thermal stability of MoO_3-type oxide nitrides consisting of larger crystallites in an oxidizing atmosphere (**chap. 3.6**).

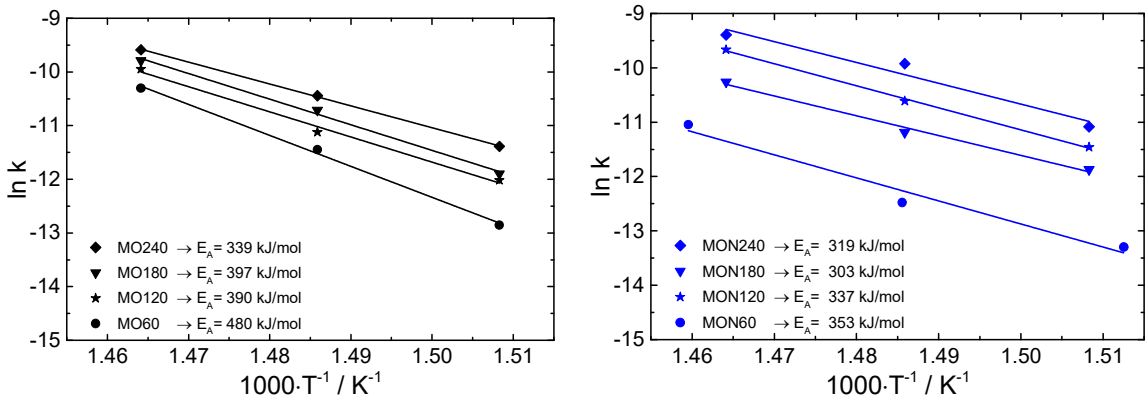

Figure 4-13: *Arrhenius-type presentation of reaction rate constants of isothermal reduction of ball-milled MoO_3 (left) and its oxide nitrides (right) with propene. Apparent activation energies of reduction to MoO_2 were calculated from the slopes.*

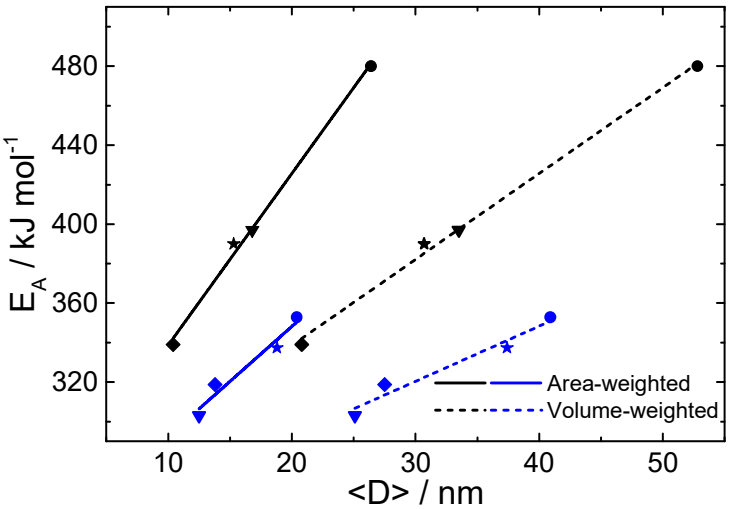

Figure 4-14: *Apparent activation energy of isothermal reduction with propene of ball-milled MoO_3 (black) and its oxide nitrides (blue) as a function of area-weighted and volume-weighted crystallite size. The crystallite sizes were calculated according to description in* ***chap. 3.3.2****.*

4.8 Summary

The reducibility of ball-milled MoO_3 and its corresponding oxide nitrides was investigated by temperature-programmed and isothermal reduction experiments. The experiments were carried out with hydrogen as well as propene as reducing agent. *In situ* XRD represented a suitable method for analyzing of solid-state kinetics during isothermal reduction. TPR and isothermal experiments revealed a dependence of apparent activation energy on crystallite size of ball-milled MoO_3 which was independent of the reducing agent. The R2-reaction model described the isothermal reduction. Hence, ball-milling increased the number of reaction centers. The increased number of reaction centers led to a faster reaction of MoO_3 to MoO_2. The reaction mechanism during TPR with hydrogen was determined by XRD measurements. The formation of Mo_4O_{11} was not influenced by ammonolysis MoO_3. Conversely, the formation of MoO_2 was significantly shifted to lower temperatures. Compared to ball-milled MoO_3 the apparent activation energies of reduction of MoO_3-type oxide nitrides to MoO_2 decreased. The extent of diminution of apparent activation energies during isothermal reduction with propene decreased with decreasing crystallite sizes of the samples. Investigations on the thermal stability of MoO_3-type oxide nitrides revealed that different strong bounded NH groups were formed during ammonolysis of ball-milled MoO_3. The influence of ball-milling and ammonolysis on reducibility was correlated to the formation of defects such as oxygen vacancies or Mo^{5+} centers.

5 *In situ* characterization during treatment under reaction conditions of molybdenum oxides with various crystallinity and its oxide nitrides

5.1 Introduction

The previous chapter of this work showed a significant influence of incorporation of nitrogen on the electronic structure and reducibility of MoO_3. Catalytic performance of molybdenum oxides with various crystallinity and its corresponding oxide nitrides will be investigated in this chapter. Additionally, previous investigations on thermal stability of MoO_3-type oxide nitrides under oxidizing and reducing conditions revealed a dependency of thermal stability on crystallinity. Therefore, *in situ* DR-UV-Vis experiments will be carried out to investigate the thermal stability of oxide nitrides during catalytic testings. DR-UV-Vis spectroscopy represents a well-known method as a suitable method for *in situ* investigations during selective oxidation of propene. Furthermore, defects and modifications of electronic structure due to modification of anion lattice of MoO_3 were significantly detected by DR-UV-Vis spectroscopy. Changes in electronic structure will be correlated to the thermal stability of MoO_3-type oxide nitrides. Establishing structure-function correlations was enabled by the modification of crystallinity and anion lattice.

5.2 Experimental

5.2.1 In situ DR-UV-Vis

In situ DR-UV-Vis measurements were conducted on a two-beam spectrometer (V670, JASCO) using a Praying Mantis™ *in situ* cell (Harrick Scientific Products, Inc.). Powder samples were measured in the spectral region of 220–890 nm. Boron nitride (Alfa Aesar, 99.5%) was used for sample dilution and as reflectance standard for baseline correction. *In situ* measurements were conducted in 5% propene (Linde Gas, 10% propene (3.5) in He (5.0)) and 5% oxygen (Linde Gas, 20% O_2 (5.0) in He (5.0)) in helium (Air Liquide, 6.0) in a temperature range from 295 K to 698 K at a heating rate of 4.25 K/min. The total gas flow was adjusted to 40 ml/min by using mass flow controller (Bronkhorst). The gas atmosphere was analyzed using an online mass spectrometer (Omnistar, Pfeiffer) in a multiple ion detection mode. The DR-UV-Vis spectra were transferred into the Kubelka-Munk function, $F(R_\infty)$, according to **eq. (2-9)**.

5.2.2 Catalytic characterization

Catalytic activities were measured in a conventional fixed bed reactor connected to an online gas chromatography system (CP-3800, Varian). The fixed-bed reactor consisted of a SiO_2 tube (length 30 cm, inner diameter 9 mm) placed vertically in a tube furnace. The sample was placed on a frit in the center of the isothermal zone. The catalyst bed in the reactor was approximately 2 cm in height. To achieve a constant volume in the reactor and to quench thermal effects, catalyst samples (about 80 mg) were diluted with boron nitride (hexagonal, Alfa Aesar, 99.5%) to result in an overall sample mass of 250 mg. To ensure differential reaction conditions, the reactor was operated at low propene conversion levels below 10 %.

Hydrocarbons and oxygenated reaction products (acetic aldehyde, propionic aldehyde, acetone, acrolein, isopropyl alcohol, n-propanol, allyl alcohol, acetic acid, propionic acid, acrylic acid, acrylonitrile, acetonitrile, propionitrile) were analyzed using a Carbowax 52CB capillary column, connected to an Al_2O_3/MAPD capillary column, and a

fused silica restriction (25 m,·0.32 mm). Each column was connected to a flame ionization detector. Permanent gases (O_2, N_2, CO_2, CO) were separated and analyzed using a Varian CP-3800 permanent gas analyzer connected to a thermal conductivity detector.

Reactant gas flow rates of oxygen, propene, and helium were adjusted through separate mass flow controllers (Bronkhorst) to a total flow of 40 ml/min. A mixture of 5% propene and 5% oxygen in helium was used for catalytic tests at 673 K. The reactor was heated to 673 K with 16.7 K/min in reaction gas flow. Additionally, a mass spectrometer (Omnistar, Pfeiffer) was connected to continuously monitored reactant and product gas composition.

Conversion *X* of the key component *k* and selectivity *S* towards product p_n were calculated from the measured volume fractions, *Vol%* by

$$X_k = \frac{Vol\%(k)_{in} - Vol\%(k)_{out}}{Vol\%(k)_{in}} \tag{5-1}$$

$$S_{pn} = \frac{a_{pn}}{a_k} \frac{(Vol\%(k)_{out} - Vol\%(k)_{in})}{\sum\left(\frac{a_{px}}{a_k} Vol\%(p_x)_{out}\right)} \tag{5-2}$$

with the number of carbon atoms in the desired product (a_{pn}) and in propene (a_k = 3). The carbon balances were determined by the equation

$$\frac{Vol\%(C)_{out}}{Vol\%(C)_{in}} = \frac{\sum\left(a_{px} \cdot Vol\%(p_x)_{in} + 3 \cdot Vol\%(C_3H_6)_{out}\right)}{3 \cdot Vol\%(C_3H_6)_{in}} \tag{5-3}$$

to ensure the significance of results by quantifying all formed products. Carbon balances were always higher than 0.99. The experimental error of reaction rates and selectivities was estimated from the relative errors of reactant gas flow rates and catalyst sample masses. The reaction rates for one compound were calculated from **eq. (5-4)**:

$$r_i = \frac{X_i \cdot Vol\% \cdot \dot{V}}{m_{cat} \cdot V_m \cdot 60}. \tag{5-4}$$

5.3 Catalytic performance

Catalytic performance in selective propene oxidation was investigated at 673 K. Reaction rates for propene conversion and acrolein formation at 673 K as a function of time on stream are shown in **Figure 5-1**. The respective rates were calculated based on the initial weight of the catalyst. The reaction rates for propene conversion showed a significant increase after ball-milling of MoO_3. Already short milling-times were enough to increase the reaction rate for propene conversion by a factor of ~4. This trend was consistence with the evolution of crystallite sizes in **chap. 3.3.3**. The most distinct change in crystallite size was determined after 60 minutes. The changes during the following 180 minutes were less significant. Little effects of time on stream on the reaction rate for propene conversion of ball-milled MoO_3 were determined. All samples exhibited a slight deactivation of propene conversion. However, the increasing activation due to varied crystallinity was preserved after incorporation of nitrogen. A slight increase of reaction rate for propene conversion was determined after incorporation of nitrogen at the beginning of the treatment under reaction conditions. Compared to molybdenum oxides a slightly more intense deactivation of MoO_3-type oxide nitride catalysts was observed. The reaction rates for propene conversion were similar to those of molybdenum oxides after 12 hours treatment under reaction conditions. This similar trend might be due to instability of MoO_3-type oxide nitrides. The removal of nitrogen was observed at lower temperatures than 673 K in an oxidizing or reducing atmosphere. Little differences of conductivities were determined after removal of nitrogen (**chap. 3.6**).

The acrolein formation rates of molybdenum oxides and MoO_3-type oxide nitrides increased with decreasing crystallite size. This corroborated the increased catalytic activity after ball-milling shown by reaction rate for propene conversion. In contrast to the reaction rate for propene conversion, the acrolein formation rate remained unvaried after 2 hours treatment under reaction conditions. The incorporation of nitrogen led to an increase of the acrolein formation rate. This increase was preserved during 12 hours treatment under reaction conditions.

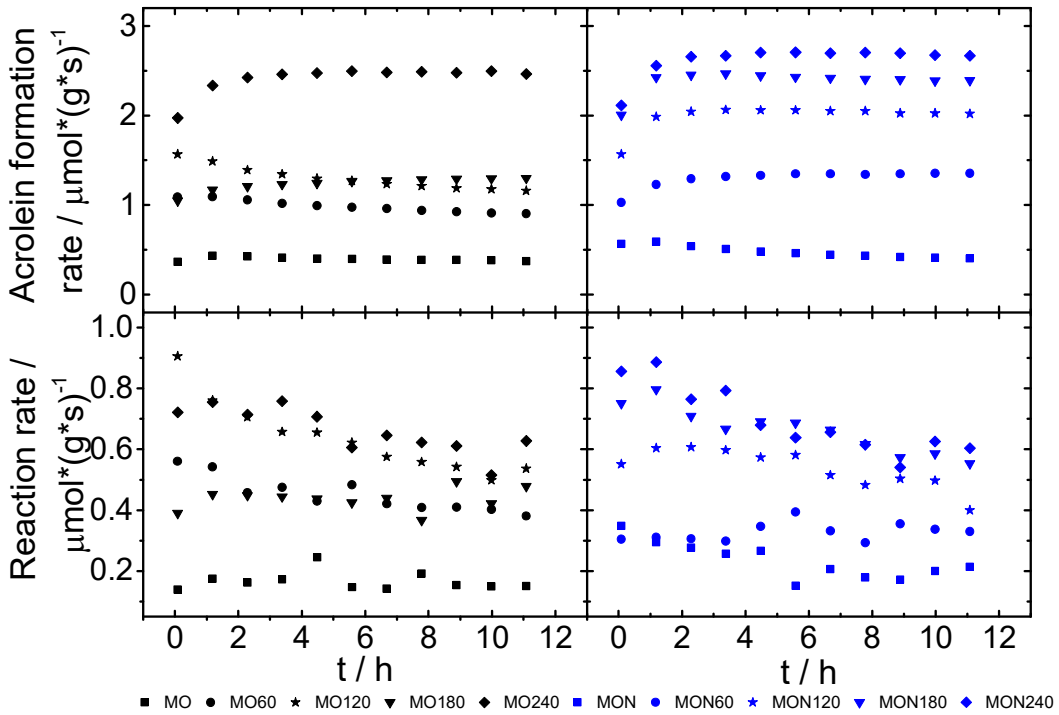

Figure 5-1: *Reaction rates for propene conversion (bottom) and acrolein formation (top) based on catalyst's initial weight as a function of time on stream at 673 K in 5 % propene and 5 % oxygen. Left: Ball-milled molybdenum oxides, right: MoO_3-type oxide nitrides.*

Selectivities towards acrolein and CO_X were determined for each sample at 673 K and at similar propene conversions after 12 hours time on stream (**Figure 5-2**). Selectivity towards acrolein increased significantly after incorporation of nitrogen. On the contrary, selectivity towards total oxidation products CO_X decreased in a similar degree as the selectivity towards acrolein increased. The incorporation of nitrogen in MoO_3 might lead to a preferred formation of selective oxidation products. Furthermore the formation of different minor products was determined. Ball-milling of MoO_3 resulted in significant decrease of selectivities towards minor oxygenates from 27 % to 13%. Changes of selectivities of minor products might be explained by considering various possible pathways of selective oxidation of propene. **Figure 5-3** shows a schematic presentation of various reaction pathways for selective oxidation of propene [140,141]. In a first step one of three alcohols might be formed as intermediates. Afterwards, the alcohols were oxidized to the corresponding aldehydes (acrolein (B), propionic aldehyde (C) and acetone (A)).

Oxidation of the aldehydes led to the formation of acetaldehyde or acetic acid. The formation of acrylic acid could not be detected. Determining selectivities towards minor products revealed a significant decrease of formation in isopropyl alcohol, acetone and acetic acid after incorporation of nitrogen (**Figure 5-2**, bottom right). These minor products represented pathway A. Acetic acid was the mainly formed product of pathway A. Hence, isopropyl alcohol and acetone might be considered intermediate products. Nevertheless, acetaldehyde was determined as the minor product with highest selectivity (pathway C). In agreement with pathway A the corresponding C_3 alcohol and aldehyde were formed in small contents. Selectivities to minor products of pathway C were dependent on milling-time of MoO_3. Conversely, consecutive ammonolysis of ball-milled MoO_3 did not influence the formation of minor products of pathway C. A decreasing crystallite size of MoO_3 led to a decreased occurrence of pathway C. Hence, the formation of acetaldehyde might be very sensitive to the structure of MoO_3. The structure sensitivity of reactions on MoO_3 is well-known from the literature [38].

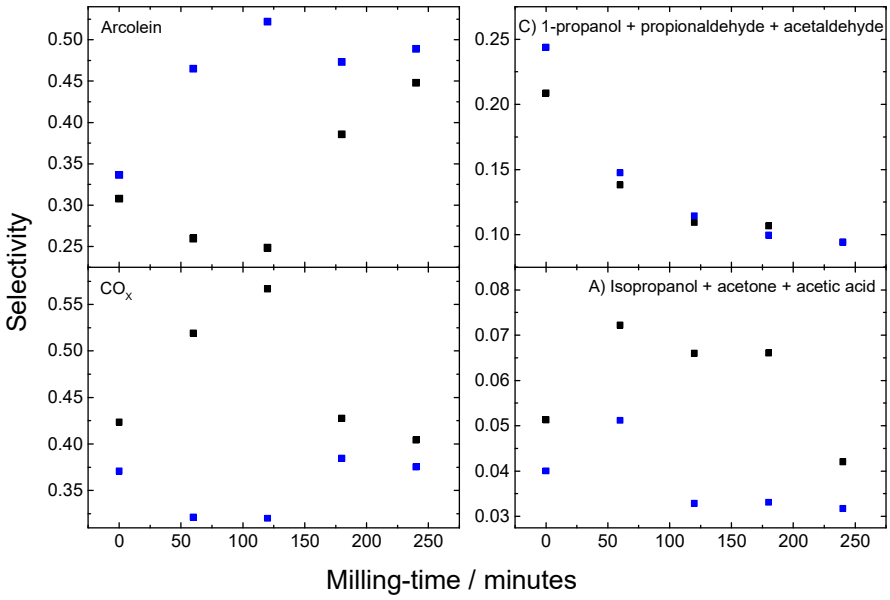

Figure 5-2: *Left: Selectivity towards acrolein (top), CO_X (bottom) as a function of milling-time of MoO_3 and MoO_3-type oxide nitrides. Right: Sum of different selectivities towards minor products of all samples according to different reaction pathways (**Figure 5-3**). All selectivities were determined at 673 K and 12 hours time on stream.*

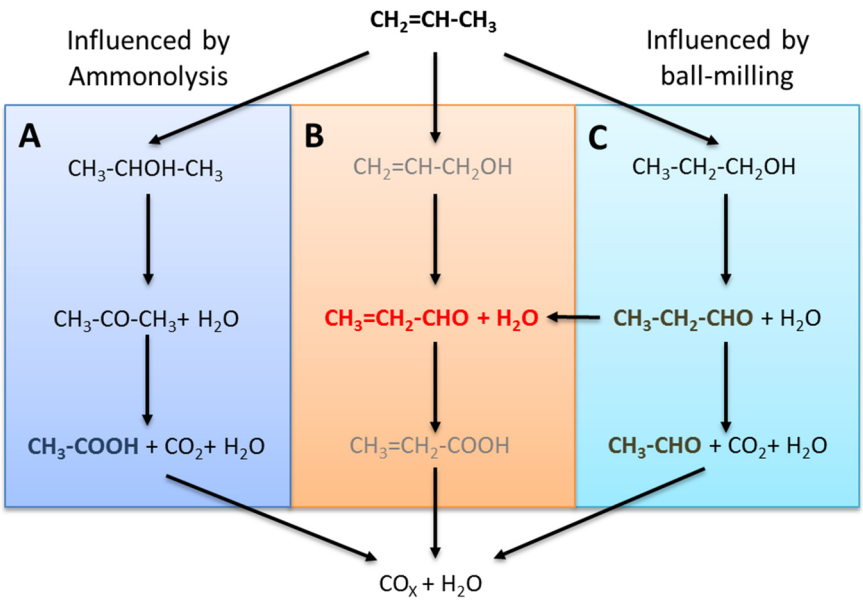

Figure 5-3: *The main oxygenate products of the partial oxidation of propene* [140,141].

The stability of MoO_3-type oxide nitrides is a crucial factor for evaluating the influence of nitrogen incorporation on catalytic performance. **Figure 5-4** shows the evolution of ion currents m/e 14, 15, 17, 18 and 28 as a function of temperature during thermal treatment of *MON120* and *MON 240* to 673 K. The ion currents were normalized to the ion current of helium. At about 400 K removal of water (*m/e* 17 and 18) was determined. Two broad maximums of *m/e* 17 at about 450 K and 550 K indicated the removal of NH_X groups from the MoO_3-type oxide nitrides. This removal of NH_X groups corroborated the results of FTIR spectra of MoO_3-type oxide nitrides. Additionally, the ion currents m/e 14 and 15 showed the corresponding maximums. A significant increase of *m/e* 28 at about 600 K was associated with the formation of CO due to beginning catalytic activity. At the same temperature the formation of water was detected. Water is one of the main products in selective oxidation of propene. However, a significant peak of *m/e* 28 was determined at 635 K during thermal treatment of *MON240*. In addition, the ion current *m/e* 14 revealed a peak at 635 K. Hence, this peak was due to the removal of nitrogen. *MON120* showed a similar trend shifted to higher temperatures by 10 K. Consequently, the thermal stability of MoO_3-type oxide nitrides might be dependent on the crystallite size. In summary, these results corroborated the results of impedance

spectroscopy (**chap. 3.6**). Investigations on the thermal stability in 5% oxygen in helium resulted in a dependency of thermal stability on crystallite size. Additionally, removal of nitrogen occurred over a wide temperature range of about 150 K.

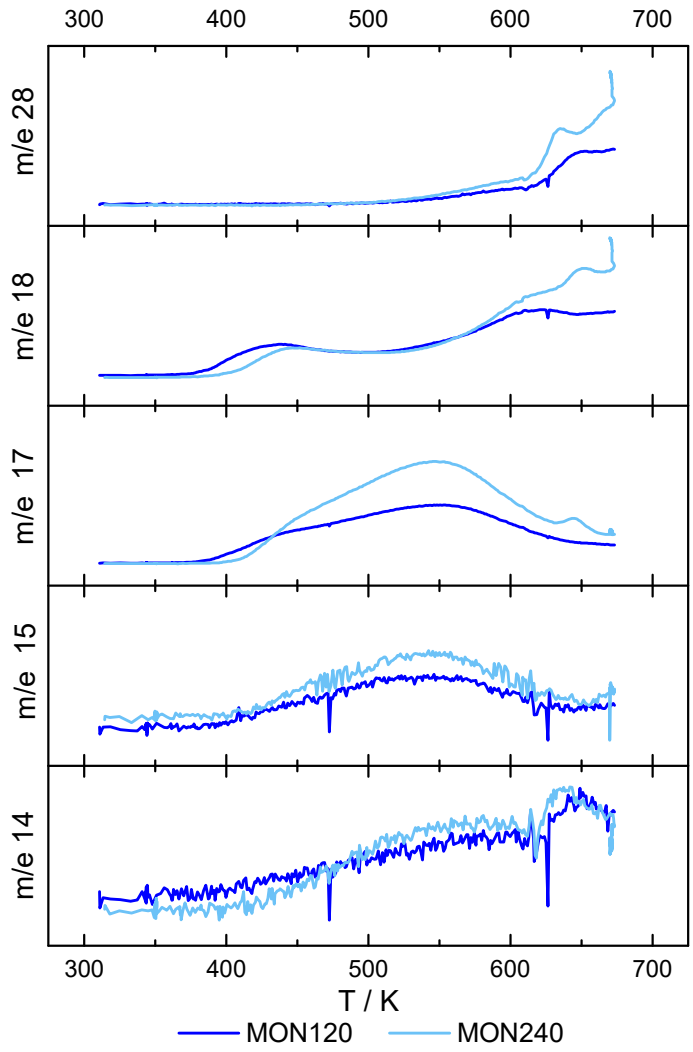

Figure 5-4: *Evolution of ion currents m/e 14, 15, 17, 18 and 28 as a function of temperature during heating of MON120 and MON 240 to 673 K before catalytic performance was investigated. The samples were heated in 5% propene and 5% oxygen in helium. Ion currents were normalized to signal of m/e 4 (helium).*

5.4 *In situ* DR-UV-Vis

In-situ spectroscopic analysis of thermal stability during treatment under reaction conditions will be carried out to result in a structure-function correlation. *In situ* DR-UV-VIS spectra of ball-milled MoO_3 and its corresponding oxide nitride are shown as examples in **Figure 5-5**. These spectra were recorded during first treatment under reaction conditions up to 700 K followed by an isotherm phase at 700 K. Both set of spectra showed significant changes in the low energy range as well as a red shift in adsorption edge and the maximum of spectra. The evolution of spectra of MoO_3-type oxide nitrides differed strongly from the evolution of spectra of the oxides in the temperature range from 530 K to 700 K. The positions and intensities of both set of spectra did not change significantly during isothermal reaction at 700 K.

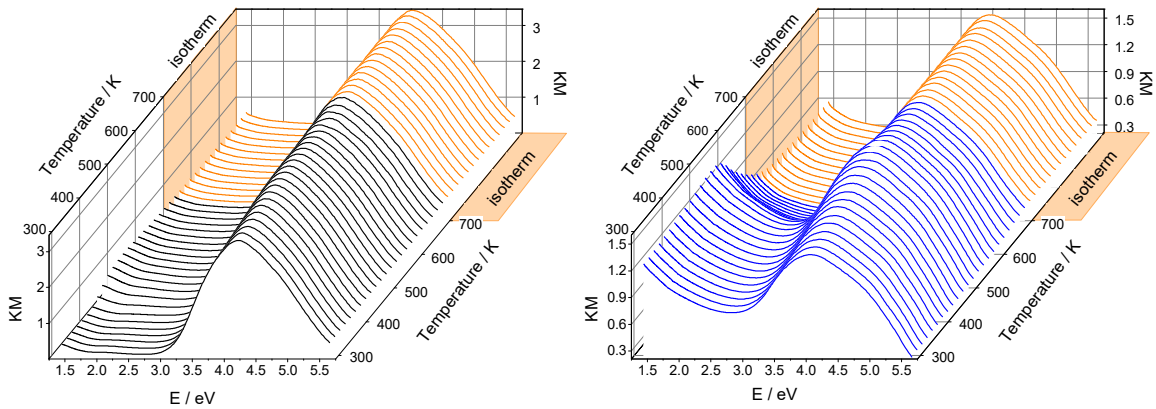

Figure 5-5: *Evolution of in situ DR-UV-VIS spectra of ball-milled MoO_3 (left) and its corresponding oxide nitride (right) during treatment in 5% propene, 5% oxygen in helium from 298 K to 700 K followed by isothermal treatment at 700 K.*

A more detailed analysis of the low energy range in the spectra of all samples is given in **Figure 5-6**. The figure shows the evolution of *KM* values at 1.5 eV. During first treatment under reaction conditions, the absorption of all ball-milled oxides slightly decreased up to 380 K while the absorption of non-milled MoO_3 remained constant. Afterwards, the absorption increased until reaching a maximum at 507 K followed by a slight decrease to the same absorption as before. This increase was correlated to the removal of water indicated by ion current *m/e* 18. The intensity of the peak of ion current

m/e 18 as well as increase of absorption was increased with increasing milling-time. During isothermal treatment the absorption at 1.5 eV of all oxides only slightly decreased.

In contrast, the absorption of non-milled oxide nitride *MON* only decreased in a temperature range of 570 – 700 K. The evolution of spectra of all MoO_3-type oxide nitrides revealed an increasing absorption followed by a strongly decrease up to the end of isothermal treatment. The decrease started at almost 570 K and was associated with the removal of nitrogen. The nitrogen removal was followed up by ion current *m/e* 17 (NH_3). Hence, it corroborated that nitrogen was incorporated mainly as NH_x species as discussed above and for non-milled ammonolyzed MoO_3 [49]. The decrease of absorption ended at a similar level for all oxides. The temperature of maximum absorption shifted to lower temperature with longer milling time from 570 K to 546 K. During the second treatment under reaction conditions only minor changes in absorption at low energies of all spectra were identified.

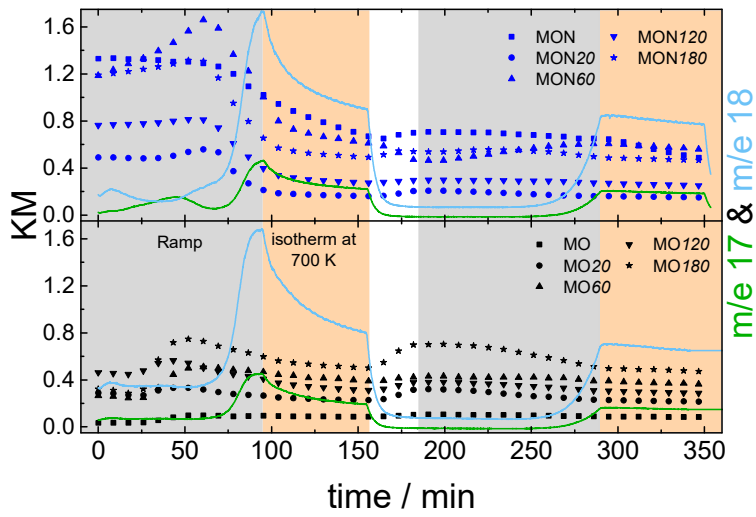

Figure 5-6: *Evolution of absorption intensity at E = 1.5 eV of different ball-milled MoO_3 (bottom) and its corresponding oxide nitrides (top) during two successive treatment in 5% propene, 5% oxygen in helium from 298 K to 700 K followed by isothermal treatment at 700 K. Normalized ion currents m/e 17 (NH_3, green line) and m/e 18 (H_2O, blue line) indicated nitrogen and water removal.*

The spectra of all oxides and oxide nitrides showed a shift in absorption edge during treatment under reaction conditions and it was shown above that ammonolysis of MoO_3 led to changes in the position of the adsorption edge (see **chap. 3.5**). Hence, the edge position was determined for all in situ spectra as described by Weber (**Figure 5-7**) [110]. The evolution of absorption edge energies of the oxides showed a temperature dependent decrease in optical band gap which might be caused by the formation of oxygen vacancies [142].

The corresponding oxide nitrides showed the same temperature dependent behavior until 550 K. In contrast to the oxides the optical band gap of oxide nitrides increased at higher temperatures during first treatment under reaction conditions due to the removal of nitrogen. Analysis of optical band gap during second treatment under reaction conditions revealed a similar evolution for oxides and oxide nitrides. Furthermore, the optical band gaps were only slightly decreased compared to oxides and the increasing effect of milling time was still detectable.

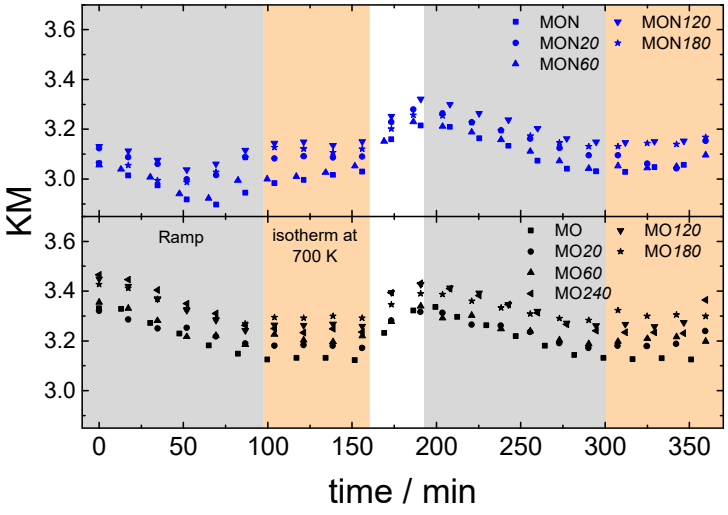

Figure 5-7: *Evolution of optical band gap of different ball-milled MoO_3 (bottom) and its corresponding oxide nitrides (top) during double treatment in 5% propene, 5% oxygen in helium from 298 K to 700 K followed by isothermal treatment at 700 K. Normalized ion current m/e 17 (NH_3, green line) indicated nitrogen removal.*

A comparison of all DR-UV-VIS spectra measured at room temperature before each treatment under reaction conditions and after second treatment is shown in **Figure 5-8**. Here, structural changes were separated from temperature dependent effects. Only little differences caused by treatment under reaction conditions were observed in the high energy range above 4 eV. Conversely, the absorption of molybdenum oxide nitride decreased strongly below 3 eV during the first treatment under reaction conditions. After the first treatment the spectra of MoO_3-type oxide nitride was similar to the spectra of MoO_3. Additionally, this comparison pointed out the blue shift of optical band during the first treatment. It corroborated that both materials did not show any changes in electronic structure when treatment under reaction conditions was repeated. Subsequently, the electronic structure of investigated molybdenum oxide nitrides was irreversible changed by nitrogen removal.

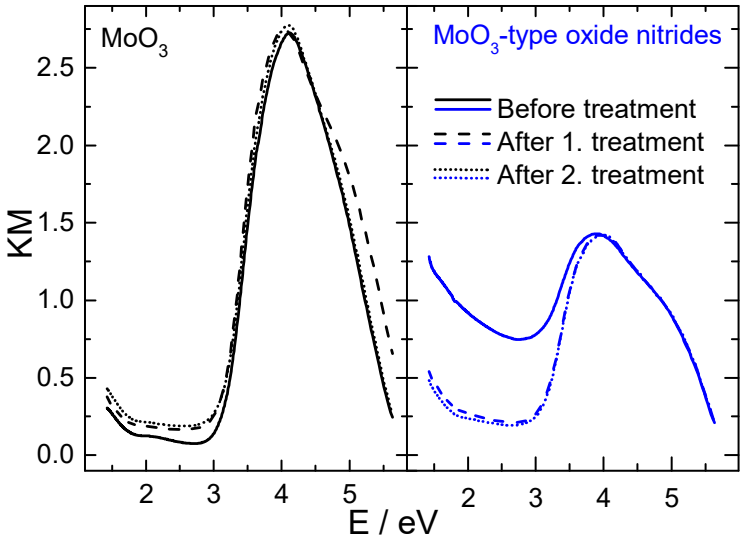

Figure 5-8: *DR-UV-VIS spectra of ball-milled MoO_3 (left) and its corresponding oxide nitride (right) recorded at room temperature before each treatment and last treatment under reaction conditions.*

5.5 Mechanistic discussion of nitrogen removal

Analysis of *in situ* DR-UV-VIS spectra resulted in a dependence of stability of oxide nitrides on milling time. Size analysis of ball-milled MoO_3 revealed that milling time of MoO_3 mainly influenced crystallite size while lattice strain was not changed. Crystallite

sizes calculated from different *hkl* diffraction peaks of orthorhombic MoO_3 were differently affected by milling process. Crystallite sizes are shown as a function of on-set temperature of nitrogen removal in **Figure 5-9**. A correlation between crystallite size calculated from (0k0) diffraction peaks and stability of oxide nitrides can be seen. The stability of oxide nitrides increased with increasing crystallite sizes. Even though crystallite sizes for (200) and (002) directions were also affected by the milling process a similar correlation with stability was not found. Crystal structure of MoO_3 consists of MoO_6 octahedral forming layers which are parallel to (020) plane. Sizes of these layers influenced stability of oxide nitrides. Oxygen ions next to interlayer space were mainly substituted by nitrogen ions (**chap. 3.4**). **Figure 5-10** shows a schematic presentation of nitrogen removal of oxide nitrides with MoO_3 structure. Nitrogen ions had to diffuse through the gap between the layers. Hydrogen atoms were incorporated forming OH and (NH_x) groups. This insertion led to an additional obstruction. In addition, increasing crystallite size parallel to (020) plane resulted in a longer diffusion path. Hence, the obstruction for diffusion was also more obstructed.

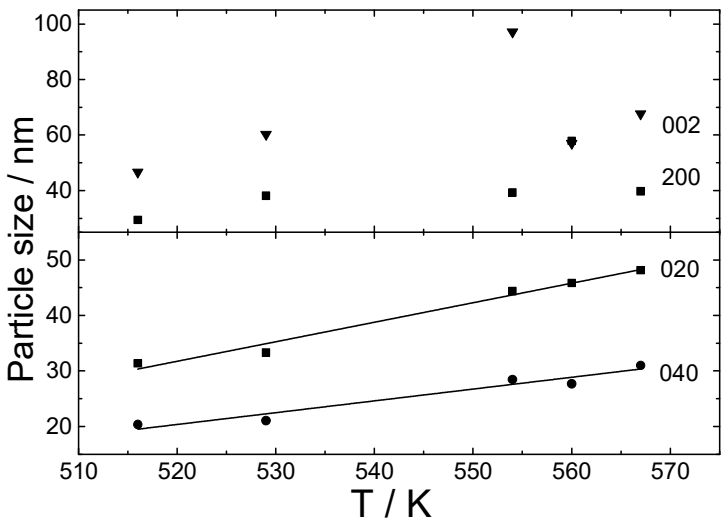

Figure 5-9: *Particle size calculated from different diffraction peaks as a function of stability temperature of ball milled oxide nitrides*

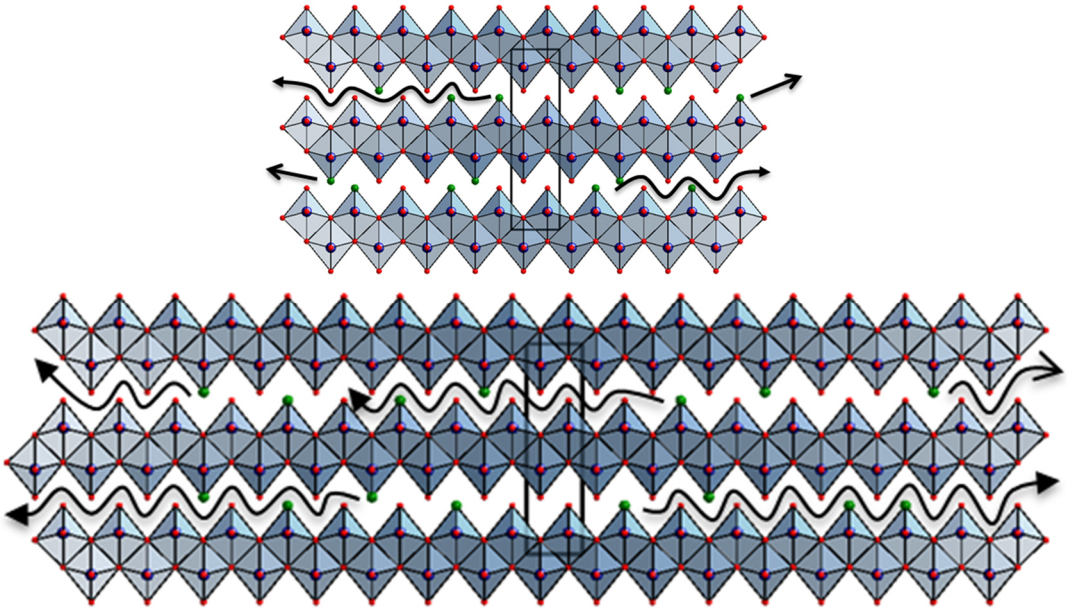

Figure 5-10: *Structure of MoO_3-type oxide nitrides is shown for small (top right) and big (bottom) crystallite size calculated from (0k0) diffraction peaks.*

5.6 Conclusion

The catalytic performance of MoO_3 samples with varying crystallinity and MoO_3-type oxide nitrides was studied under selective propene oxidizing conditions. The catalysts were investigated by *in situ* DR-UV-Vis spectroscopy. Modification of crystallinity resulted in an increased catalytic activity. Reaction rates for propene conversion showed a deactivation of the catalyst during isothermal treatment under reaction conditions. Otherwise, the formation rate of acrolein was increased by ball-milling without deactivation during isothermal treatment. The quantitative analysis of selective propene oxidation products revealed a significant influence of incorporation of nitrogen on the formation of acrolein and CO_X. The increased selectivity towards acrolein might be due an enhanced achievable of nucleophilic lattice oxygen. Investigations on the thermal stability of MoO_3-type oxide nitrides revealed that nitrogen ions were removed from the catalysts during heating to reaction temperature. *In situ* spectroscopic investigations corroborated the removal of nitrogen associated with replenishing the defects. The defects might be re-oxidized by gas-phase oxygen over a wide temperature range. A correlation between crystallite size from the (020) and (040) diffraction peaks and the thermal stability of MoO_3-type oxide nitrides was found. The ammonolysis of larger crystallites resulted in more stable oxide nitrides. This correlation might be due to layer structure of MoO_3. The oxygen ions for re-oxidation of defects must cover a longer distance in the crystallite.

In summary, increasing the catalytic activity by ball-milling led to a precursor for less stable MoO_3-type oxide nitrides. Nevertheless, the differences in catalytic performance supported the thesis that modification of anion lattice can result in suitable model systems for correlations between oxygen mobility and catalytic performance. However, MoO_3 is not the most relevant system for studies on selective oxidation of propene. Consequently, the range of oxide nitrides should be extended to more relevant structures in propene oxidation. Model catalysts with the Mo_5O_{14}-structure constitute more complex system compared to MoO_3 (**Figure 5-11**). The structural motives of Mo_5O_{14} were found to be more relevant for selective oxidation of propene [143]. Additionally, the Mo_5O_{14}-structure represents a non-layer structure. The ammonolysis of model catalysts

with Mo_5O_{14}-structure might result in more stable oxide nitrides. The previous results of investigations on molybdenum oxide nitrides will be applied to the ammonolysis of $(MoV)_5O_{14}$ in the next chapter of this work.

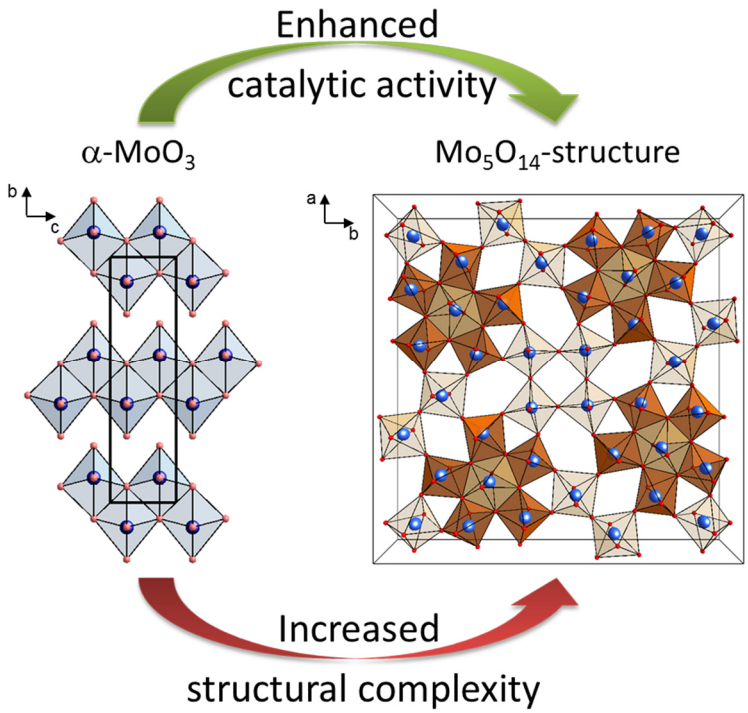

Figure 5-11: *Extension of range of molybdenum-based oxides for modification of its anion lattice by incorporation of nitrogen ions.*

6 Preparation and characterization of mixed molybdenum oxide nitrides

6.1 Introduction

Previous results showed that modification of anion lattice by ammonolysis might be a useful method to influence oxygen mobility of molybdenum oxides. Hence, oxide nitrides represent suitable model system for studying correlations between oxygen mobility and catalytic performance [48]. Although ball milling of MoO_3 resulted in an increased catalytic activity for selective oxidation of propene, MoO_3-type oxide nitrides showed low thermal stability for investigations on catalytic performance. The low thermal stability of MoO_3-type oxide nitrides was due to crystal structure of MoO_3. MoO_3 is built-up by layers of MoO_6 octahedrons which enabled easy incorporation as well as removal of nitrogen. Model catalysts with the Mo_5O_{14} structure stabilized by additional V centers constitute more complex systems compared to MoO_3 without layer structure. Hence, ammonolysis of $(MoV)_5O_{14}$ might result in more stable oxide nitrides. The Mo_5O_{14} structure constitutes a more relevant system for selective oxidation of propene. Furthermore, the known defect structure of $(MoV)_5O_{14}$ can lead to an enhanced catalytic activity compared to MoO_3 [143,144]. This chapter describes the preparation of Mo_5O_{14}-type oxide nitrides. The characterization focuses on the incorporation of nitrogen in the anion lattice and the resulting structural effects. Additionally, the compensation of additional negative charges of nitrogen ions will be investigated to complete structural characterization. The last part of this chapter focuses on electrical properties of $(MoV)_5O_{14}$ and its corresponding oxide nitrides.

6.2 Experimental

6.2.1 Preparation of $(MoV)_5O_{14}$ and Mo_5O_{14}-type oxide nitrides

$(MoV)_5O_{14}$ was prepared according to the literature using ammonium heptamolybdate (AHM) and vanadyl oxalate [20]. An aqueous solution of vanadyl oxalate was obtained by adding 180 mg oxalic acid to a suspension of 109.2 mg V_2O_5 in 50 mL bidestilled water at 353 K. The resulting blue solution was mixed with a solution of 3 g AHM in 20 mL bidestilled water. After stirring the solution for 1 h at 353 K the olive-green precursor was crystallized at 338 K. The MoV oxide precursor was treated in helium at 773 K for 4 h followed by dissolution of impurities in 1 M ammonia solution. Finally, $(MoV)_5O_{14}$ model catalysts were obtained by an additional treatment in helium at 773 K for 4 hours. The metal content in the $(Mo,V)_5O_{14}$ phase was 93 mol-% Mo and 7 mol-% V.

Corresponding oxide nitrides of $(MoV)_5O_{14}$ were produced by ammonolysis of $(MoV)_5O_{14}$ using a tube furnace with a silica tube and direct gas supply [85]. Preparation conditions (temperature and ammonia flow rate) were varied to preserve the Mo_5O_{14} structure and optimize the incorporation of nitrogen. Gas flows were adjusted by mass flow controllers (Bronkhorst). Ammonolysis was carried out in a temperature range from 498 K – 573 K and the ammonia gas flow was varied between 5 and 20 l/h. Reaction time was kept constant at 10 h.

6.2.2 Sample characterization

X-ray diffraction (XRD)

X-ray diffraction patterns were recorded on an X'Pert PRO MPD diffractometer (Panalytical) in θ-θ geometry using Cu K_α radiation and a solid-state multi-channel PIXcel® detector. Measurements were performed in reflection mode in a range of 5 – 80° 2θ in steps of 0.013° 2θ with a sampling time of 60 s/step using a silicon sample holder. Analysis of the diffractograms and rietveld refinements of the diffractograms were carried out using the programs X'Pert High Score Plus (v2.2d, PANalytical) and FullPROF suite program 1.10 [86,87].

X-Ray Fluorescence Analysis

Elemental analysis by X-ray fluorescence spectroscopy was performed on an X-ray spectrometer (AXIOS, 2.4 kW model, PANalytical) equipped with a Rh K_α source, a gas flow detector and a scintillation detector. 100 mg of the sample were diluted with wax (Hoechst wax C micropowder, Merck) at a ratio of 1:1 and pressed into 13 mm pellets. Quantification was performed after calibration with mixtures of MoO_3 and V_2O_5 as external standards with the SuperQ 5 software package (PANalytical).

Elemental Analysis

Elemental contents of C, H and N were determined by using a FlashEA 1112 NC analyzer (ThermoFinnigan/ThermoElectron) with CHNS-O configuration. Measurements were carried out to determine nitrogen contents after ammonolysis of $(Mo,V)_5O_{14}$.

Fourier-transformed infrared spectroscopy (FTIR)

A Magna System 750 (Nicolet) was used to measure infrared spectra of the samples in a wavenumber range of 400 – 4000 cm^{-1}. Samples were diluted with CsI (1:300) and pressed into pellets of 13 mm in diameter.

Impedance spectroscopy

Impedance spectra of mixed molybdenum oxides and oxide nitrides were obtained by measuring the magnitude $|Z|$ and the phase ϕ of an alternating current as a response of an applied alternating potential (impedance analyzer N4L: IAI+PSM1735). The real part Z' and the imaginary part Z'' of the impedance were calculated from these results. The impedance was measured as a function of frequency (1 Hz - 10 MHz) and temperature. Oxides and oxide nitride samples were pressed into pellets with a diameter of 5 mm (initial weight 50 mg, 750 MPa pressure) and placed between two Au disc electrodes. Impedance measurements were carried out in a temperature range up to 673 K with flowing gas mixtures. Gas mixtures of oxygen and nitrogen were adjusted by mass flow controllers (Bronkhorst) with a total flow of 85 ml/min.

X-Ray Absorption spectroscopy (XAS)

Transmission X-ray absorption spectroscopy (XAS) was performed at the V K edge (5.465 keV) and the Mo K edge (19.999 keV) at beamline C, and X1, respectively, at the Hamburg Synchrotron Radiation Laboratory, HASYLAB, using a Si(111) (V K edge) or Si(311) (Mo K edge) double crystal monochromator. For ex situ measurements samples were diluted with wax (Hoechst wax C micropowder, Merck) and pressed into self-supporting pellets with a diameter of 13 mm. Sample masses were calculated to result in an edge jump around $\Delta\mu(d)$ = 1.5 at Mo K edge and $\Delta\mu(d)$ = 0.3 at V K edge. X-ray absorption fine structures (XAFS) at the V K edge (5.4–6.0 keV) were measured in approximately 21 min. At the Mo K edge the energy range for a XAFS scan was 19.9-21.0 keV (~12 min).

Data analysis was performed by using the software package WinXAS v3.2 [88]. Background subtraction and normalization was carried out by fitting a linear polynomial to the pre-edge region and a third degree polynomial to the post-edge region, respectively. The X-ray absorption fine structure (EXAFS) $\chi(k)$ of Mo K edge XAFS spectra was extracted by using cubic splines to obtain a smooth atomic background, $\mu_0(k)$ in the k range from 3 to 14 $Å^{-1}$. The radial distribution function $FT(\chi(k)\cdot k^3)$ was calculated by Fourier transformation of the k^3-weighted experimental $\chi(k)$ function, multiplied by a Bessel window, into the R space. XAS structure model and refinement strategy are described in **chap. 6.4**.

Temperature-programmed oxidation (TPO)

Temperature-programmed oxidation (TPO) experiments were carried out with a catalyst analyzer from BEL Japan Inc. equipped with a silica glass tube reactor. 30 mg of Samples were placed on silica wool inside the reactor next to a thermocouple. A gas flow (20% oxygen in helium) of 40 ml/min was adjusted during reaction. Heating rates used were 5, 10, 15 K/min to 773 K while outlet gas composition was measured with a non-calibrated mass spectrometer (Omnistar, Pfeiffer).

6.3 Optimization of ammonolysis parameters

In a first step the parameters of ammonolysis had to be optimized to prepare mixed molybdenum oxide nitrides with Mo_5O_{14} structure. For this purpose, ammonolysis temperature and ammonia flow rate were varied while reaction time was kept constant. **Figure 6-1** shows the XRD powder patterns of ammonolysis products treated at a temperature range of 498 K – 573 K and 5 l/h NH_3. The diffraction patterns of the samples ammonolyzed at 498 K and 523 K showed the same phase composition as the starting material $(Mo,V)_5O_{14}$. Elemental analysis provided information about the nitrogen content in the prepared samples. The nitrogen content could be increased by increasing the temperature. At 533 K and 548 K $(Mo,V)_5O_{14}$ was partially reduced to Mo_9O_{25} by H_2 formed during decomposition of gaseous NH_3[145]. Mo_3N_2 was formed at 573 K [146]. Additionally, the effect of variation of ammonia gas flow was investigated. The incorporated nitrogen content could also be adjusted by modifying the ammonia gas flow. In contrast to temperature modification, the variation of ammonia gas flow did not influence the phase composition after ammonolysis. All results of optimization are summarized in **Table 6-1**. Consequently, a set of oxide nitrides with 1 wt%, 1.3 wt% and 1.5 wt% nitrogen contents was prepared by varying ammonolysis temperature and ammonia gas flow. The Mo_5O_{14}-type oxide nitrides with 1 wt% or 1.3 wt% nitrogen were prepared at 498 K with 5 l/h or 10 l/h ammonia. Temperature was increased to 523 K for preparing oxide nitride with 1.5 wt% nitrogen adjusting an ammonia gas flow of 5 l/h. A surface area A_{BET} of approximately 4 g/m^2 was determined for all samples by N_2 physisorption. XRF analysis showed that metal contents were not affected by ammonolysis.

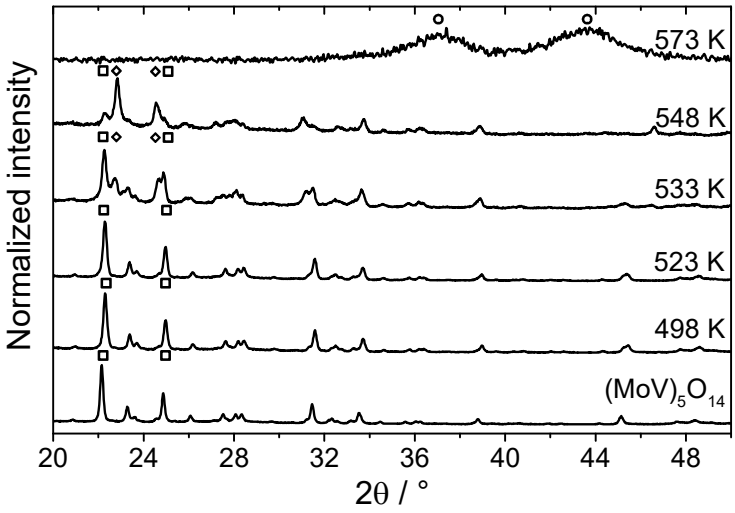

Figure 6-1: *X-Ray powder patterns of ammonolysis products of $(MoV)_5O_{14}$ ammonolyzed at different temperatures with 10 h reaction time and a constant flow of 5 l/h NH_3. The identified phases are marked by symbols (□ Mo_5O_{14}, ◊ Mo_9O_{26}, ○ Mo_3N_2) (ICSD 27202)* [145,146].

Table 6-1: *Nitrogen contents and phase composition of ammonolysis products of $(MoV)_5O_{14}$ while temperature and ammonia flow rate were varied. The reaction time was kept constant at 10 h.*

T / K	$\dot{V}_{NH_3}$ / l·h^{-1}	wt% N	Phase composition
498	5	1.1	$(Mo,V)_5O_{14}$
523	5	1.6	$(Mo,V)_5O_{14}$
533	5	3.6	$(Mo,V)_5O_{14}$ Mo_9O_{26}
548	5	7.1	$(Mo,V)_5O_{14}$ Mo_9O_{26}
573	5	---	Mo_3N_2
523	5	1.6	$(Mo,V)_5O_{14}$
523	10	2.2	$(Mo,V)_5O_{14}$
523	20	2.7	$(Mo,V)_5O_{14}$

6.4 Structural characterization

6.4.1 Analysis of long-range structure (XRD)

A Rietveld refinement of the Mo_5O_{14} crystal structure to XRD powder patterns of $(MoV)_5O_{14}$ and its corresponding oxide nitrides with 1 wt%, 1.3 wt% and 1.5 wt% nitrogen was carried out. A pseudo-Voigt function convoluted with an axial divergence asymmetry function was used for Rietveld refinement [92,147]. The correction by an axial divergence asymmetry function was necessary to account for peak asymmetry at low diffraction angels due to instrumental effects [148]. The good agreement of the experimental and theoretical data showed that other crystalline phases were not detected (**Figure 6-2**). The formation of significant amounts of amorphous phases during ammonolysis was excluded by analyzing the XRD powder pattern of a mixture of 50 wt% of the sample and 50 wt% of α-Al_2O_3 as described in the literature [149].

The results of Rietveld refinements of all samples are summarized in **Table 6-2**. In conjunction with ammonolysis and increasing nitrogen content of the samples a slight increase of the *a/b* parameter of the tetragonal crystal system was observed. No significant change in *c* parameter was determined. Consequently, cell volume was increased after ammonolysis. The increase of cell parameters might be explained by incorporation of nitrogen in the anion lattice of $(Mo,V)_5O_{14}$. Logvinovich et. al. reported a similar behavior of strontium-molybdenum oxide nitrides due to the larger effective ionic radius of N^{3-} (1.32 Å) compared to O^{2-} (1.26 Å) [94]. Additionally, an increasing cell volume of about 1 % was also found for different iron based materials when oxygen ions was substituted by nitrogen ions [46,150].

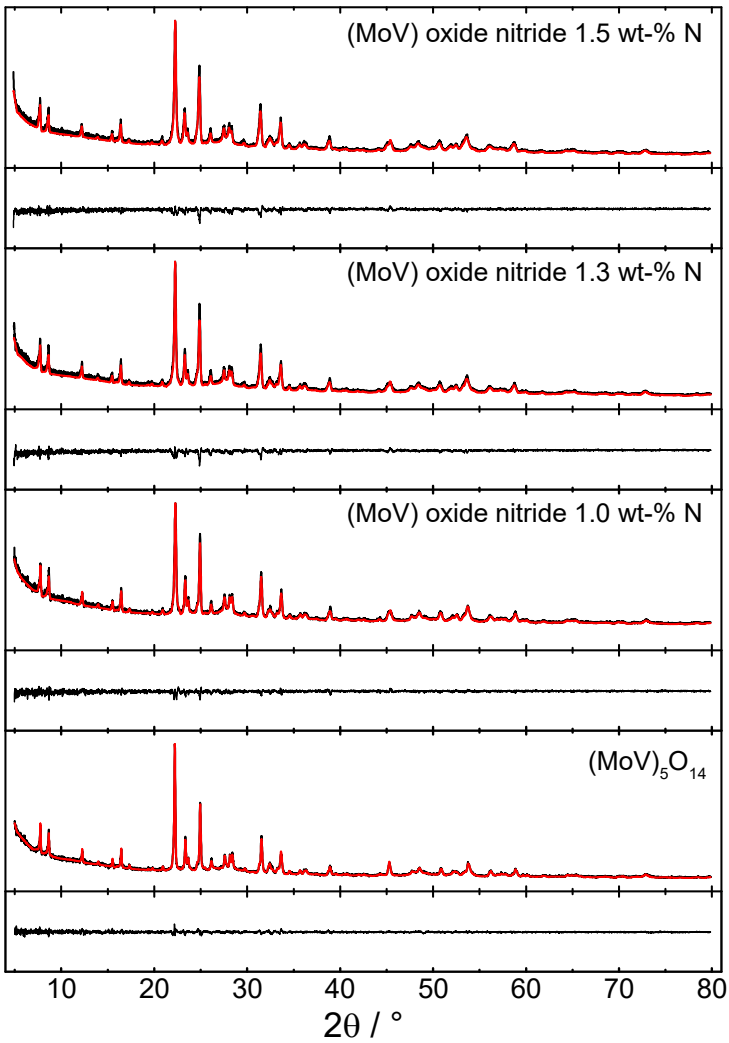

Figure 6-2: *Rietveld refinements of $(MoV)_5O_{14}$ crystal structure to XRD powder patterns of $(MoV)_5O_{14}$ and its corresponding oxides nitrides with different nitrogen contents. Difference curves are shown under each refinement. Selected resulting parameters of refinements are given in* ***Table 6-2****.*

Table 6-2: *Results of Rietveld refinements and Williamson-Hall analysis of $(MoV)_5O_{14}$ and its corresponding oxide nitrides with different nitrogen contents.*

	Oxide	Oxide nitride 1 wt.-% N	Oxide nitride 1.3 wt.-% N	Oxide nitride 1.5 wt.-% N
a / Å	22.8666(4)	22.8969(8)	22.9302(8)	22.9491(8)
c / Å	4.0027(9)	3.9939(2)	3.9950(2)	3.9936(2)
V / Å³	2092.9	2093.2	2100.6	2103.3
ε	0.061	0.095	0.148	0.171
D / nm	(57 ± 2)	(56 ± 2)	(54 ± 2)	(57 ± 2)
GOF	1.3	1.3	1.5	1.9
Chi²	1.8	1.6	2.1	1.4
FWHM (001) / °2θ	0.121	0.173	0.175	0.193

A line broadening of the X-ray diffraction peaks after ammonolysis was observed. The FWHM of the most intensive line at 2θ=22.4 °2θ was 0.121 °2θ. After ammonolysis a FWHM of 0.193 °2θ was determined for the sample with the highest nitrogen content (see **Table 6-2**). The line broadening can be due to a decrease in particle size or increase in lattice strain. For a detailed analysis of the line broadening a size-strain analysis via the Williamson-Hall (WH) method was carried out [151]. The Williamson-Hall analysis assumes that total line broadening is represented by the sum of the contributions of particle size and lattice strain. Particle size D and the lattice strain ε can be determined by plotting $(\beta_{hkl} \cdot \cos\theta)/\lambda$ versus $\sin\theta$ according to the Williamson-Hall equation

$$\frac{\beta_{hkl}}{\lambda}\cos\theta = \frac{k}{D} + \frac{4\varepsilon}{\lambda}\sin\theta \text{ [152]}. \tag{6-1}$$

Integral breadth of LaB_6 660a was used as XRD standard to correct the measured integral breadth for instrumental effects on line broadening. The corrected integral breadth β_{hkl} was estimated by the expression

$$\beta_{hkl} = ((\beta_{hkl})^2_{measured} - (\beta)^2_{instrumental})^{1/2} \tag{6-2}$$

which was used for WH analysis [153]. A isotropic distribution of particle size and lattice strain in the samples constitutes a required assumption for determining particle size and lattice strain. A linear evolution of the WH plot indicates an isotropic distribution. XRD powder patterns of all samples with Mo_5O_{14}-structure showed many overlapping

diffraction peaks. Hence, a simultaneous analysis of all diffraction peaks was required to perform a significant size-strain analysis of selected reflections with varying *hkl* [96]. Subsequently, the results of Rietveld refinement were used for WH analysis. According to the refinement procedure the FWHM of each diffraction peak was calculated from halfwidth parameters U, *V* and *W*. Afterwards, the FWHM was transferred into integral breadth according to the literature [100]. However, this procedure might not lead to information about isotropic distribution of particle size and lattice stain due to calculation procedure of FWHM. Therefore, an additional control of isotropic distribution was carried out by single line fitting of few selected reflections with varying *hkl*.

The Williamson-Hall-plots for all samples resulted in a straight line over a wide angle range (**Figure 6-3**). Thus, particle size was calculated from intercept with the y-axis of the straight line while the lattice strain was obtained from the slope. The intercept with the y-axis revealed in average particle size of about 56 nm for all samples. Conversely, the slope had significantly changed from 0.061 to 0.171 after ammonolysis of $(Mo,V)_5O_{14}$. The degree of increase of lattice strain strongly depends on the amount of substitution of oxygen atoms by nitrogen atoms. Besides the increase of volume of elementary cell the increase of lattice strain confirmed the incorporation of nitrogen atoms in Mo_5O_{14}-structure.

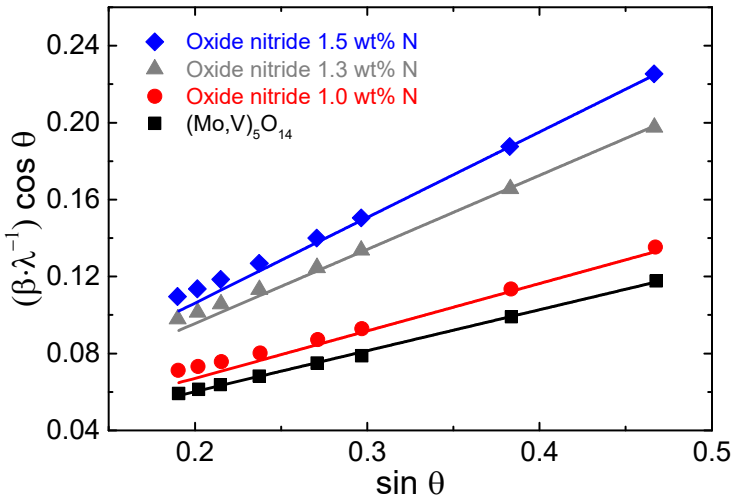

Figure 6-3: *Size and strain analysis of $(MoV)_5O_{14}$ and its corresponding oxide nitrides with different nitrogen contents samples by Williamson-Hall method. The selected diffraction peaks were chosen from all crystallographic directions. Results of size and strain are shown in* ***Table 6-2****.*

6.4.2 Analysis of short-range structure (XAFS)

X-ray absorption spectroscopy was carried out to analyze the influence of nitrogen incorporation on the short-range structure of the MoV oxide nitrides with 1 wt% and 1.5 wt% N. The Mo_5O_{14} structure consists of six different metal sites and 16 oxygen sites in one unit cell (**Figure 6-4**). Additionally, all metal sites are doubled due to mirror plane in the *ab*-plane and half occupied. The metal sites are coordinated by oxygen atoms in pentagonal bipyramidal geometry or disordered octahedron. A XAS measurement results in an average spectrum of all metal sites. Hence, analysis of EXAFS data of Mo_5O_{14} structure with its numerous metal sites cannot be carried out by refining a structure model of all metal sites. Although the $\chi(k)$ of all metal sites can be simulated, a refinement of all simulations to one spectrum would not succeed. A larger number of free parameters would be required than experimentally obtained. Thus, the refinement strategy was adapted to simulate an averaged spectrum of the Mo_5O_{14} structure. Averaging distances can be used for analyzing complex structures such as $(Mo,V)_5O_{14}$ [30,154]. Vanadium was only to a small extent incorporated to stabilize the molybdenum based structure. Subsequently, the distinction of molybdenum and vanadium was omitted in the structure model. The metal-oxygen and metal-metal distances based on the XRD Rietveld refinements were averaged into three types of distances. The average coordination number of each scattering path was calculated from the classification of distances in respect to Mo_5O_{14} structure. This structure model was refined to experimental data in two steps. One overall E_0 shift and respective Debye-Waller-factors for all distances were refined in the first step with average distances kept invariant. Afterwards, free-ranged average distances were added to the refinement procedure. Coordination numbers were kept invariant.

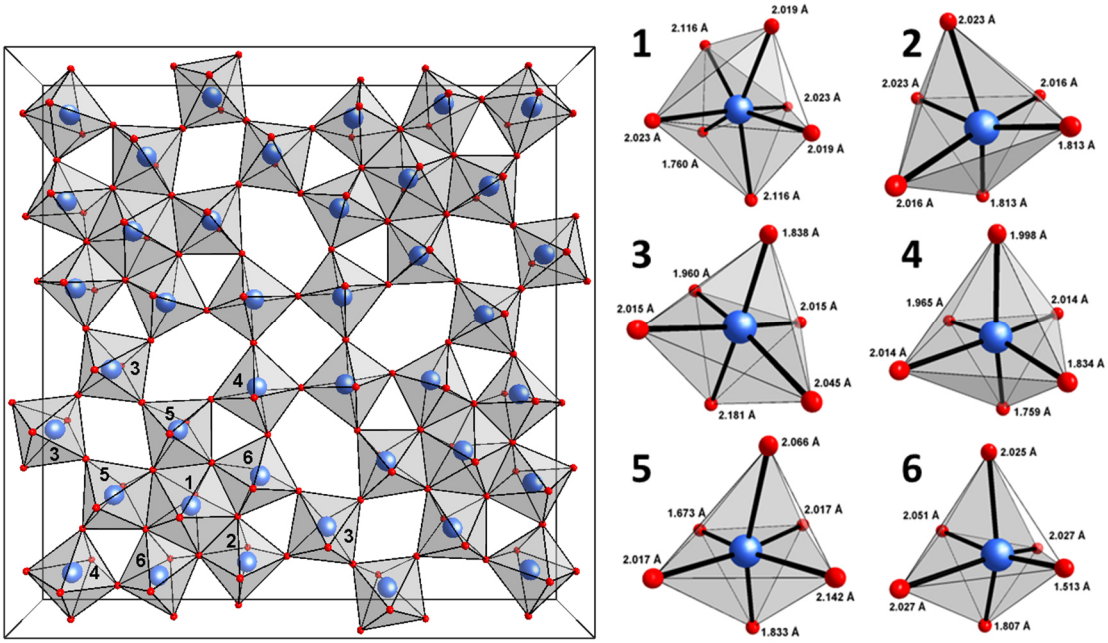

Figure 6-4: *Left: View on the ab-plane of Mo_5O_{14} structure with numbered metal sites of structural motif. Right: Coordination spheres of all metal sites of Mo_5O_{14} structure. Mo-O distances were calculated from refined XRD atom positions. The values were applied to model of averaging distances for XAFS refinement.*

The pseudo radial distribution function, $FT(\chi(k)\cdot k^3)$, of all samples showed a similar shape. Two prominent peaks could be identified at 1-2 Å assigned to Mo-O distances. Furthermore, two peaks were observed in the range of 3-4 Å. These peaks were assigned to Mo-Mo distances. The XAFS spectra of $(Mo,V)_5O_{14}$ and its corresponding oxide nitrides could be well described with three Mo-O and three Mo-Mo distances. A good agreement between experimental $FT(\chi(k)\cdot k^3)$ of $(MoV)_5O_{14}$ and its corresponding oxide nitrides with 1 and 1.5 wt-% and theoretical $FT(\chi(k)\cdot k^3)$ of model of average distances was achieved (**Figure 6-5**). Results of all refinements are shown in **Table 6-3**. Significance of the fitted parameters was determined by calculating confidence limits and statistical F parameters.

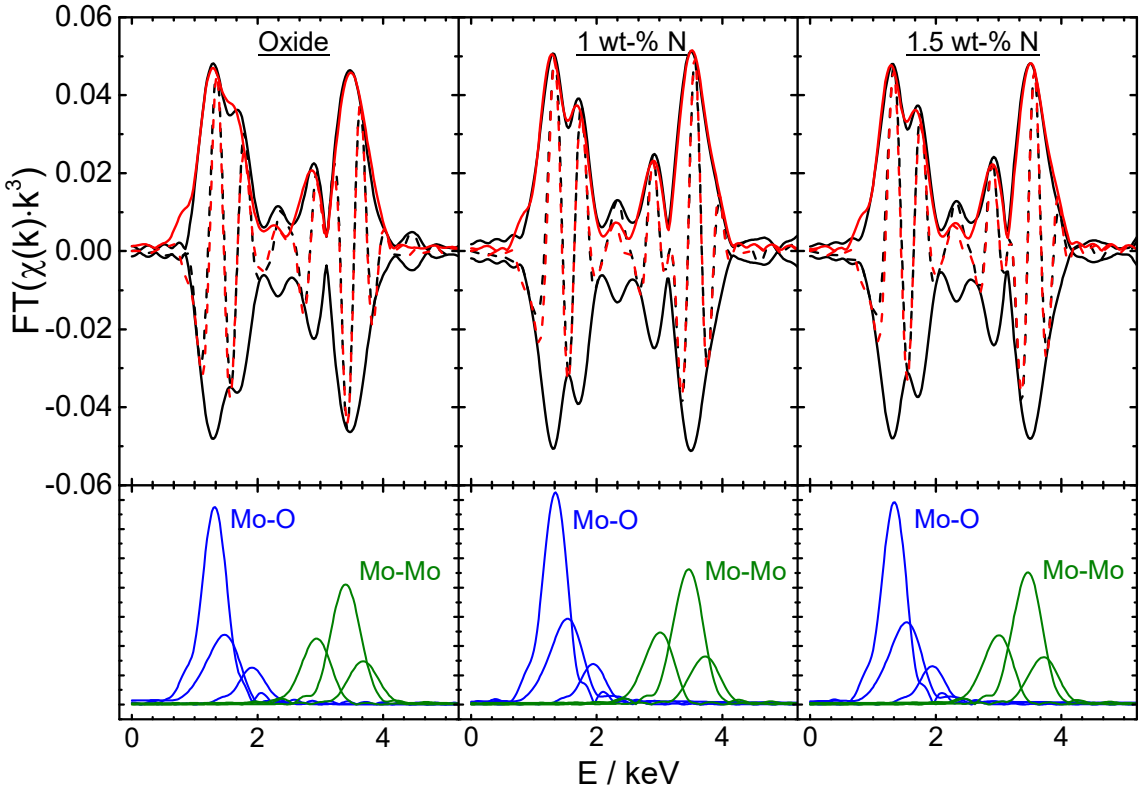

Figure 6-5: *Top: Refinements of experimental FT(χ(k)·k³) to theoretical model of averaged distances of $(MoV)_5O_{14}$ and two oxide nitrides with different nitrogen contents. Bottom: Mo-O (blue) and Mo-Mo (green) scattering paths of refined FT(χ(k)·k³). The results of refinements are shown in* **Table 6-3**.

The disorder parameter, σ^2, of the shortest Mo-O distance increased with increasing nitrogen content of the sample while σ^2 of the middle Mo-O distance was not influenced by ammonolysis (**Figure 6-6**). Formation of oxygen vacancies or incorporated ions might cause structural disorder. Additionally, the shorter Mo-O scattering path was found to be the most intensive in all samples which might explain the influence on σ^2 of the shorter Mo-O scattering path. The disorder parameters of the shortest and longest Mo-O distances had to be correlated to result in a statistically stable refinement. The necessity of the correlation of these parameters might be explained by considering Mo_5O_{14} structure. Most of the long Mo-O distances subtend the short Mo-O distances in octahedral coordination. Hence, the disorder parameter of the short Mo-O distance influenced the disorder parameter of the longer Mo-O distance. All Mo-O distances in *c* direction in Mo_5O_{14} structure were classified as “axial” Mo-O distances (**Figure 6-7**). Thus,

it might be suggested that oxygen ions of the *ab* plane were primarily substituted by nitrogen ions. On this basis of the increase of the volume of the tetragonal elementary cell in *a*/*b* direction were plausible. Apparently, the Mo-Mo scattering paths were not significantly influenced by ammonolysis. Thus, it can be assumed that ammonolysis of $(MoV)_5O_{14}$ only led to changes in the anion lattice while the cation lattice was not significantly affected. XRD represents a complementary method to XAS by providing information about long-range structure. Combining these two methods, a detailed characterization of the structural influences of ammonolysis of $(MoV)_5O_{14}$ could be carried out. The increasing lattice strain obtained by XRD corroborated the increasing structural disorder in the local structure of the anion lattice.

Table 6-3: *Type, number (N), and XAFS disorder parameter (σ^2) of atoms at a distance R from the Mo atoms in $(MoV)_5O_{14}$ and oxide nitrides with different nitrogen contents. Experimental distances and disorder parameters were obtained from refinement of a model of averaged distances based on XRD results (k range from 3 to 14 Å^{-1}, R range from 0.9 to 3.96 Å, N_{ind} =23 , N_{free} = 5 - 11)*

Type	Oxide			Oxide nitride 1 wt.-% N			Oxide nitride 1.5 wt.-% N		
	N	R / Å	σ^2 / Å^2	N	R / Å	σ^2 / Å^2	N	R / Å	σ^2 / Å^2
Mo-O "short"	1.6_f	1.74	0.0012_c	1.6_f	1.74	0.0013_c	1.6_f	1.74	0.0016_c
Mo-O "axial"	3.8_f	2.00	0.014	3.8_f	2.00	0.014	3.8_f	2.00	0.014
Mo-O "long"	0.7_f	2.36	0.0012_c	0.7_f	2.36	0.0013_c	0.7_f	2.37	0.0016_c
Mo-Mo "short"	1.3_f	3.33	0.0058	1.3_f	3.33	0.0055	1.3_f	3.33	0.0057
Mo-Mo "axial"	2.3_f	3.8	0.0036_c	2.3_f	3.80	0.0033_c	2.3_f	3.81	0.0034_c
Mo-Mo "long"	1_f	4.09	0.0036_c	1_f	4.06	0.0033_c	1_f	4.06	0.0034_c
Residual	10.5			8.5			9.2		
E_0 / eV	-1.78			9.08			7.88		

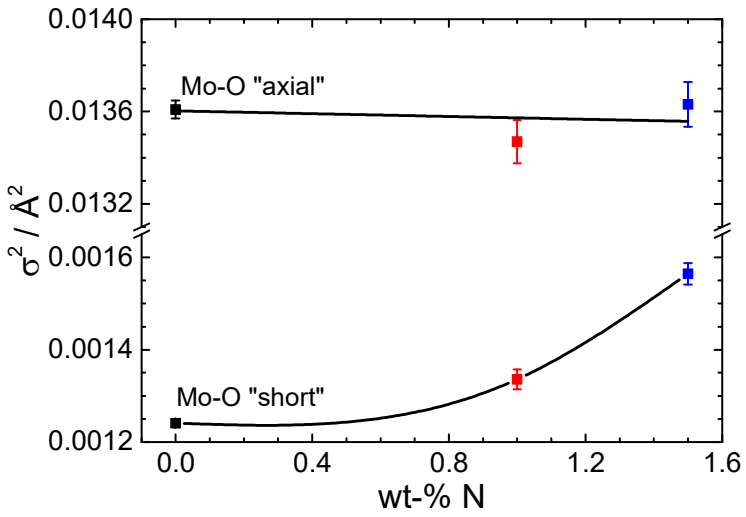

Figure 6-6: *Evolution of disorder parameter σ^2 of two Mo-O distances obtained by EXAFS refinements as a function of nitrogen content.*

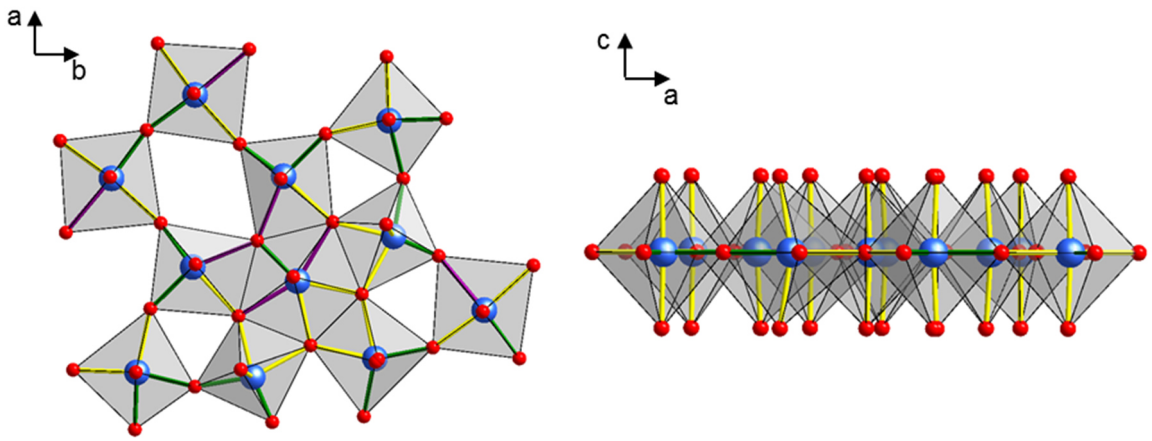

Figure 6-7: *Classification of Mo-O distances in three types of distances (short: green, middle: yellow, long: purple) for XAFS refinement.*

6.4.3 Temperature-programmed oxidation (TPO)

Increase of thermal stability constituted one crucial objective in synthesis of oxide nitrides with Mo_5O_{14} structure. Apparent activation energy of nitrogen removal was investigated by temperature-programmed oxidation (TPO) in 20% oxygen in helium to give information about the stability of incorporated nitrogen. The recorded ion currents of m/e 18 (water) showed one peak between 550 K and 575 K followed by removal of nitrogen indicated by ion current m/e 28 (**Figure 6-8**). Each peak shifted to higher

temperatures with increasing heating rate. The dependence of the peak shift on the heating rate can be analyzed by Kissinger method [130]. The Kissinger method was used for the evaluation of apparent activation energies of rate determining steps from TGA measurements. Here, it could be adapted to analysis of evolution of ion currents. The relationship between heating rate and apparent activation energy is given by **eq. (4-3).** Apparent activation energies can be estimated by plotting $ln(\beta/T^2_{max})$ vs. $1/T_{max}$. According to **eq. (4-3)** the apparent activation energies can be determined from the slope. It was assumed that these apparent activation energies could be assigned to the rate-determining steps of removal of water and nitrogen of the samples. The calculation resulted in activation energy of 132 kJ/mol for water removal and 278 kJ/mol for nitrogen removal. Hence, it can be assumed that oxygen ions were substituted by nitrogen ions and nitrogen was not adsorbed at the surface of the sample. Typical apparent activation energies for nitrogen and ammonia desorption of transition metal oxide surfaces are clearly below 100 kJ/mol [155,156]. Compared to nitrogen removal of MoO_3-type oxide nitrides, the apparent activation energy of nitrogen removal of Mo_5O_{14}-type oxide nitrides was more than 100 kJ/mol higher. Nitrogen removal of Mo_5O_{14}-type oxide nitrides was shifted to higher temperatures. Subsequently, Mo_5O_{14}-type oxide nitrides revealed a higher thermal stability during TPO in 20% oxygen compared to MoO_3-type oxide nitrides. Phase analysis of oxidized samples shared the formation of MoO_3 and $Mo_{2.4}V_{3.6}O_{16}$ (ICSD 644063, 202977).

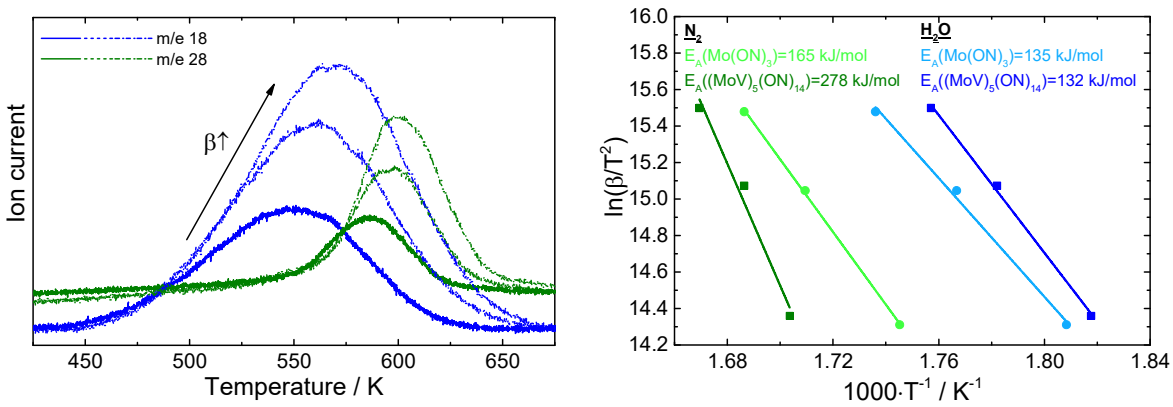

Figure 6-8: *Ion currents of m/e 18 (water, blue) and m/e 28 (nitrogen, green) during TPO with 5, 10 and 15 K/min of oxide nitride with Mo_5O_{14} structure (left). Apparent activation energies of water and nitrogen removal of both types of oxide nitrides were calculated out of a Kissinger plot (right).*

6.5 Compensation of additional negative charge of nitrogen ions

Incorporation of nitrogen ions in the anion lattice of $(MoV)_5O_{14}$ led to an additional negative charge by N^{3-} compared to O^{2-} which must be compensated. Charge compensation processes include [157]: (i) oxidation of metal centers (Mo or V), or (ii) additional incorporation of positive charges like H^+, e.g. in the form of $(NH)^{2-}$or (iii) generation of anion vacancies, e.g. $2NH_3 + 3O_O^X = 2N_O' + V_O^{\cdot\cdot} + 3H_2O$.

6.5.1 Average valence of metal centers

X-ray absorption near edge spectroscopy (XANES) was used to determine the average valence of the Mo and V metal centers. Mo K edge and V K edge XANES spectra of $(MoV)_5O_{14}$ and its corresponding oxide nitrides are given in the Appendix (**Figure A 3-1**, **Figure A 3-2**). Analyzing characteristic maxima in the Mo XANES spectra revealed the average valence of molybdenum metal centers [35]. Various molybdenum oxides (MoO_3, Mo_4O_{11}, and MoO2) were used as references for a correlation between average valence and energy of the Mo K-edge. Analysis of Mo-XANES spectra revealed an average molybdenum valence of 5.66 for the oxide and 5.61 for the oxide nitride with 1.0 and 1.5 wt-% nitrogen (**Figure 6-9**).

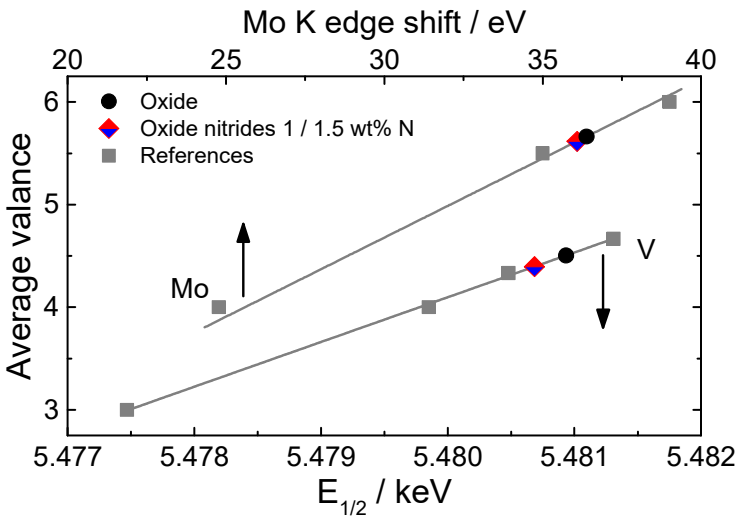

Figure 6-9: *Determination of average valences of molybdenum and vanadium in $(MoV)_5O_{14}$ (circle) and two oxide nitrides with different nitrogen contents (diamond). A set of references (squares) of each element was used for calibration of average valence to relative maximum of Mo K edge spectra and absorption edge position of V K edge spectra [35,158].*

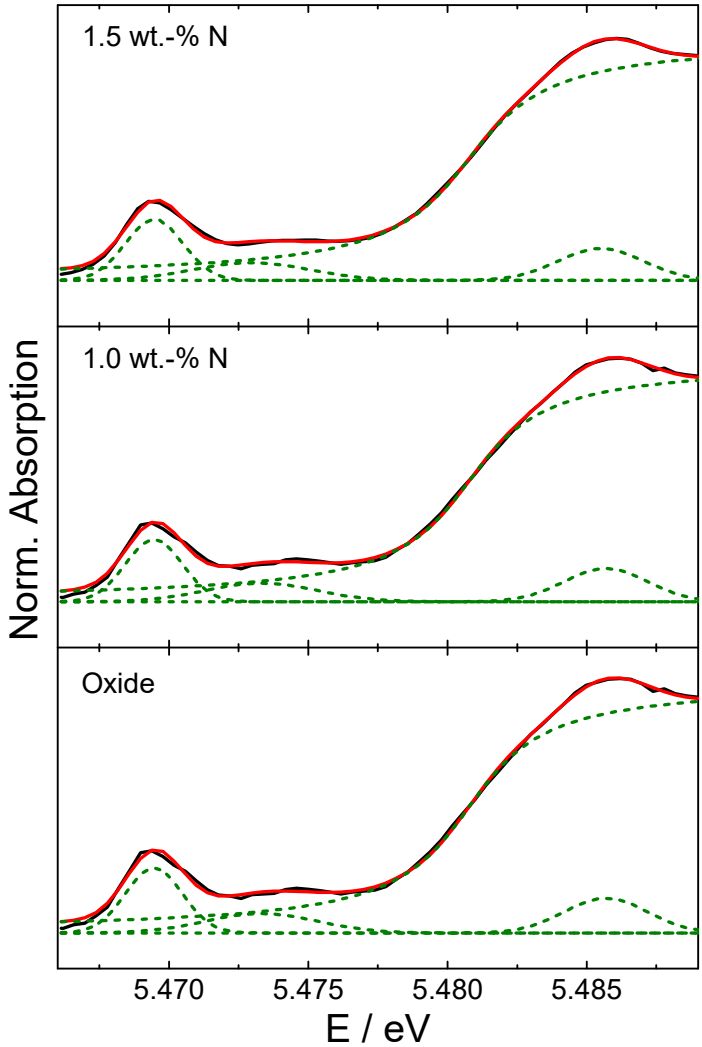

Figure 6-10: *Refinements of XANES data for V K edge using three Gaussian functions and one arctangent function of $(MoV)_5O_{14}$ and two oxide nitrides with different nitrogen contents.*

A refinement of three Gaussian functions and an arctangent function to simulate the absorption edge jump resulted in a good agreement with V XANES spectra (**Figure *6-10***) [158]. The centroid of the arctangent function represents the position of the absorption edge. Fitting of XANES spectra of a set of vanadium oxide references (V_2O_3, VO_2(M), V_6O_{13} and V_7O_{13}) yielded a linear dependency of the energy of the adsorption edge on the average valance. Refinements of the references spectra are shown in Appendix (**Figure A 3-3**). Applying this fitting method resulted in an average vanadium valence of 4.50 for the oxide and 4.40 for the oxide nitrides (**Figure 6-9**). In conclusion, analysis of XANES spectra revealed a minor changed average valence of metal centers. The average valence of metal centers should have been increased by 0.05 when

compensation of additional negative charge occurred by oxidation of metal centers. Hence, oxidation of metal centers to compensate additional negative charge could be excluded.

6.5.2 Fourier transform infrared spectroscopy (FTIR)

FTIR spectra were recorded to compare characteristic vibrational modes before and after ammonolysis (**Figure 6-11**). Refining Gaussian functions to the spectra resulted in maximum peak positions which are summarized in **Table 6-4**. The spectra showed the symmetric stretching vibrations of Mo=O group in a wavenumber range from 900 to 1000 cm^{-1}. The bands at lower wavenumber are due to asymmetric vibrations of Mo-O-Me (Me = Mo, V) and V-O-Mo bridging bonds [159–161]. After ammonolysis the same bands could be identified below 1000 cm^{-1}. Additionally, a slight shift of Mo-O-Me and Mo-O bands to lower wavenumbers was revealed by analysis of band positions in the FTIR spectra of Mo_5O_{14}-type oxide nitrides. Gallego reported a similar behavior in the characterization of $LaFeO_{3-X}N_X$ and attributed this shift to an incorporation of nitrogen in iron-oxygen octahedron [46]. This explanation may be adapted to the Mo_5O_{14} structure consisting of molybdenum-oxygen octahedron. Band shift to lower wavenumbers is connected with a weakening of the bond. Hence, decreasing metal-oxygen bond strength may lead to an increased oxygen mobility and altered redox properties for selective oxidation of propene [104,162]. Compared to the spectrum of oxides an additional band at 1055 cm^{-1} appeared in the spectrum of all oxide nitrides. This band could be assigned to the stretching mode of Mo-N bonds [163]. Detecting a Mo-N stretching mode indicated the incorporation of nitrogen atoms in the anion lattice of $(MoV)_5O_{14}$. Additionally, oxide nitrides with 1.3 and 1.5 wt-% nitrogen showed a N-H bending mode at 1405 cm^{-1} [49]. Hence, intensified treatment of $(MoV)_5O_{14}$ with ammonia resulted in the formation of incorporated $(NH)^{2-}$.

In summary, oxidation of Mo or V metal centers for charge compensation could be excluded by XAS measurements. An additional incorporation of $(NH)^{2-}$ was only detectable for samples with 1.3 and 1.5 wt% nitrogen. Elemental analysis of oxide nitrides confirmed the absence of hydrogen at 1.0 wt% nitrogen. Apparently, at low nitrogen contents the additional negative charge was only compensated by formation of oxygen

vacancies. Formation of $(NH)^{2-}$ might be parallel process by intensified treatment of $(MoV)_5O_{14}$.

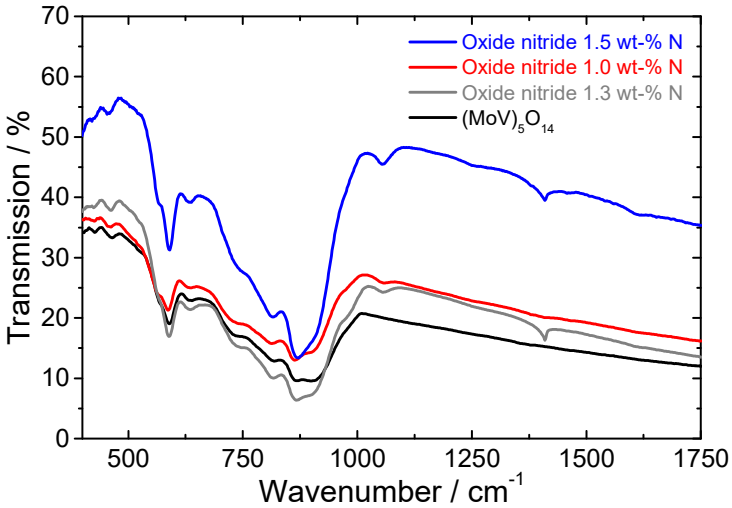

Figure 6-11: *FTIR-spectra of $(MoV)_5O_{14}$ and its corresponding oxide nitrides with different nitrogen contents. The positions and assignments of bands are listed in* **Table 6-4**.

Table 6-4: *Positions and assignments of refined FTIR bands of $(MoV)_5O_{14}$ and its corresponding oxide nitrides with different nitrogen contents.*

Oxide	Oxide nitride 1 wt.-% N	Oxide nitride 1.3 wt.-% N	Oxide nitride 1.5 wt.-% N	Vibration mode (Me=Mo,V)	
569	565	564	559	Mo-O-Me	[159]
592	589	589	585	V-O-Mo	[161]
628	632	632	631	Mo-O-Me	[160]
731	728	732	731	Mo-O-Me	[161]
814	810	813	813	Mo-O-Me	[159,161]
865	861	865	861	Mo-O-Me	[159,161]
909	904	907	895	Mo=O symmetric stretching	[159,161]
980	976	976	955	Mo=O symmetric stretching	[159,161]
---	1055	1057	1057	Mo-N stretching	[163]
---	---	1405	1409	N-H bending	[49]

6.6 Influence on electrical properties

6.6.1 Analysis of d.c. conductivity

Substitution of anions associated with formation of oxygen vacancies should strongly influence the electronic properties of the oxide nitrides. Electrical properties were measured by impedance spectroscopy. Nyquist plots (negative imaginary part of impedance *-Z''* vs. real part of impedance *Z'*) are shown in **Figure 6-12**. The spectrum of each sample measured at room temperature consisted of slightly depressed semicircles. The ohmic resistances were determined by refining an equivalent circuit to the experimental spectra. A parallel connection of an ohmic resistor *R* and a constant phase element (*CPE)* was used as an equivalent circuit [118]. Using a *CPE* instead of a capacitor *C* describes the deformation of semicircle in experimental data and represents a widely-used empirical model. Additionally, the ohmic resistor in the equivalent circuit has the practical advantage that d.c. conductivity can easily be determined by refining ohmic resistances *R* [118]. The refinement resulted in an increased conductivity with higher nitrogen contents. Bulk conductivities exhibited an exponential dependence on nitrogen content. The increase of electrical conductivity with higher substitution degree might be due to the formation of oxygen vacancies [164]. This will lead to an increase in mobility of lattice oxygen [39,165].

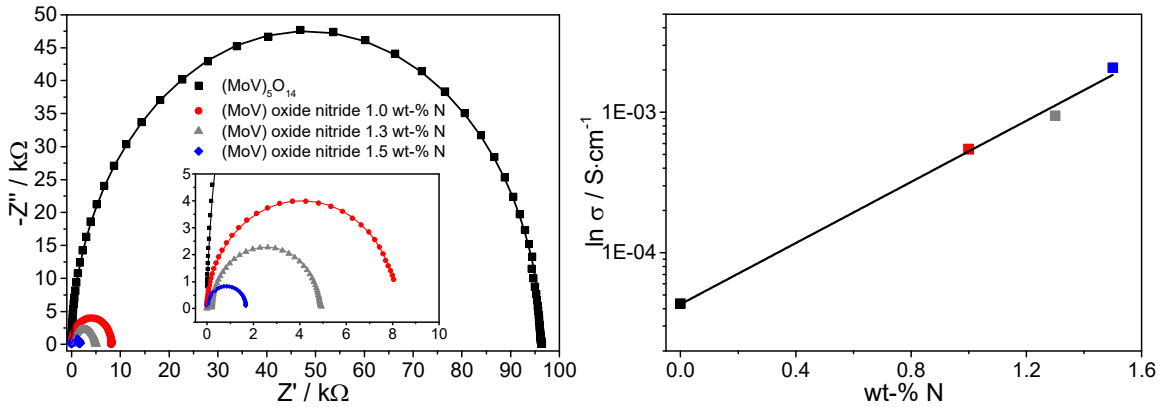

Figure 6-12: *Left: Nyquist presentation of impedance measurements of $(MoV)_5O_{14}$ and its corresponding oxide nitrides with different nitrogen contents at 298 K in a frequency range of 1 Hz – 10 MHz. Spectra of oxide nitrides are enlarged presented (inset).Right: D.c. conductivities as function of nitrogen content.*

The evolutions of d.c. conductivities of $(MoV)_5O_{14}$ and its corresponding oxide nitrides during thermal treatment in 20 % oxygen in nitrogen up to 650 K are shown in **Figure 6-13**. The temperature-dependent d.c. conductivities were also calculated from refined ohmic resistances. All samples exhibited a semiconducting behavior corresponding to an increasing conductivity with temperature. In contrast to $(MoV)_5O_{14}$ the conductivities of oxide nitrides slightly decreased in a temperature range of 550 K to 620 K. In the remaining temperature range the oxide nitrides showed also a semiconductor behavior. The increase of conductivities was dependent on nitrogen content of the sample. Analyzing the evolved gas phase by mass spectrometer revealed a release of nitrogen (*m/e* 28) in the same temperature range. After release of nitrogen the conductivities increased again before phase transition of $(MoV)_5O_{14}$ to MoO_3 started. Comparable studies on MoO_3-type oxide nitrides showed that conductivities after nitrogen removal were the same as α-MoO_3 [48]. Conversely, conductivities of Mo_5O_{14}-type oxide nitrides exhibited a dependence on nitrogen content above 620 K after removal of nitrogen. Apparently, structural defects caused by anion substitution in $(MoV)_5O_{14}$ were preserved after nitrogen removal in the temperature range of selective propene oxidation.

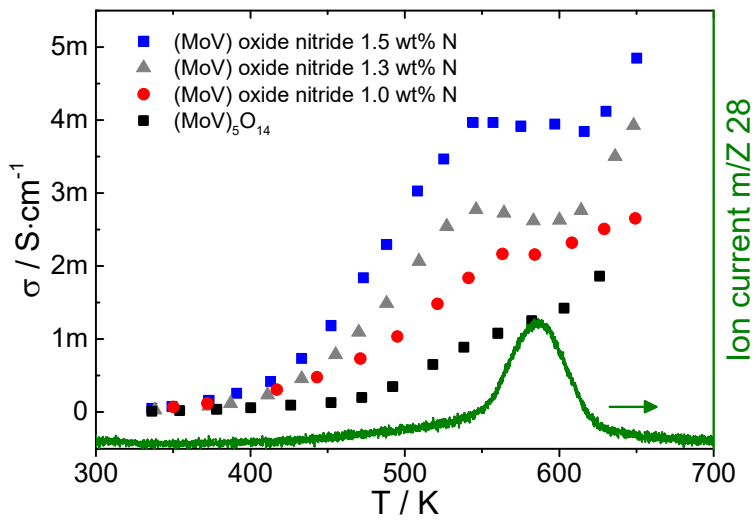

Figure 6-13: *Evolution of conductivities of $(MoV)_5O_{14}$ and its corresponding oxide nitrides with different nitrogen contents and evolution of ion current m/e 28 (nitrogen) of (MoV) oxide nitride with 1.0 wt.-% N during thermal treatment in air (green line).*

From an Arrhenius type presentation of conductivities of all samples up to 500 K apparent activation energies for extrinsic conduction were calculated (**Figure 6-14**). Because of nitrogen removal from 550 to 620 K and phase transformation above 673 K in air no reliable activation energies could be obtained at higher temperatures. The activation energies for extrinsic conduction decreased with higher degree of substitution of oxygen ions by nitrogen ions from 0.44 eV to 0.35 eV. The decreasing activation energies corroborated the formation of structural defects. Apparently, formation of oxygen vacancies led to changes in band structure. Consequently, electron transition from valence band to conduction band was facilitated.

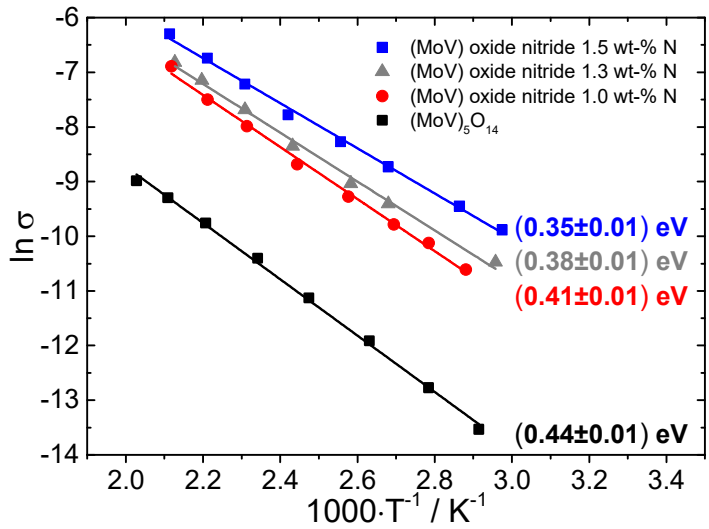

Figure 6-14: *Arrhenius-type presentation of conductivities of $(MoV)_5O_{14}$ and its corresponding oxide nitrides with different nitrogen contents. Activation energies of extrinsic conduction processes were calculated from the slope of linear evolution of conductivities.*

6.6.2 Analysis of a.c. conductivity

A more detailed explanation for differences in conductivities could be provided by an analysis of a.c. conductivity $\sigma_{a.c.}$. The frequency dependent a.c. conductivity was calculated from real and imaginary part of the impedance *Z'* and *Z''* using the relation

$$\sigma_{a.c.}(\omega) = \frac{1}{\sqrt{Z'^2 + Z''^2}}\left(\frac{l}{A}\right) \tag{6-3}$$

where *l* describes the thickness of the pellet and *A* the contact area to the electrodes. **Figure 6-15** shows the angular frequency dependent conductivities spectra of $(MoV)_5O_{14}$ measured in a temperature range of 335 K to 625 K. Two different regions were observed in the spectra. The low frequency range exhibited a frequency independent plateau region which corresponds to d.c. conductivity. Otherwise, at higher frequencies the a.c. conductivity increased with increasing angular frequency. This region is known as dispersive region. The hopping frequency ω_h indicates the frequency at which the dispersion takes place [166]. The a.c. conductivity spectra followed Jonscher's universal power law which explains the conductivity of solids:

$$\sigma_{a.c.}(\omega) = \sigma_{d.c.} + A\omega_h^n \text{ [167]}. \tag{6-4}$$

On the basis of this power law a non-linear refinement was carried out to determine hopping frequency ω_h and d.c. conductivity $\sigma_{d.c.}$. The refined values of $\sigma_{d.c}$ were in good agreement with results of refined equivalent circuits in **chap. 6.6.1**. The calculated values of *n* were in a range of 1.10 – 1.49 for $(MoV)_5O_{14}$. Hence, the hopping motion involved localized hopping without the species leaving the neighborhood [168]. From these results charge carrier concentration could be calculated by using following relationship between $\sigma_{d.c.}$ and ω_h:

$$\sigma_{d.c.} = \frac{K}{T}\omega_h \tag{6-5}$$

with $K = Ne^2a^2\gamma k^{-1}$ (*N*: charge carrier concentration, *e*: electron charge, *T*: temperature, *k*: Boltzmann constant). According to the literature the correlation factor γ was set to 1 and the distance between two adjacent sites was taken as 3 Å [169]. The charge carrier mobility μ was calculated by

$$\mu = \frac{\sigma_{d.c.}}{N \cdot e} \tag{6-6}$$

Performing this calculation procedure to spectra of all samples the charge carrier mobility as a function of temperature was calculated for all samples (**Figure 6-16**). The charge carrier mobility increased with higher temperatures. Similar differences concerning each sample were revealed compared to d.c. conductivities. The nitrogen

removal led to a slight decrease in charge carrier mobility. Above 550 K spectra of the oxide nitride with 1.5 wt% nitrogen did not follow the mentioned power law. Additionally, the charge carrier concentration did not change significantly during thermal treatment of each sample. Thus, all changes in conductivities could be attributed to a modification of charge carrier mobility after ammonolysis of $(MoV)_5O_{14}$.

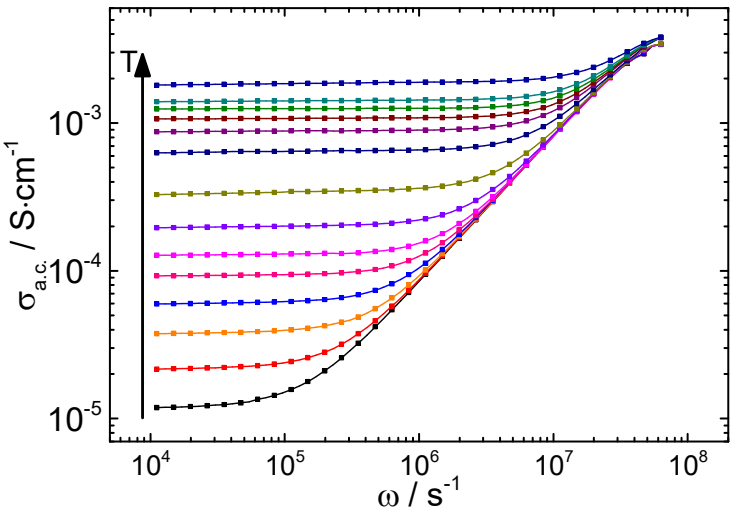

Figure 6-15: *Frequency dependence of a.c. conductivity of $(MoV)_5O_{14}$* in a temperature range of 336 – 626 K in 20 % oxygen in nitrogen.

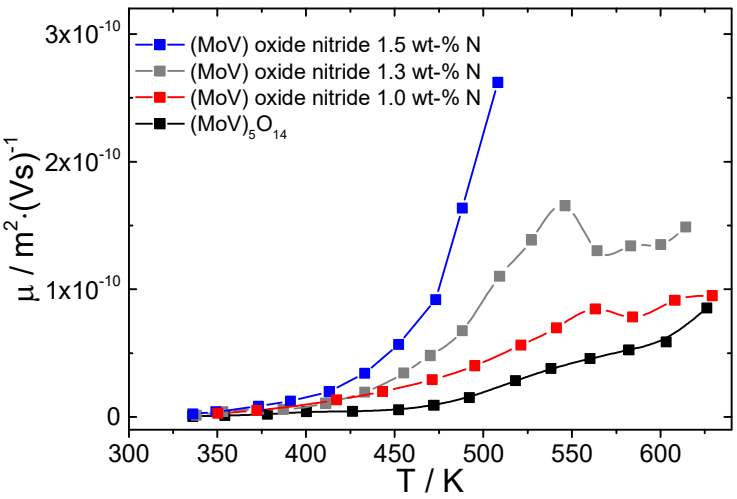

Figure 6-16: *Evolution of charge carrier mobility during thermal treatment in 20 % oxygen in nitrogen of $(MoV)_5O_{14}$ and its corresponding oxide nitrides with different nitrogen contents.*

6.6.3 Dependency of conductivity on oxygen partial pressure

The total conductivity in a solid oxide can be classified in three types: electronic p-type (σ_p) or n-type (σ_n) and ionic conductivity (σ_{ion}). Each conductivity type shows a different dependency on oxygen partial pressure [121]:

$$\frac{\delta\sigma_p}{\delta p_{O_2}} > 0 \tag{6-7}$$

$$\frac{\delta\sigma_n}{\delta p_{O_2}} < 0 \tag{6-8}$$

$$\frac{\delta\sigma_{ion}}{\delta p_{O_2}} = 0 \tag{6-9}$$

The total conductivity σ_{tot} is given by the sum of the three types. Conductivity of electronic conductors changes with partial oxygen pressure as $p_{O2}^{-1/4}$ or $p_{O2}^{+1/4}$. According to **eq. (6-10)** the ionic conductivity can be determined by plotting σ_{tot} as a function of $p_{O2}^{-1/4}$ or $p_{O2}^{+1/4}$, respectively. However, in many cases the dependence of σ_{tot} on oxygen partial pressure is significantly weaker than in ideal cases given by the exponent *n* in $p_{O2}^{\pm 1/n}$ [170]. The value of *n* gives information how ionic conductivity governs the electronic conductivity.

$$\sigma_{tot} = \sigma_{ion} + \sigma_n + \sigma_p = \sigma_{ion} + k \cdot p_{O_2}^{-1/4} + k \cdot p_{O_2}^{+1/4} \tag{6-10}$$

The total conductivity σ_{tot} of $(MoV)_5O_{14}$ and its oxide nitride with 1 wt% nitrogen is shown in **Figure 6-17** as a function of oxygen partial pressure. The determination of exponent *n* revealed that both samples were mixed p-type semiconductors ($n > 0$). This type of conductivity could be attributed to existence of acceptor levels. In addition, the ratio of σ_{ion} to σ_{tot} was calculated and is given in **Table 6-5**. The substitution of O^{2-} by N^{3-} led to a significant increase in contribution of σ_{ion}. σ_{tot} was almost independent of p_{o2}. The mobility of O^{2-} and the concentration of oxygen vacancies influence the oxygen ion conductivity. Recent studies on ionic conductivity of N^{3-} indicated a fast nitrogen ion conductivity [171]. Hence, incorporation of N^{3-} led to a higher concentration of mobile ions.

The absolute value of σ_p was also increased after ammonolysis. The orbital energy of nitrogen 2p orbitals is slightly higher than the O 2p orbital energy [172]. Hence, new acceptor levels were formed by ammonolysis. Additionally, energy levels of formed vacancies are located close to the valence band. Subsequently, σ_p was increased due to conduction of electrons [170].

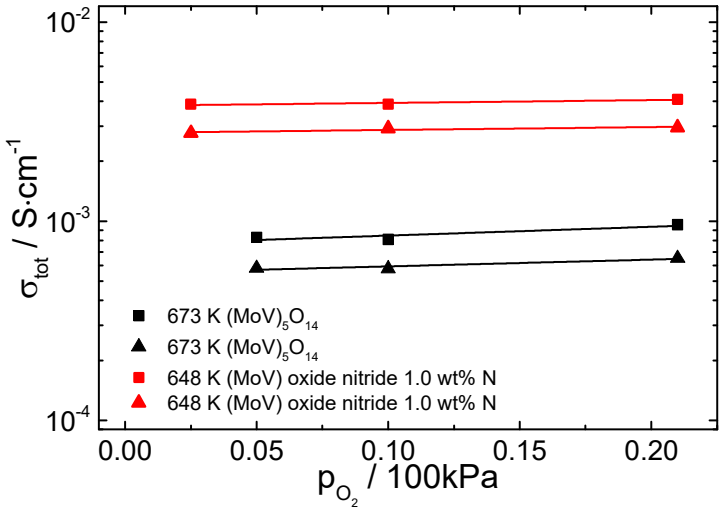

Figure 6-17: *Total conductivity as a function of partial oxygen pressure of $(MoV)_5O_{14}$ and its oxide nitride with 1 wt% N at 648 K and 673K.*

Table 6-5: *Electrochemical properties of $(MoV)_5O_{14}$ and its oxide nitride with 1 wt% N.*

	n ($p_{O2}^{\pm 1/n}$) 648 K	n ($p_{O2}^{\pm 1/n}$) 673 K	σ_{ion} / σ_{tot} 648 K, 21kPa	σ_{ion} / σ_{tot} 673 K, 21kPa
Oxide	9.7	12.5	0.52	0.65
Oxide nitride 1 wt.-% N	31.7	39.5	0.85	0.87

6.7 Conclusion

Substituting oxygen ions in the anion lattice of $(MoV)_5O_{14}$ with nitrogen ions preserved the Mo_5O_{14} structure. Nitrogen content of the Mo_5O_{14}-type oxide nitrides could be adjusted by varying temperature and ammonia gas flow. Average valence of metal centers was not affected by incorporation of nitrogen. The additional negative charge of incorporated nitrogen atoms compared to oxygen atoms was mainly compensated by formation of oxygen vacancies. Samples with higher nitrogen content showed an additional formation of $(NH)^{2-}$. Incorporation of nitrogen ions weakened the average metal-oxygen bond strength. Investigations of electrical properties were carried out using impedance spectroscopy. Incorporation of nitrogen ions resulted in a correlation between increasing conductivity and nitrogen content. Hence, the formation of oxygen vacancies led to changes in band structure and eased electron hopping from the valence to the conduction band. Structural characterization was performed by XRD and XAFS. Both methods revealed complementary results by analyzing long-range and short-range structure. Incorporation of nitrogen ions led to increasing XAFS disorder parameter and lattice strain (XRD). A structure-function correlation between structural parameters and d.c. conductivity could be described (**Figure 6-18**).

Temperature-programmed oxidation revealed remaining differences of conductivity of Mo_5O_{14}-type oxide nitrides after nitrogen removal. Furthermore, an improved stability during TPO compared to MoO_3-type oxide nitrides was determined which can be associated to the non-layer structure of Mo_5O_{14}. The improved stability during TPO might also lead to an improved stability during treatment under reaction conditions. Compared to previous studies on MoO_3-type oxide nitrides this range of molybdenum-based oxide nitrides could be successfully applied to a more relevant system for studies in selective oxidation of propene.

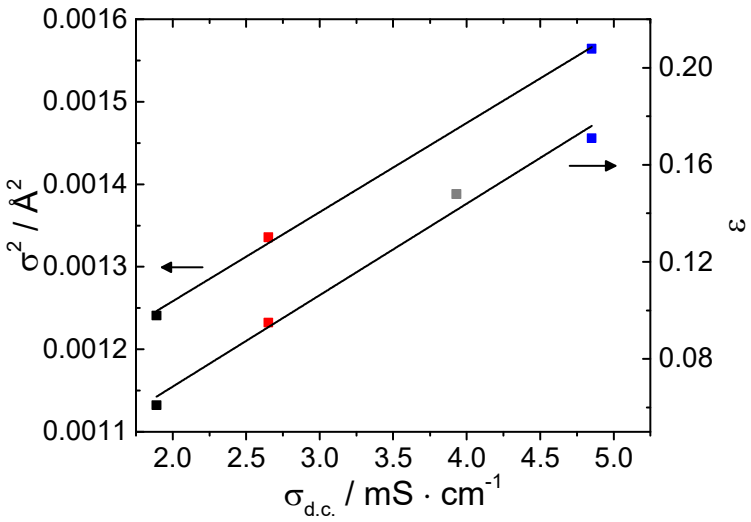

Figure 6-18: *Structure-function correlation between structural disorder parameter, lattice strain and d.c. conductivity of mixed molybdenum oxide nitrides with Mo_5O_{14} structure.*

7 *In situ* characterization of mixed molybdenum oxide nitrides

7.1 Introduction

Oxygen ions of $(Mo,V)_5O_{14}$ were successfully substituted by nitrogen ions via ammonolysis to prepare mixed molybdenum oxide nitride. Investigations on the ammonolysis products of $(Mo,V)_5O_{14}$ showed oxide nitrides with a preserved crystal structure and an invariant cation composition. The substitution resulted in a significant dependence of conductivity on degree of substitution. The dependence was preserved after nitrogen removal. Studies on MoO_3-type oxide nitrides showed that reducibility was significantly influenced by ammonolysis. Reducibility is expected to be a crucial property of catalysts in selective oxidation reactions and describes the ease of the oxygen extraction from a catalyst [21,173]. Hence, TPR measurements were carried out to investigate oxygen mobility. Enhancing thermal stability of oxide nitrides constitutes an essential objective of this work. Compared to MoO_3-type oxide nitrides an improved stability of oxide nitrides can be assumed due to an increased apparent activation energy of nitrogen removal during TPO. Structural characterization by complementary XRD and XAS revealed an increasing structural disorder as a function of nitrogen content. Both methods represent well-known analytical methods for *in situ* investigations [125]. Accordingly, *in situ* experiments under catalytic conditions might give information about stability during treatment under reaction conditions. Gas phase composition during selective propene oxidation was determined by online mass spectrometry und gas chromatography at different temperatures to elucidate relationships between electronic properties and catalytic performance.

7.2 Experimental

7.2.1 Temperature-programmed reduction with H_2

Temperature-programmed reduction (TPR) experiments were carried out with a catalyst analyzer from BEL Japan Inc. equipped with a silica glass tube reactor. Samples were placed on silica wool inside the reactor next to a thermocouple. A gas flow (5% hydrogen in argon) of 60 ml/min was adjusted during reaction. Heating rates used were 5, 10, 15 K/min to 1023 K while hydrogen consumption was measured using a TCD. For measurements 30 mg of samples were used.

7.2.2 X-Ray Absorption spectroscopy (XAS)

Transmission X-ray absorption spectroscopy (XAS) was performed at the V K edge (5.465 keV) and the Mo K edge (19.999 keV) at beamline C, and X1, respectively, at the Hamburg Synchrotron Radiation Laboratory, HASYLAB, using a Si(111) (V K edge) or Si(311) (Mo K edge) double crystal monochromator. Boron nitride (hexagonal, Alfa Aesar, 99.5%) was used as diluent for *in situ* measurements. Mixtures of samples and boron nitride were pressed into self-supporting pellets with a diameter of 5 mm. References were diluted with wax (Hoechst wax C micropowder, Merck) and pressed into self-supporting pellets with a diameter of 13 mm for *ex situ* measurements. Sample masses were calculated to result in an edge jump of $\Delta\mu(d)$ = 1.5 at the Mo K edge and $\Delta\mu(d)$ = 0.3 at the V K edge.

TPR experiments were carried out in an *in situ* XAS flow reactor at atmospheric pressure with flowing reactants (5% propene in helium, ~30 ml/min) and in a temperature range from 298 K to 763 K (5 K/min) [174]. Holding time at 763 K of the oven was aborted when no structural change could be observed. In situ experiments under catalytic conditions were carried out in a gas mixture of 5 % propene and 5 % oxygen in helium (~30 ml/min) while the reactor was heated up to 723 K with 5 K/min. Reactant gas flow rates of propene, and helium were adjusted through separate mass flow controllers (Bronkhorst). Additionally, a mass spectrometer (Omnistar, Pfeiffer) was connected to continuously monitored reactant and product gas composition.

Data analysis was performed using the software package WinXAS v.3.2 [88]. Background subtraction and normalization were carried out by fitting a linear polynomial to the pre-edge region and a third degree polynomial to the post-edge region, respectively. The X-ray absorption fine structure (EXAFS) $\chi(k)$ at the Mo K edge was extracted by using cubic splines to obtain a smooth atomic background, $\mu_0(k)$ in the k range from 3 to 14 $Å^{-1}$. The radial distribution function $FT(\chi(k)\cdot k^3)$ was calculated by Fourier transformation of the k^3-weighted experimental $\chi(k)$ function, multiplied by a Bessel window, into the R space. XAS structural model and refinement procedure is described in **chap. 6.4.**

7.2.3 X-ray diffraction (XRD)

In situ XRD measurements were conducted on a STOE STADI P diffractometer (θ-θ geometry) using an Anton-Paar *in situ* cell. The experiments were carried out in a temperature range from 323 K to 698 K (effective heating rate 0.14 K/min) and in 5% propene and 5% oxygen in He. Measurements were performed in reflection mode in a range of 20 – 47° 2θ in steps of 0.02° 2θ with a sampling time of 5 s/step. The 2θ range was increased to 20 – 63° 2θ for all measurements at 323 K. A total flow of 100 ml/min was adjusted by mass flow controllers (Bronkhorst). The gas phase composition at the cell outlet was continuously monitored using a non-calibrated mass spectrometer in a multiple ion detection mode (Pfeiffer Omnistar). Data analysis was performed by using software packages WinXAS v.3.2 and FullPROF suite program 1.10 [86–88].

7.2.4 Catalytic characterization

Catalytic activities were measured in a conventional fixed bed reactor connected to an online gas chromatography system (CP-3800, Varian). The fixed-bed reactor consisted of a SiO_2 tube (length 30 cm, inner diameter 9 mm) placed vertically in a tube furnace. The sample was placed on a frit in the center of the isothermal zone. The catalyst bed in the reactor was approximately 2 cm in height. To achieve a constant volume in the reactor and to quench thermal effects, catalyst samples (about 50 mg) were diluted with boron nitride (hexagonal, Alfa Aesar, 99.5%) to result in an overall sample mass of 250 mg. To

ensure differential reaction conditions, the reactor was operated at low propene conversion levels below 10 %.

Hydrocarbons and oxygenated reaction products (acetic aldehyde, propionic aldehyde, acetone, acrolein, isopropyl alcohol, n-propanol, allyl alcohol, acetic acid, propionic acid, acrylic acid, acrylonitrile, acetonitrile, and propionitrile) were analyzed using a Carbowax 52CB capillary column, connected to an Al_2O_3/MAPD capillary column, and a fused silica restriction (25 m, 0.32 mm), respectively. Each column was connected to a flame ionization detector. O_2, N_2, CO_2 and CO were separated and analyzed using a Varian CP-3800 permanent gas analyzer connected to a thermal conductivity detector.

Reactant gas flow rates of oxygen, propene, and helium were adjusted through separate mass flow controllers (Bronkhorst) to a total flow of 40 ml/min. A mixture of 5% propene and 5% oxygen in helium was used for catalytic testing in the range of 648 - 698 K. Additionally, a mass spectrometer (Omnistar, Pfeiffer) was connected to continuously monitored reactant and product gas composition.

Conversion X of the key component k and selectivity S towards product p_n were calculated from the measured volume fractions, *Vol%*, according to **eq. (5-1)** and **eq. (5-2)**. The carbon balances were always higher than 0.98 (**eq. (5-3)**). The reaction rates for one compound were calculated from **eq. (5-4)**. The experimental error of the given reaction rates and selectivities was estimated from the relative errors of reactant gas flow rates and catalyst sample masses.

7.2.5 Elemental analysis

Amounts of C, H and N were in the samples determined by using an analyzer (FlashEA 1112 NC, ThermoFinnigan/ThermoElectron) with CHNS-O configuration. In addition to measurements of samples as prepared, measurements were carried out to determine nitrogen contents of treated samples.

7.3 Reducibility of Mo_5O_{14} and its corresponding oxide nitrides

According to the mentioned redox mechanism, availability of lattice oxygen plays an important role for selective oxidation of propene. Temperature-programmed reduction

experiments (TPR) are commonly used for characterizing the availability of lattice oxygen of catalysts in selective oxidation reactions [175,176]. In a first step reducibility in 5% hydrogen in helium was investigated (**Figure 7-1**). The evolution of hydrogen consumption of all samples showed one peak attributed to the reduction to MoO_2. The peak shifted to higher temperatures with increasing heating rate. The maximum of hydrogen consumption was shifted to lower temperatures after ammonolysis of $(MoV)_5O_{14}$. According to **eq. (4-3)** the Kissinger method was used to determine the apparent activation energies of reduction to MoO_2 [130]. The calculation resulted in an apparent activation energy of 217 kJ/mol for $(MoV)_5O_{14}$ and 185 kJ/mol for its oxide nitride with 1.0 wt% N. Reducibility of mixed molybdenum oxides was significantly influenced by substitution of lattice oxygen ions by nitrogen ions.

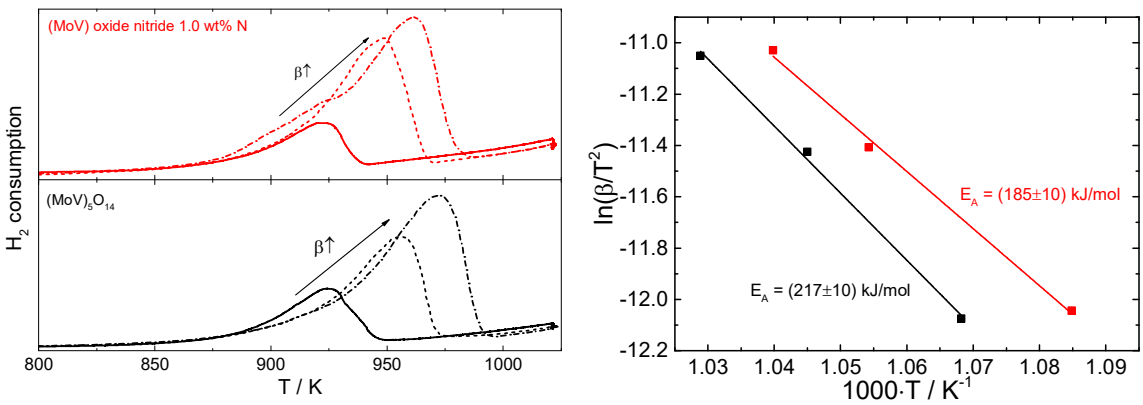

Figure 7-1: *Left: Hydrogen consumption during TPR of $(MoV)_5O_{14}$ and oxide nitride with 1.0 wt% N. Right: Kissinger plot for determination of apparent activation energies of reduction of $(MoV)_5O_{14}$ and oxide nitride with 1.0 wt% N to MoO_2 according to* ***eq. (4-3)****.*

Additionally, reducibility of $(MoV)_5O_{14}$ and the corresponding oxide nitrides in propene was investigated using *in situ* XAS during TPR in 5% propene in helium up to 763 K (**Figure 7-2**). Phase transformation of $(MoV)_5O_{14}$ to MoO_2 was observed at 700 K. The reduction of $(MoV)_5O_{14}$ proceeded in a one-step reaction to MoO_2 without any detectable intermediate phases [20]. The measured XANES spectra were fitted with a linear combination (LC) of $(MoV)_5O_{14}$ and MoO_2 reference spectra to determine the phase composition during TPR (**Figure 7-3**). The respective α-traces were calculated from the phase composition during TPR. A strong dependence of the onset of reduction on nitrogen content was shown. The onset temperature was lowered from 700 K to 650 K by

incorporation of nitrogen. Because of the similar long-range structure and crystallinity, the improved reducibility of the oxide nitrides can be attributed to an increased availability of lattice oxygen. This increased oxygen availability correlated with an increased density of oxygen vacancies. A linear correlation could be established between temperature of extent of reduction α = 0.5 (phase ratio Mo_5O_{14}:MoO_2 = 1) and conductivity. Reducibility describes the lattice oxygen availability. Subsequently, the found relation corroborated that the increasing conductivity was associated with increasing oxygen availability.

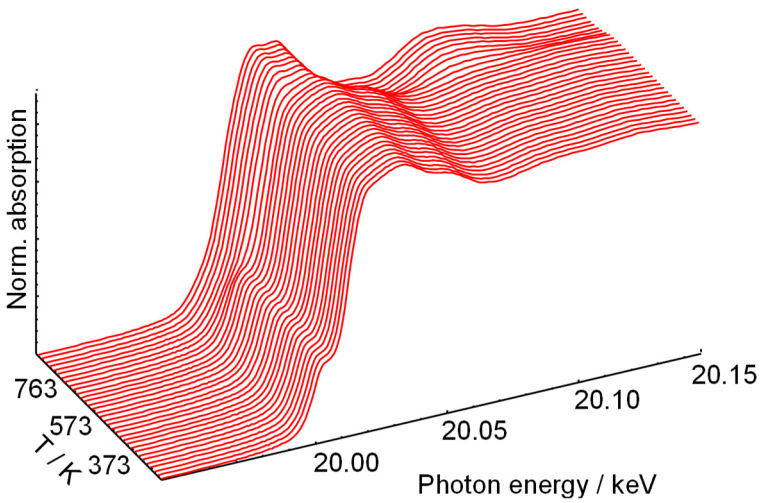

Figure 7-2: *Evolution of in situ XANES spectra (MoV) oxide nitride with 1.0 wt% N during TPR from 300 K to 763 K (5% propene in He).*

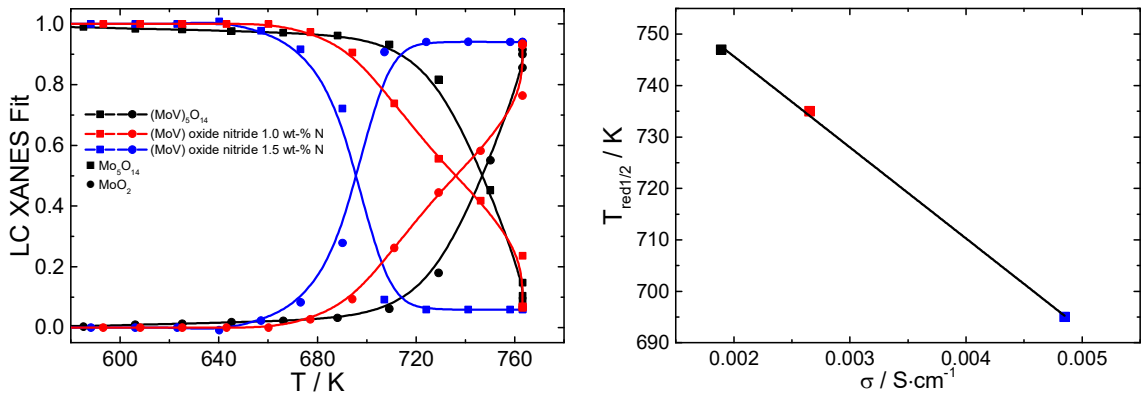

Figure 7-3: *Left: Evolution of phase composition during TPR in 5 % propene up to 763 K of $(MoV)_5O_{14}$ and its oxide nitrides with 1.0 and 1.5 wt% N. Right: Temperatures at a conversion degree α = 0.5 during TPR as a function of conductivities of impedance measurements indicated a correlation between conductivity and oxygen availability.*

Evolution of ion currents of *m/e* 14 (nitrogen) during TPR and the amount of Mo_5O_{14} is shown in **Figure 7-4**. Ion currents of both oxide nitride samples showed a peak which was attributed to removal of nitrogen. The peak of the sample with higher nitrogen content was more intensive and shifted to lower temperatures. The onset of nitrogen removal started after 10% of Mo_5O_{14} were transformed to MoO_2. Hence, it might be assumed that the removal of nitrogen was promoted by the transformation of tetragonal in monoclinic crystal system.

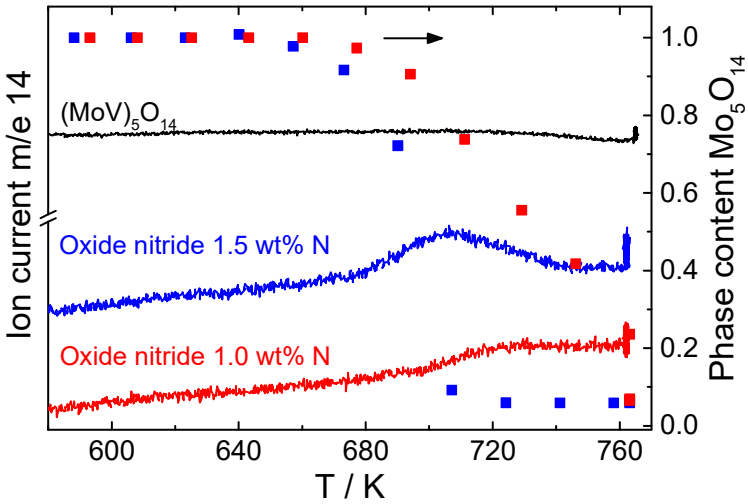

Figure 7-4: *Evolution of phase content of Mo_5O_{14} of oxide nitrides with 1.0 and 1.5 wt% N (squares) and ion current m/e 14 (nitrogen) of $(MoV)_5O_{14}$ and its oxide nitrides with 1.0 and 1.5 wt% N during TPR in 5 % propene up to 763 K.*

XANES spectra of reduced samples after TPR in 5% propene up to 763 K are shown in **Figure 7-5**. Mo XANES spectra exhibited a similar trend as the reference spectrum of MoO_2. The average valence of Mo was determined by analyzing the relative maximum position to the Mo K edge according to correlation in **Figure 6-9** [35]. The average valence amounted to 3.9 for all samples which is close to that of MoO_2. In addition, the pseudo radial distributions, $FT(\chi(k)\cdot k^3)$, of all samples showed a similar shape to the $FT(\chi(k)\cdot k^3)$ of MoO_2 [177]. Theoretical $FT(\chi(k)\cdot k^3)$ of structure model of MoO_2 could be refined to experimental data with good agreement (**Table A 4-1**). Significance of the fitted parameters was determined by calculating confidence limits and statistical F parameters. The XAFS spectra could be well described by three Mo-O and four Mo-Mo distances. The resulting atom distances and disorder parameters, σ^2, of all samples showed no significant differences. The trend of V K edge XANES spectra of all samples after TPR was similar to the reference spectrum of V_2O_3 in agreement with previous investigations on $(MoV)_5O_{14}$ [30]. The same average valence of vanadium was calculated for all samples.

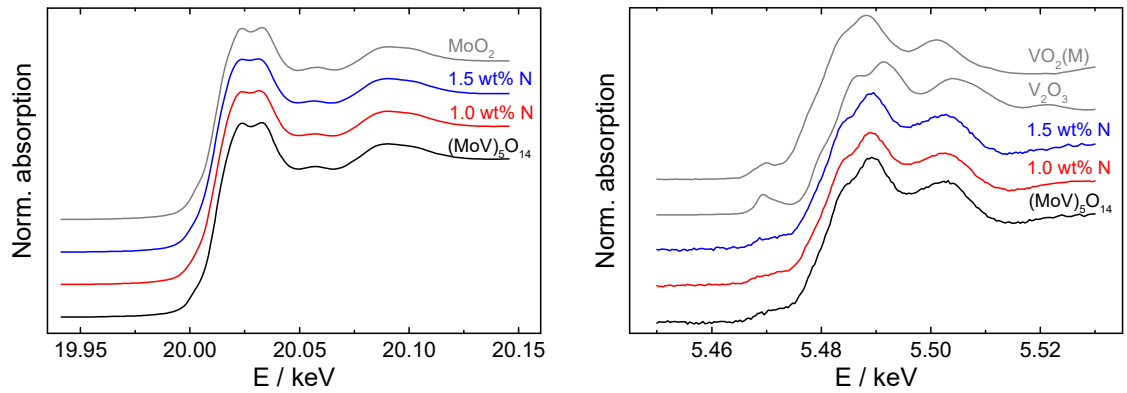

Figure 7-5: *XANES spectra of reduction products (TPR in 5 % propene/He up to 763 K)* of *$(MoV)_5O_{14}$, its oxide nitrides with 1.0 and 1.5 wt% N* and selected references at Mo K edge (left) and V K edge (right).

7.4 Stability during treatment under reaction conditions

7.4.1 X-Ray diffraction (XRD)

Previous characterization showed that ammonolysis of $(MoV)_5O_{14}$ influenced structural parameters (lattice parameters and lattice strain, **chap. 6.4.1**). *In situ* XRD measurements during treatment under reaction conditions were carried out to

investigate structural evolution and stability of oxide nitrides. Evolution of *in situ* XRD powder patterns of tetragonal $(MoV)_5O_{14}$ and its corresponding oxide nitride with 1.5 wt% nitrogen is shown in **Figure 7-6**. According to the literature crystal structure of $(MoV)_5O_{14}$ was stable during treatment under reaction conditions up to 698 K [20]. In addition, tetragonal Mo_5O_{14}-structure of Mo_5O_{14}-type oxide nitride was preserved. The known linear expansion of lattice parameter *c* with temperature was also observed for oxide nitride similar to that of $(MoV)_5O_{14}$. Conversely, the evolution of the *a* parameter showed differences (**Figure 7-7**). Lattice parameter *a* of $(MoV)_5O_{14}$ remained constant during first treatment under reaction conditions. An intermediate expansion with maximum elongation at 648 K of *a* parameter was observed. In agreement with Rietveld refinements of the Mo_5O_{14} crystal structure to XRD powder patterns of samples as prepared the *a* parameter of oxide nitride was increased at the beginning of treatment under reaction conditions compared to $(MoV)_5O_{14}$. A slight decrease of the *a* parameter was observed above 623 K. During the second treatment under reaction conditions the evolution of *a* parameter was similar to that of $(MoV)_5O_{14}$ up to 648 K.

Determination of lattice strain was carried out by Williamson-Hall analysis of 20 selected *hkl* diffraction peaks using **eq. (6-1)**. The Williamson-Hall plot resulted in straight lines. Lattice strain was calculated from the slope for each measurement. The evolution of lattice strain as a function of temperature is shown in **Figure 7-7**. The lattice strain of $(MoV)_5O_{14}$ slightly decreased at around 600 K followed by an increase up to 698 K. During the second treatment under reaction conditions lattice strain of $(MoV)_5O_{14}$ increased linear with temperature. Comparing both successive treatments, no significant differences in lattice strain were observed in a temperature range of 623 to 698 K. Lattice strain of Mo_5O_{14}-type oxide nitride increased linear with temperature up to 623 K in both runs. Afterwards, lattice strain decreased strongly and remained almost constant with increasing temperature up to 698 K.

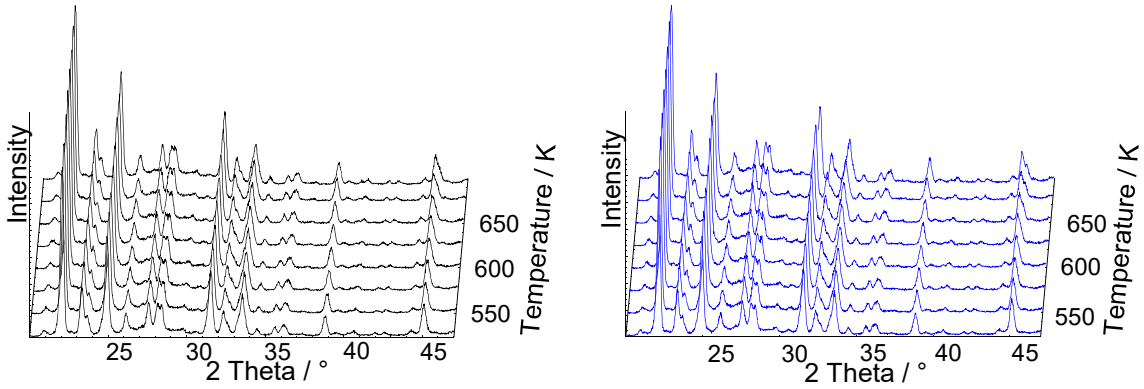

Figure 7-6: *Evolution of XRD powder patterns during treatment in 5% propene, 5% oxygen in He. Left: $(MoV)_5O_{14}$, right: Mo_5O_{14}-type oxide nitride.*

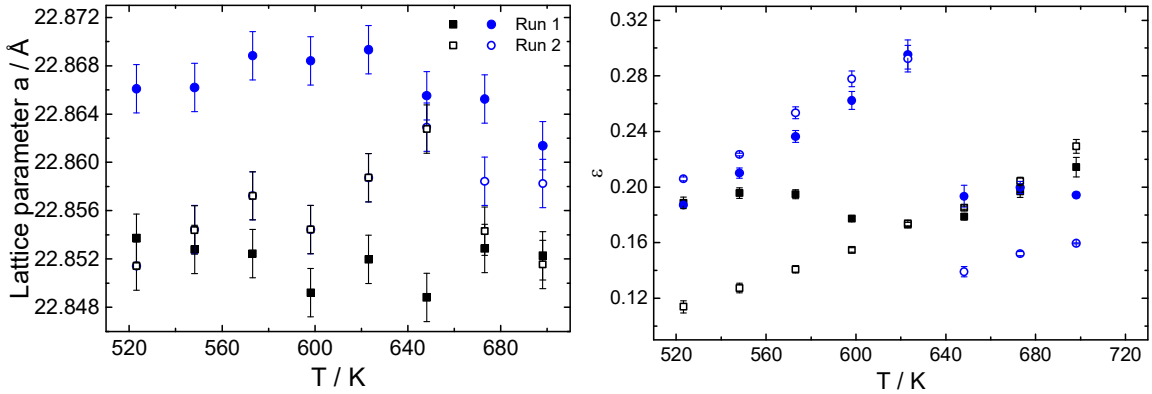

Figure 7-7: *Evolution of lattice strain of $(MoV)_5O_{14}$ and its oxide nitride during two consecutive treatments in 5% propene, 5% oxygen in He up to 698 K.*

In addition to analysis of *in situ* data, a Williamson-Hall analysis of XRD powder patterns measured at 323 K before and after each treatment under reaction conditions was carried out. Structural changes can be investigated without taking into account of influences of temperature on lattice strain (**Figure 7-8**). All Williamson-Hall plots resulted in straight lines indicating a homogenous distribution of lattice strain and particle size. A slight decrease of lattice strain was observed after each treatment under reaction conditions of $(MoV)_5O_{14}$ (**Table *7-1***). Lattice strain of oxide nitride decreased significant during first catalytic treatment. In contrast to $(MoV)_5O_{14}$, the lattice strain of oxide nitride remained constant during the second treatment under reaction conditions. After treatment under reaction conditions, lattice strain of oxide nitride was increased compared to that of starting $(MoV)_5O_{14}$. A decreasing lattice stain might be associated

with a partial removal of nitrogen. Elemental analysis of treated samples resulted in residual nitrogen content of 0.25 wt%. Consequently, Mo_5O_{14}-type oxide nitrides showed an increased stability during treatment under reaction conditions compared to MoO_3-type oxide nitrides.

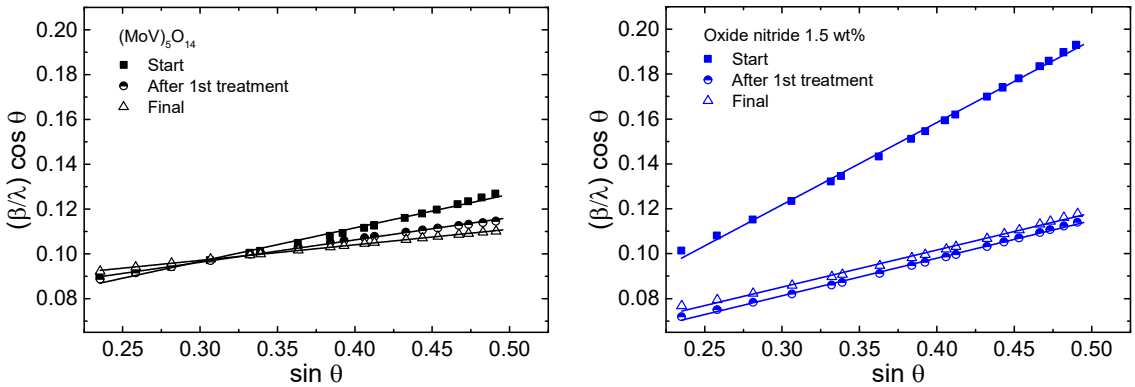

Figure 7-8: *Williamson-Hall analysis of XRD powder patterns at 323 K before treatment, after first and second treatment under reaction conditions.*

Table 7-1: *Lattice strain of $(MoV)_5O_{14}$ and oxide nitride with 1.5 wt% N before, after first and second treatment under reaction conditions calculated from Williamson-Hall analysis.*

	Oxide	**Oxide nitride 1.5 wt.-% N**
Start	0.057	0.141
After 1st treatment	0.038	0.064
Final	0.027	0.064

After *in situ* XRD experiment in catalytic atmosphere, a TPO of the Mo_5O_{14}-type oxide nitride was carried out. The evolution of ion currents (*m/e* 14, 18, 28, 32, 44) during TPO is shown in **Figure 7-9**. At temperatures below 373 K a peak of *m/e* 18 was observed which was attributed to water adsorbed at the surface of the catalyst. A peak of m/e 28 and *m/e* 44 was identified at 615 K combined with a decrease of *m/e* 32. The peak of *m/e* 28 was attributed to the formation of CO because an increase of *m/e* 14 (nitrogen) was not observed. Adsorbed hydrocarbon species of treatment under reaction conditions were desorbed and oxidized to CO/CO_2 and water. A second peak of *m/e* 28 was observed at 765 K. On the basis of the additional peak of *m/e* 14 at the same temperature the

peaks were attributed to nitrogen removal. Subsequently, the analysis of ion currents during TPO corroborated the results of elemental analysis of treated samples. Treated oxide nitrides still contained a residual amount of nitrogen.

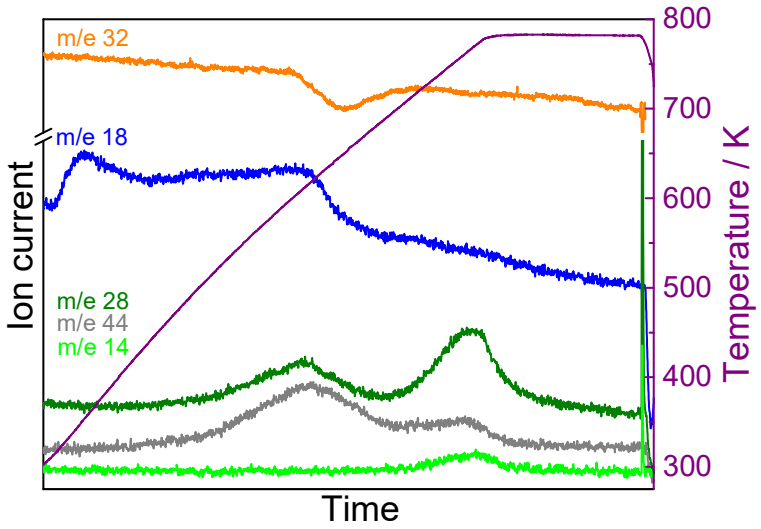

Figure 7-9: *Evolution of ion currents (m/e 14, 18, 28, 32, 44) during TPO of oxide nitride after treatment under reaction conditions. Associated temperature program is indicated by purple line.*

7.4.2 X-ray absorption spectroscopy (XAS)

Evolution of *in situ* XANES spectra of $(MoV)_5O_{14}$ and oxide nitrides with 1.0 and 1.5 wt% nitrogen during treatment under reaction conditions is shown in **Figure A 4-1**. It confirmed the results of *in situ* XRD experiments that the Mo_5O_{14}-structure was preserved during treatment under reaction conditions. A slight shift of relative Mo K edge position to lower energies was observed after ammonolysis of $(MoV)_5O_{14}$. In addition, investigations on MoO_3 and its corresponding oxide nitrides revealed a correlation between the slight shift of relative Mo K edge position and stability of oxide nitrides. The evolution of Mo K edge shift of $(MoV)_5O_{14}$ and oxide nitrides with 1.0 and 1.5 wt% N was determined from the XANES spectra (**Figure 7-10**). A second treatment under reaction conditions of the oxide nitride with 1.0 wt% N could not be carried out due to insufficient beam time. The relative Mo K edge position of $(MoV)_5O_{14}$ did not change significant during treatment under reaction conditions. A slight increase of relative Mo K edge position of oxide nitrides was observed during first treatment under reaction conditions.

Conversely, previous studies of MoO_3 and MoO_3-type oxide nitrides shared that the final relative Mo K edge position was lower than the position of the oxide. The evolution of relative Mo K edge position of non-milled MoO_3 and its corresponding oxide nitride is shown in **Figure A 4-2**. An additional difference between both model systems was the behavior during second treatment under reaction conditions. Relative Mo K edge position of MoO_3-type oxide nitrides was similar to that of MoO_3 while position of Mo_5O_{14}-type oxide nitride was similar to that of first treatment under reaction conditions. Subsequently, *in situ* XAS experiments revealed an improved stability of (MoV) oxide nitrides during treatment under reaction conditions.

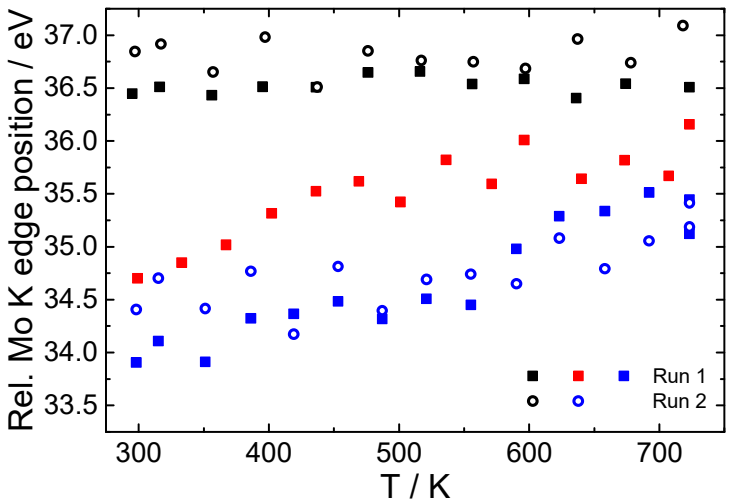

Figure 7-10: *Evolution of Mo K edge shift during treatment in 5% propene, 5% oxygen in helium up to 723 K.*

A refinement of XAS model of averaged distances to the experimental $FT(\chi(k)\cdot k^3)$ after first and second treatment under reaction conditions was carried out. The same refinement procedure as explained in **chap. 6.4.2** was used. In agreement to refinements of Mo_5O_{14} structure model to samples as prepared, only the disorder parameter σ^2 showed significant differences (**Figure 7-11**). Disorder parameters of shortest Mo-O distance of all samples decreased during first treatment under reaction conditions. Significant differences of σ^2 of $(MoV)_5O_{14}$ and its oxide nitrides were observed after treatment. On the contrary, σ^2 of the second Mo-O distance increased after the first treatment under reaction conditions. In addition, the increase of σ^2 of oxide nitrides was more distinct. The evolution of σ^2 after first treatment under reaction conditions

depended on the nitrogen content of the samples. During second the treatment under reaction conditions the disorder parameter remained constant. The dependences of σ^2 on nitrogen content might be due a partial removal of nitrogen. Analysis of spectra measured at room temperature confirmed results of *in situ* XAS data. Analysis of relative Mo K edge position revealed remaining structural defects after treatment under reaction conditions depending on nitrogen content. Additionally, *in situ* XRD experiments resulted in an increased lattice strain of Mo_5O_{14}-type oxide nitride after treatment under reactions conditions. Hence, these results were confirmed. Short Mo-O distance mainly represented distances in a/b plane as discussed in **chap. 6.4.2**. Similar disorder parameter of first Mo-O distance after treatment under reaction conditions were in good agreement with similar evolution of lattice parameter *a* during second treatment under reaction conditions.

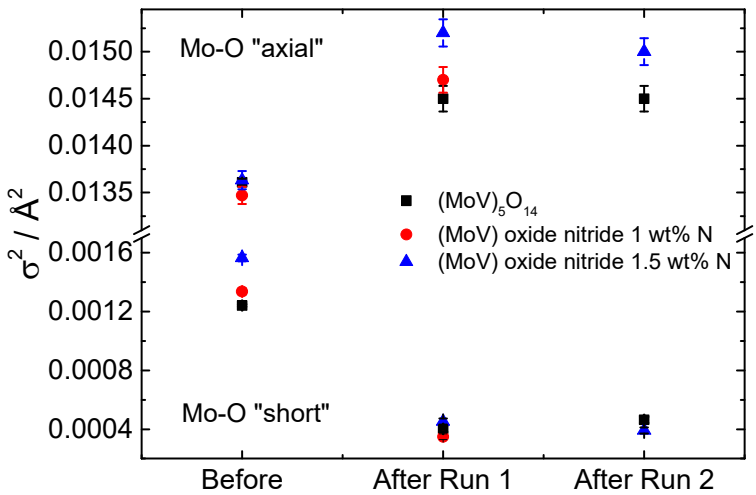

Figure 7-11: *XAFS disorder parameter σ^2 of two independent Mo-O distances before, after first and after final treatment in 5% propene, 5% oxygen in helium.*

7.5 Catalytic performance in selective propene oxidation

Catalytic performance in selective propene oxidation was investigated at 648 K, 673 K and 698 K. **Figure 7-12** shows the evolution of ion currents *(m/e* 17, 18, 28) during heating of Mo_5O_{14}-type oxide nitride with 1.5 wt% nitrogen in helium before catalytic testing. A peak of *m/e* 17 and *m/e* 18 at about 415 K could be associated with removal of water. A second peak of *m/e* 17 was detected at about 500 K. This peak corresponded to the

removal of NH_X groups. At temperatures higher than 600 K the removal of water and nitrogen was detected. Catalytic performance was investigated at various progressions of nitrogen removal. Compared to measurements at 648 K the amount of removed nitrogen at 698 K was increased by a factor of 2.5.

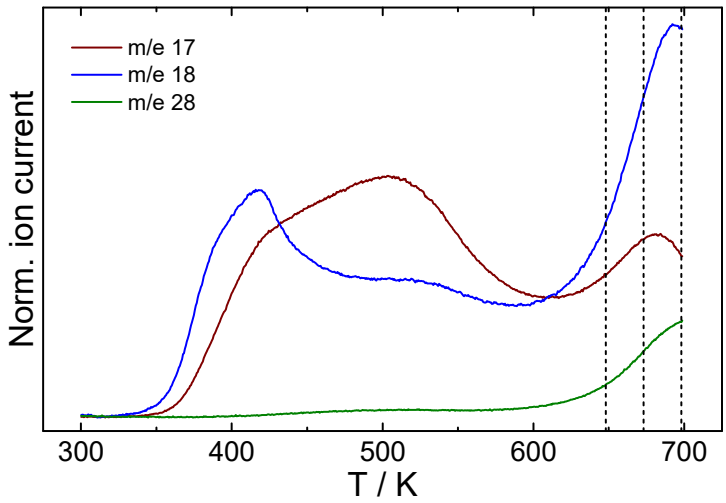

Figure 7-12: *Evolution of normalized ion current m/e 28 during heating up to 698 K in helium before treatment under reaction conditions. Temperatures of catalytic investigations are marked (dashes).*

Determining reaction rates and selectivities was carried out for each sample at different temperatures and similar propene conversions as well as similar time on stream. Reaction rates for propene conversion and acrolein formation at the various temperatures are shown in **Figure 7-13**. Propene conversion and acrolein formation exhibited a similar evolution after nitrogen substitution. Only the rates of the oxide nitride with the highest nitrogen content were slightly increased at 698 K.

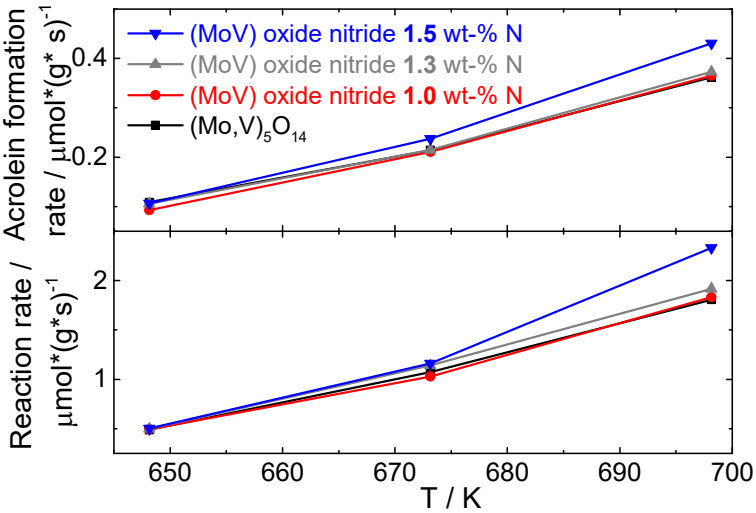

Figure 7-13: *Reaction rates for propene conversion (bottom) and acrolein formation (top) based on catalyst's initial weight at 648 K, 673 K and 698 K in 5 % propene and 5 % oxygen.*

Selectivities towards acrolein increased with higher nitrogen contents of the samples (**Figure 7-14**). Selectivities towards acrolein increased with higher nitrogen contents of the samples at every temperature. The increase of selectivity for the oxide nitride with 1.0 wt% nitrogen was independent of temperature. Selectivities of oxide nitrides with 1.3 and 1.5 wt% nitrogen were dependent on temperature. The change of selectivity with increasing nitrogen content was more distinct at low temperatures. At 698 K the increase of selectivity can be described by a linear regression over the whole range of nitrogen contents. FTIR measurements indicated the formation of N-H bonds in the samples with 1.3 and 1.5 wt%. Hence, the formation of N-H groups might cause an additional effect on selectivity. Elemental analysis of samples treated at 698 K yielded the remaining nitrogen content of the samples (0.25 wt%). The temperature dependence of selectivities of oxide nitrides with 1.3 and 1.5 wt% nitrogen might be due to the partial removal of nitrogen. XRD analysis of these samples showed that the Mo_5O_{14} structure was preserved during treatment under reaction conditions. This was corroborated by *in situ* XRD and XAS experiments (**Chap. 7.4**).

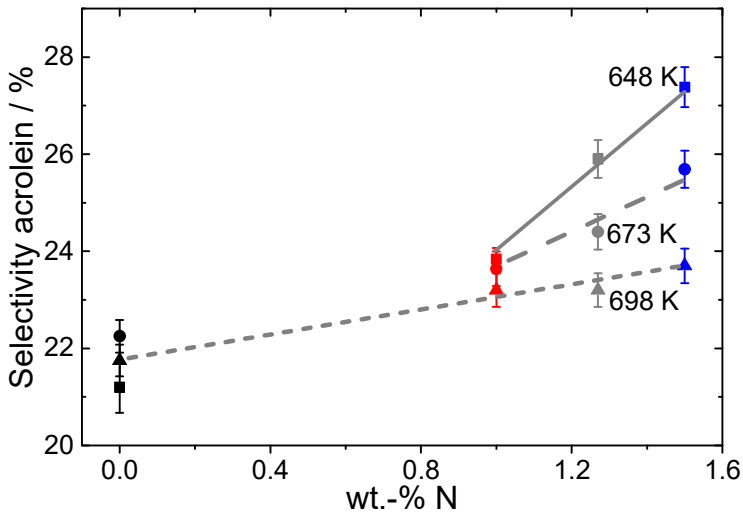

Figure 7-14: *Dependency of selectivity towards acrolein on nitrogen contents at 648 K, 673 K and 698 K in 5 % propene and 5 % oxygen.*

Compared to the evolution of selectivity towards acrolein the formation of total oxidation products showed an opposing trend (**Figure 7-15**). Selectivities towards CO_X were increased with increasing temperature. A higher nitrogen content of the samples led to a decreasing formation of CO_X. The ratio of $CO:CO_2$ remained about 1.5 for all samples. Similar to the evolution of selectivities towards acrolein, a more distinct change in selectivities was observed for the samples with 1.3 and 1.5 wt% nitrogen. In contrast to formation of acrolein, the evolution of CO_X formation with nitrogen contents remained at higher temperatures.

Lattice NH_X groups of oxide nitrides might also lead to the formation of nitriles by ammoxidation of propene [178]. The major product of selective ammoxidation of propene is acrylonitrile. Acetonitrile and propane nitrile represent the most prominent by-products in selective ammoxidation of propene [6]. Catalytic performance was investigated after different progressions of nitrogen removal. Formation of ammoxidation products could not be detected by gas chromatography. Hence, it can be assumed that NH_X groups were removed during heating in helium. Incorporated nitrogen ions, compensated by formation of oxygen vacancies, showed a higher thermal stability. Although a partial removal of these nitrogen ions during treatment under reaction conditions can occur, this removal was not associated with formation of ammoxidation products.

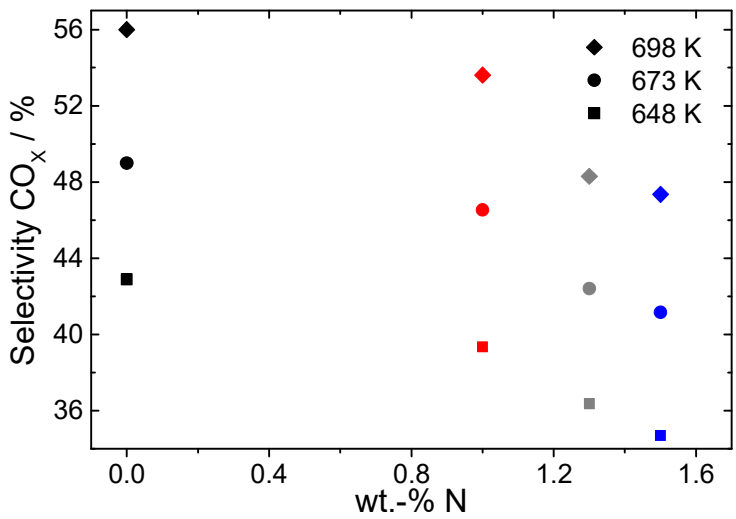

Figure 7-15: *Dependency of selectivity towards CO_X on nitrogen contents at 648 K, 673 K and 698 K in 5 % propene and 5 % oxygen.*

7.6 Correlation of conductivity and selectivity

Characterization of $(Mo,V)_5O_{14}$ and corresponding oxide nitrides showed a significant dependence of conductivity and selectivity on the nitrogen content in the samples. **Figure 7-16** shows the selectivity towards acrolein and CO_x as a function of conductivity at 648 K. Selectivity towards acrolein increased linearly with increasing conductivity. As discussed above conductivity represented a measure of availability of lattice oxygen. Consequently, increasing oxygen mobility led to an increased selectivity towards acrolein and a decreased formation of CO_X. According to the redox mechanism nucleophilic lattice oxygen of the bulk is inserted in the allylic species to form acrolein. Conversely, electrophilic species form total oxidation products [179]. According to Grasselli the resulting anion vacancy migrates to another site and is replaced by adjacent lattice oxygen [33]. Gaseous oxygen is adsorbed at another site on the surface and replenishes the anion vacancies [36]:

$$O_{2,ads} + e^- \rightleftharpoons O_2^- + e^- \rightleftharpoons O_2^{2-} \rightleftharpoons 2O^- + 2e^- \rightleftharpoons 2O^{2-}$$

The required electrons are transported in the bulk sample. Hence, investigations of conductivities revealed an increased electron transport in the bulk sample making electrons readily available to form nucleophilic lattice oxygen O^{2-}.

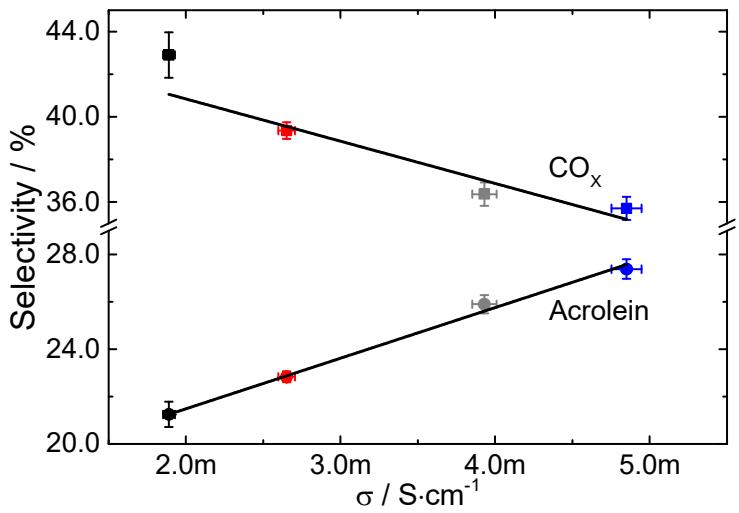

Figure 7-16: *Selectivity towards acrolein and CO_x as a function of conductivities indicating the oxygen availability at 648 K.*

7.7 Comparison to supported catalysts

Investigations on transition metal oxides supported on an inert support material represent a widely used approach in research of heterogeneous catalysts in selective oxidation reactions. Supported and highly dispersed metal oxides allow investigations on local structural motifs without considering bulk oxide properties. Several examples from the literature show that these supported transition metal oxides are also active in selective propene oxidation [180,181]. Hence, migration of anion vacancy in the bulk may not be mandatory for catalytic activity. However, the re-oxidation of supported catalysts is also associated with a transfer of electrons to adsorbed oxygen species on M-O-M units. Isolated monomeric species on support material showed very low catalytic activity [182]. Recent studies of supported vanadium oxides confirmed the assumption that at least two [VO_4] units are involved in selective oxidation of propene. A higher degree of oligomerization resulted in formation of V_xO_y nanocrystallites leading to a decreasing acrolein TOF. The influence of metal loading on catalytic performance was also investigated for supported molybdenum oxide in different selective oxidation reactions [183,184]. These types of reactions occurred by a redox mechanism including electron transfer for re-oxidation. Selectivity to respective products increased with increasing MoO_X surface density associated with an oligomerization of monomolybdate

species [184]. However, the role of electron transport in these supported catalysts is difficult to access because conductivity represent a bulk characteristic. Consequently, the influence of conductivity can best be investigated using bulk model systems. In this work, the correlation between oxygen mobility and selectivity towards acrolein could be shown for the first time without changing the crystal structure or chemical composition of the catalyst.

7.8 Summary

Reducibility of $(MoV)_5O_{14}$ and its corresponding oxide nitrides was studied by TPR with hydrogen and propene. Substitution of oxygen ions led to an improved reducibility which can be attributed to an increased availability of lattice oxygen. Combining results of *in situ* XANES spectra with mass spectrometry of product gases resulted in a correlation between reducibility, nitrogen content, and removal of nitrogen. In addition, thermal stability of Mo_5O_{14}-type oxide nitrides was enhanced compared to MoO_3-type oxide nitrides. Structural characterization of treated samples under reaction conditions revealed significant differences. The differences of disorder parameters of $(MoV)_5O_{14}$ and Mo_5O_{14}-type oxide nitrides decreased during treatment under reaction conditions. This decrease correlated to a partial removal of nitrogen. Remaining nitrogen content could be detected by different analytic methods despite two successive treatments under reaction conditions up to 698 K. Ammonolysis led to a weakening of metal-oxygen bond strength as well as increased bulk conductivity. Moreover, the resulting enhanced conductivity correlated with an increased selectivity towards acrolein in selective oxidation of propene. The formation of total oxidation products CO_X showed the opposite evolution as a function of conductivity. The enhanced conductivity was assigned to an improved electron transport in the bulk sample which might be essential for re-oxidation of the catalyst. Hence, the availability of nucleophilic oxygen species was improved. These results might also explain the known correlation between catalytic performance of supported transition metal oxides and transition metal oxide surface coverage. Apparently, Mo_5O_{14}-type oxide nitrides represent a suitable model system for studying correlations between conductivity, oxygen availability, and catalytic performance.

8 Conclusion

8.1 Introduction

Elucidating structure-activity relationships is an important issue in fundamental research on heterogeneous catalysts. Structure and chemical composition of industrial catalysts are often very complex. Therefore, investigations on simplified model catalysts are often carried out. Such investigations allow characterizing the influence of individual properties on catalytic performance. With the help of these relationships, the important factors for catalytic performance can be determined. Hence, determining these factors for activity and selectivity can result in a rational design of improved catalysts. Recent studies showed the suitability of MoO_3-type oxide nitrides as model catalysts for studying the influence of oxygen mobility on catalytic performance. The objective of this work was preparing and characterizing more active and stable molybdenum-based oxide nitrides. Therefore, the crystallinity of MoO_3 was modified by mechanical activation in a planetary mill. Ammonolysis of a set of ball-milled MoO_3 samples resulted in MoO_3-type oxide nitrides with various crystallinity. The results of *ex situ* and *in situ* structural characterization revealed a correlation between MoO_3-structure and thermal stability of oxide nitrides. However, MoO_3-type oxide nitride showed a low thermal stability under reaction conditions. Subsequently, the range of oxide nitrides was extended to more relevant catalysts for propene oxidation. Hence, mixed molybdenum oxide nitrides with Mo_5O_{14}-structure were prepared and characterized in detail by XRD, XAS, FTIR and impedance spectroscopy. The thermal stability of Mo_5O_{14}-type oxide nitrides was investigated using complementary *in* situ analytical methods. Furthermore, the effects of substitution of oxygen ions by nitrogen ions on catalytic performance in selective oxidation of propene were studied. These results were correlated to various structural and electrical properties.

8.2 Incorporation of nitrogen in molybdenum-based oxide nitrides

Modification of the anion lattice of MoO_3 and $(MoV)_5O_{14}$ by incorporation of nitrogen was studied in this work. The respective crystallographic structures were preserved during ammonolysis. The MoO_3-structure consists of layers of corner- and edge-sharing MoO_6 octahedrons. Oxygen ions next to the interlayer space were mainly substituted by nitrogen ions. After decomposition of NH_3 nitrogen ions can be incorporated.

FTIR spectra of MoO_3-type oxide nitrides showed strong N-H stretching and bending vibration modes. These vibration modes indicated the incorporation of NH_X species. Mechanical activation of MoO_3 resulted in an improved accessibility for hydrogen atoms. This was shown by an increased formation of OH groups or molybdenum hydrates. These OH groups can react with incorporated nitrogen ions to NH_X species (**eq. (8-2)**). Additionally, the formation of NH_X species could also occur when nitrogen ions were incorporated in MoO_3 (**eq. (8-3)**). The incorporation of NH_X species occurred without formation of oxygen vacancies according to following Kröger-Vink notation.

$$2NH_3(g) + 3O_O^X = 2N_O' + V_O^{\cdot\cdot} + 3H_2O \tag{8-1}$$

$$N_O' + OH_O^{\cdot} = NH_O^X + O_O^X \tag{8-2}$$

$$2NH_3(g) + 2O_O^X = NH_O^X + 2H_2O \tag{8-3}$$

The successful substitution of oxygen ions by nitrogen ions in $(MoV)_5O_{14}$ was shown by detection of Mo-N vibration modes in the FTIR spectra of Mo_5O_{14}-type oxide nitrides. The formation of oxygen vacancies mainly compensated the additional negative charge of nitrogen ions compared to oxygen ions. The oxidation of Mo and V centers for charge compensation was excluded by determining the average valences of Mo and V by XAS measurements. Only the samples with higher nitrogen contents showed an additional formation of $(NH)^{2-}$. The formation of NH_X species was significantly lowered compared to MoO_3-type oxide nitrides. FTIR spectra and elemental analysis of $(MoV)_5O_{14}$

and Mo_5O_{14}-type oxide nitrides showed the absence of OH groups. Hence, a reaction of nitrogen ions and OH groups according to **eq. (8-2)** could not occur.

8.3 Structure-function relationships of MoO_3-type oxide nitrides with various crystallinity

The crystallinity of MoO_3 and its corresponding oxide nitrides was successfully modified by ball-milling in a planetary mill. Size-strain analysis of XRD powder patterns was carried out by single-line analysis and Fourier analysis. Ball-milling of MoO_3 resulted in a decrease in crystallite sizes as calculated from different diffraction peaks. Subsequent ammonolysis led to an incorporation of nitrogen associated with an increase of lattice strain.

According to the redox mechanism, the ease of extraction of lattice oxygen is expected to play an important role for catalytic performance in selective oxidation of propene. The ease of extraction of lattice oxygen from a catalyst can be investigated by studies on the reducibility of the catalyst. Recent studies showed that the reducibility was significantly varied by modification of the anion lattice. The reducibility of MoO_3 with varying crystallinity and its corresponding oxide nitrides was investigated during isothermal and non-isothermal reduction with hydrogen and propene. Analysis of solid-state kinetics during isothermal reduction revealed that the rate-determining step was well described by R2-model. R2 model simplifies the particle shape to a cylinder. A rapid nucleation on the surface of the crystal was assumed. Decreasing the crystallite size as well as modifying the anion lattice of MoO_3 resulted in a significant enhanced reducibility. In addition, the apparent activation energies of the rate-determining step for the reduction of MoO_3 to MoO_2 were calculated from analysis of solid-state kinetics. A correlation between crystallize size and apparent activation energy was shown. Ball-milling of MoO_3 led to a decrease in apparent activation energies. This dependence of reducibility on crystallite size was preserved after ammonolysis. Incorporation of nitrogen ions caused an additional decrease of apparent activation energies.

Catalytic performance of MoO_3 and MoO_3-type oxide nitrides with various crystallinity was tested. A decrease in crystallite size led to significantly increased reaction

rates for propene conversion and acrolein formation. The incorporation of nitrogen led to slightly increased reaction rate for propene conversion at the beginning of the catalytic testing. However, this increase was not long-time stable because of the lower thermal stability of MoO_3-type oxide nitrides. Otherwise, the product distribution was significantly affected by varying crystallinity and modifying the anion lattice. MoO_3-type oxide nitrides showed an increased formation of acrolein while formation of CO_X was decreased. In addition, the insertion of oxygen in C_2-position of propene was diminished resulting in a decreased formation of acetone and acetic acid.

8.4 Thermal stability of molybdenum-based oxide nitrides

Incorporation of nitrogen in MoO_3 resulted in significant coloration of the samples due to formation of structural defects. Hence, *in situ* DR-UV-Vis spectroscopy represented a suitable method to investigate the thermal stability of MoO_3-type oxide nitrides under reaction conditions. Absorption in the low energy range increased significantly after incorporation of nitrogen. A decrease at the same energy during thermal treatment was correlated to the removal of nitrogen. Destruction of defects was associated with the removal of nitrogen and was detected by *in situ* DR-UV-Vis spectroscopy. The onset of nitrogen removal decreased with increasing milling-time. A correlation between increased thermal stability of MoO_3-type oxide nitrides and increased crystallite size calculated from the (020) and (040) diffraction peaks was elucidated. The calculated crystallite sizes corresponded to the length of interlayer space in the MoO_3-structure. Consequently, the mechanical activation of MoO_3 led to a decrease in thermal stability of MoO_3-type oxide nitrides. The range of molybdenum-based oxide nitrides was extended to Mo_5O_{14}-type oxide nitrides. Mo_5O_{14}-structure represents an important structural motive for heterogeneous catalysts. Recent studies showed that catalysts with Mo_5O_{14}-structure are active in various selective oxidation reactions. It was proposed that Mo_5O_{14}-type oxides represent the major component of highly active MoVW catalysts. This component is expected to provide high electronic conductivity. V-stabilized Mo_5O_{14}-structure is known to be active in selective oxidation of propene. $(MoV)_5O_{14}$ crystallized in a non-layered structure.

Thermal stability of Mo_5O_{14}-type oxide nitrides under catalytic conditions was investigated by *in situ* XRD and XAS. XRD lattice strain and XAFS disorder parameter of Mo_5O_{14}-type oxide nitrides revealed a decrease in structural disorder during first treatment under reaction conditions. Structural disorder was invariant during second successive treatment under reaction conditions. Compared to $(MoV)_5O_{14}$ significant differences of structural disorder of Mo_5O_{14}-type oxide nitrides were preserved after treatment under reaction conditions. These differences might be correlated to a partial removal of nitrogen. An elemental analysis of samples treated at 698 K yielded a remaining nitrogen content of the samples (0.25 wt%).

8.5 Correlations between conductivity and catalytic activity of Mo_5O_{14}-type oxide nitrides

A detailed structural and functional characterization of Mo_5O_{14}-type oxide nitrides was carried out to obtain structure-function correlations. Molybdenum-based oxide nitrides represent suitable model system for studying correlations between conductivity, oxygen availability, and catalytic performance.

Figure 8-1 summarizes all correlations between results of structural and functional characterization. The substitution of oxygen ions by nitrogen ions led to an increased conductivity. The increase of conductivity was dependent on the degree of substitution. The increased conductivity was correlated to the increased reducibility observed in TPR experiments. This behavior could be associated with increasing oxygen availability. The incorporation of nitrogen ions resulted in an increased structural disorder while preserving the Mo_5O_{14}-structure. XRD as well as XAS revealed complementary results by analyzing lattice strain ε (XRD) and XAFS disorder parameter σ^2. Furthermore, the enhanced conductivity correlated with an increased selectivity towards acrolein and a decreased selectivity towards total oxidation products CO_X. Subsequently, the increased formation of acrolein was related to increased electron transfer and oxygen availability.

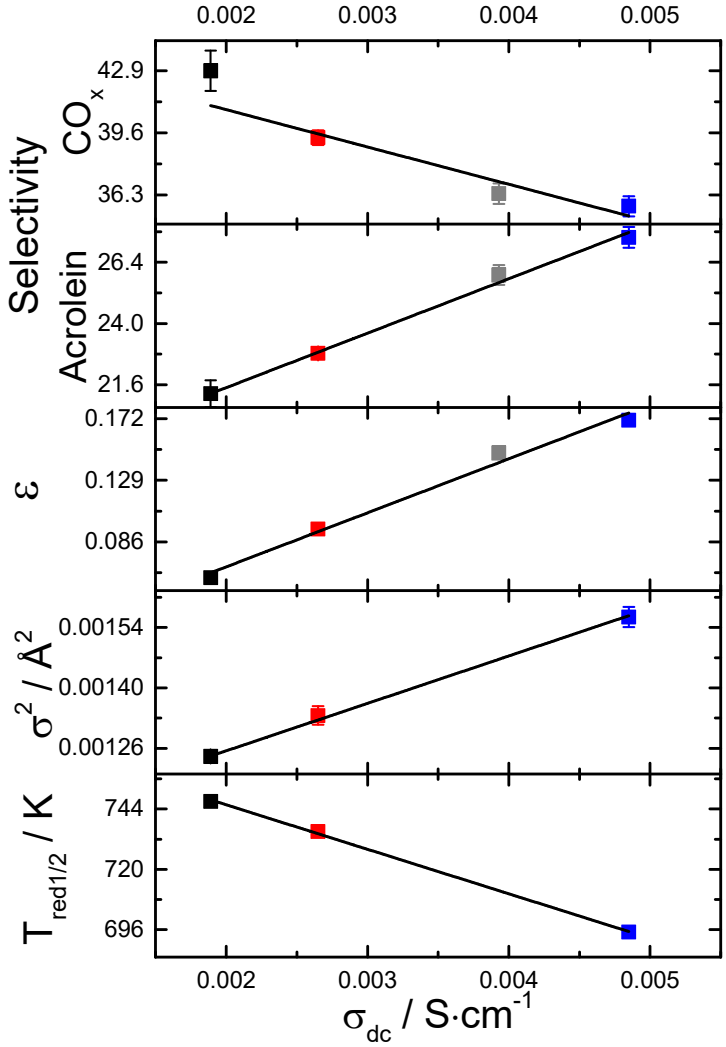

Figure 8-1: *Correlations between conductivity and results of structural and functional characterization.*

Selectivity in propene oxidation is affected by the availability of different oxygen species. According to the "Mars-van-Krevelen"-mechanism nucleophilic lattice oxygen O^{2-} and electrophilic oxygen species O^{-} participate in the catalytic cycles (**Figure 8-2**, top). Reaction of propene with nucleophilic lattice oxygen results in the formation of acrolein and water. From a defect chemistry point of view, oxygen vacancies and mobile electrons are formed (**eq. (8-4)**). The metal centers of the catalyst are partial reduced by the formed electrons (**eq. (8-5)**).

$$C_3H_6 + 2O_O^X \rightarrow C_3H_4O + H_2O + 2V_O^{\cdot\cdot} + 4e' \quad (8\text{-}4)$$

$$M^{n+} + xe' \rightarrow M^{(n-x)+} \quad (8\text{-}5)$$

Conversely, CO_X is formed by conversion of propene with electrophilic oxygen species. These electrophilic oxygen species represent intermediates in transferring gas-phase oxygen into lattice oxygen ions of the bulk catalyst (**eq. (8-6)**). The required four electrons are given by the solid. The re-oxidation of the catalyst can occur at a different reactive site of the catalyst.

$$O_{2,ads} + e^- \rightleftharpoons O_2^- + e^- \rightleftharpoons O_2^{2-} \rightleftharpoons 2O^- + 2e^- \rightleftharpoons 2O^{2-} \quad (8\text{-}6)$$

Incorporation of nitrogen ions in the oxide catalyst led to formation of oxygen vacancies. (**Figure 8-2**, bottom). These processes significantly influenced the electric properties of the catalysts. Investigations on the influence of oxygen partial pressure on conductivity revealed that $(MoV)_5O_{14}$ and its corresponding oxide nitrides are p-type semiconductors. P-type semiconductors are electron-deficient in the lattice and characterized by an excess of lattice oxygen. P-type mixed oxides conduct electrons by means of positive holes. Electronic p-type conductivity was increased after incorporation of nitrogen. Hence, electrons can be more easily transported in the bulk from the metal cations to re-oxidation site. Here, electrons might be more available to form nucleophilic lattice oxygen from adsorbed gas-phase oxygen. In contrast to n-type semiconductors, electrons can be more easily removed from metal cations. Hence, the adsorption and transformation of gas-phase oxygen might occur far more readily on this type of semiconductors.

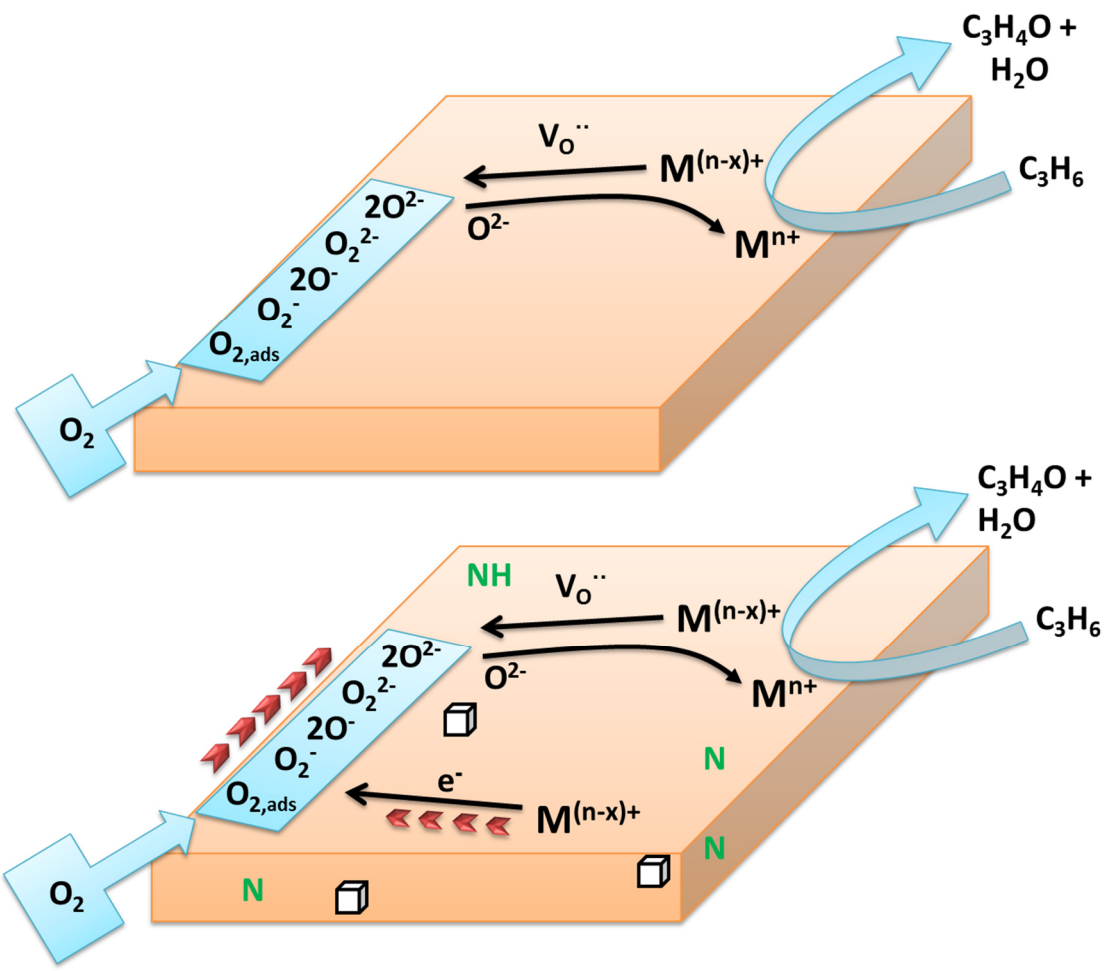

Figure 8-2: *Top: Schematic presentation of redox mechanism ("Mars-van-Krevelen") for selective oxidation of propene to acrolein (adapted from [3,33]). Bottom: Schematic representation of structural and functional changes after modification of anion lattice of molybdenum-based model catalysts by incorporation of nitrogen.*

9 References

[1] D. Saygin, E. Worrell, C. Tam, N. Trudeau, D. J. Gielen, M. Weiss, M. K. Patel, *Long-term energy efficiency analysis requires solid energy statistics: The case of the German basic chemical industry*, *Energy* **2012**, *44*, 1094–1106.

[2] F. Schüth, *Heterogene Katalyse: Schlüsseltechnologie der chemischen Industrie*, *Chemie in unserer Zeit* **2006**, *40*, 92–103.

[3] G. Centi, F. Cavani, F. Trifirò, *Selective Oxidation by Heterogeneous Catalysis*, Springer US; Imprint; Springer, Boston, MA, **2001**.

[4] H. W. Cui, S. M. Wen, T. T. Zhuang, F. C. Bai, L. Yu, *Poly Acrylic Acid Superabsorbent Hydrogel for Hygiene Materials*, *AMR* **2014**, *1002*, 7–10.

[5] U. S. Ozkan, R. B. Watson, *The structure–function relationships in selective oxidation reactions over metal oxides*, *Catal. Today* **2005**, *100*, 101–114.

[6] R. K. Grasselli, *Advances and future trends in selective oxidation and ammoxidation catalysis*, *Catal. Today* **1999**, *49*, 141–153.

[7] J. M. Thomas, *The Ineluctable Need for in Situ Methods of Characterising Solid Catalysts as a Prerequisite to Engineering Active Sites*, *Chem. Eur. J.* **1997**, *3*, 1557–1562.

[8] B. M. Weckhuysen, *Snapshots of a working catalyst: possibilities and limitations of in situ spectroscopy in the field of heterogeneous catalysis*, *Chem. Commun.* **2002**, 97–110.

[9] H. F. Rase, *Handbook of commercial catalysts*. *Heterogeneous catalysts*, CRC Press, Boca Raton, Fla., **2000**.

[10] G. Ertl, H. Knözinger, F. Schüth, J. Weitkamp (Eds.) *Handbook of heterogeneous catalysis*, Wiley-VCH, Weinheim, **2008**.

[11] J. Haber, E. Lalik, *Catalytic properties of MoO_3 revisited*, *Catal. Today* **1997**, *33*, 119–137.

[12] K. Schuh, W. Kleist, M. Høj, A. D. Jensen, P. Beato, G. R. Patzke, J.-D. Grunwaldt, *Systematic study on the influence of the morphology of α-MoO_3 in the selective oxidation of propylene*, *J. Solid State Chem.* **2015**, *228*, 42–52.

[13]R. K. Grasselli, J. D. Burrington, *Selective Oxidation and Ammoxidation of Propylene by Heterogeneous Catalysis* **1981**, *30*, 133–163.

[14]G. Mestl, C. Linsmeier, R. Gottschall, M. Dieterle, J. Find, D. Herein, J. Jäger, Y. Uchida, R. Schlögl, *Molybdenum oxide based partial oxidation catalyst: 1. Thermally induced oxygen deficiency, elemental and structural heterogeneity and the relation to catalytic performance*, *J. Mol. Catal. A: Chem.* **2000**, *162*, 463–492.

[15]Y. Moro-Oka, W. Ueda, K.-H. Lee, *The role of bulk oxide ion in the catalytic oxidation reaction over metal oxide catalyst*, *Journal of Molecular Catalysis A: Chemical* **2003**, *199*, 139–148.

[16]T. Ressler, J. Wienold, R. E. Jentoft, F. Girgsdies, *Evolution of Defects in the Bulk Structure of MoO_3 During the Catalytic Oxidation of Propene*, *Eur. J. Inorg. Chem.* **2003**, 301–312.

[17]P. Mars, D. W. van Krevelen, *Oxidations carried out by means of vanadium oxide catalysts*, *Chem. Eng. Sci.* **1954**, *3*, 41–59.

[18]G. W. Keulks, L. D. Krenzke, T. M. Notermann, *Selective Oxidation of Propylene*, *Adv. Catal.* **1979**, *27*, 183–225.

[19]T. Ono, K. Utsumi, S. Tsukamoto, H. Tamaru, M. Kataoka, F. Noguchi, *Roles of bulk γ(L)-Bi_2MoO_6 and surface β-$Bi_2Mo_2O_9$ in the selective catalytic oxidation of C_3H_6*, *J. Mol. Catal. A: Chem.* **2010**, *318*, 94–100.

[20]E. Rödel, O. Timpe, A. Trunschke, G. Zenkovets, G. Kryukova, R. Schlögl, T. Ressler, *Structure stabilizing effect of tungsten in mixed molybdenum oxides with Mo_5O_{14}-type structure*, *Catal. Today* **2007**, *126*, 112–118.

[21]B. Grzybowska-Świerkosz, *Thirty years in selective oxidation on oxides: what have we learned?*, *Top. Catal.* **2000**, *11/12*, 23–42.

[22]G. Andersson, A. Magnéli, L. G. Sillén, M. Rottenberg, *On the Crystal Structure of Molybdenum Trioxide*, *Acta Chem. Scand.* **1950**, *4*, 793–797.

[23]M. Dieterle, G. Weinberg, G. Mestl, *Raman spectroscopy of molybdenum oxides*, *Phys. Chem. Chem. Phys.* **2002**, *4*, 812–821.

[24]L. Kihlborg, *Crystal structure studies on Mo_5O_{14}, a compound exhibiting two-dimensional disorder.*, *Arkiv Kemi* **1963**, *21*, 427.

[25]N. Yamazoe, L. Kihlborg, *Mo_5O_{14} – twinning and three-dimensional structure, determined from a partly tantalum-substituted crystal*, *Acta Crystallogr B Struct Crystallogr Cryst Chem* **1975**, *31*, 1666–1672.

[26]T. Ekström, M. Nygren, D. Simov, H. A. Øye, S. Svensson, *Ternary Phases with the Mo_5O_{14} Type of Structure. I. A Study of the Molybdenum-Vanadium-Oxygen System*, *Acta Chem. Scand.* **1972**, *26*, 1827–1835.

[27]L. Kihlborg, B. Dahlén, H. M. Seip, T. Holme, A. A. Lindberg, G. Jansen, B. Lamm, B. Samuelsson, *Stabilization of the Tunnel Structure of Mo_5O_{14} by Partial Metal Atom Substitution*, *Acta Chem. Scand.* **1969**, *23*, 1834–1835.

[28]T. Ekström, M. Nygren, D. Simov, H. A. Øye, S. Svensson, *Ternary Phases with the Mo_5O_{14} Type of Structure. II. A Study of the Molybdenum-Niobium-Oxygen and Molybdenum-Tantalum-Oxygen Systems*, *Acta Chem. Scand.* **1972**, *26*, 1836–1842.

[29]T. Ekström, M. Nygren, D. Simov, H. A. Øye, S. Svensson, *Ternary Phases with the Mo_5O_{14} Type of Structure. III. A Phase Analysis of the Molybdenum-Titanium-Oxygen System*, *Acta Chem. Scand.* **1972**, *26*, 1843–1846.

[30]E. Rödel, *In situ bulk structural investigations of Mo_5O_{14}-type mixed metal oxide catalysts for partial oxidation reactions*, Dissertation, TU Berlin, Berlin, **2006**.

[31]P. Beato, A. Blume, F. Girgsdies, R. E. Jentoft, R. Schlögl, O. Timpe, A. Trunschke, G. Weinberg, Q. Basher, F. A. Hamid et al., *Analysis of structural transformations during the synthesis of a MoVTeNb mixed oxide catalyst*, *Appl. Catal., A* **2006**, *307*, 137–147.

[32]E. V. Ishchenko, T. V. Andrushkevich, G. Popova, T. Kardash, A. V. Ishchenko, L. S. Dovlitova, Y. Chesalov, *The structure and catalytic properties of amorphous phase in MoVTeO catalysts for propane ammoxidation*, *Appl. Catal., A* **2014**, *476*, 91–102.

[33]R. K. Grasselli, *Fundamental Principles of Selective Heterogeneous Oxidation Catalysis*, *Top. Catal.* **2002**, *21*, 79–88.

[34]A. Guerrero-Ruiz, I. Rodriguez-Ramos, P. Ferreira-Aparicio, M. Abon, J. C. Volta, *Description of active sites on molybdenum oxide as detected by isotope exchange between $C^{18}O_2$ and $Mo^{16}O_3$*, *Catal. Today* **1996**, *32*, 223–227.

[35]T. Ressler, *Bulk Structural Investigation of the Reduction of MoO_3 with Propene and the Oxidation of MoO_2 with Oxygen*, *J. Catal.* **2002**, *210*, 67–83.

[36]E. Bordes, *The role of structural chemistry of selective catalysts in heterogeneous mild oxidation catalysis of hydrocarbons*, *C. R. Acad. Sci., Ser. IIc: Chim.* **2000**, *3*, 725–733.

[37]J. Haber, *The Concept of Structure-Sensitivity in Catalysis by Oxides* **1989**, *48*, 447–467.

[38]J. C. Védrine, *Revisiting active sites in heterogeneous catalysis: Their structure and their dynamic behaviour*, *Appl. Catal., A* **2014**, *474*, 40–50.

[39]B. Grzybowska-Świerkosz, *Effect of Additives on the Physicochemical and Catalytic Properties of Oxide Catalysts in Selective Oxidation Reactions*, *Top. Catal.* **2002**, *21*, 35–46.

[40]M. O. Guerrero-Pérez, M. A. Bañares, *Niobium as promoting agent for selective oxidation reactions*, *Catal. Today* **2009**, *142*, 245–251.

[41]X. Li, J. Zhao, W. Ji, Z. Zhang, Y. Chen, C. Au, S. Han, H. Hibst, *Effect of vanadium substitution in the cesium salts of Keggin-type heteropolyacids on propane partial oxidation*, *J. Catal.* **2006**, *237*, 58–66.

[42]M. Lerch, J. Janek, K. D. Becker, S. Berendts, H. Boysen, T. Bredow, R. Dronskowski, S. G. Ebbinghaus, M. Kilo, M. W. Lumey et al., *Oxide nitrides: From oxides to solids with mobile nitrogen ions*, *Prog. Solid State Chem.* **2009**, *37*, 81–131.

[43]H. Soerijanto, C. Rodel, U. Wild, M. Lerch, R. Schomäcker, R. Schlögl, T. Ressler, *The impact of nitrogen mobility on the activity of zirconium oxynitride catalysts for ammonia decomposition*, *J. Catal.* **2007**, *250*, 19–24.

[44]J. L. Gole, J. D. Stout, C. Burda, Y. Lou, X. Chen, *Highly Efficient Formation of Visible Light Tunable $TiO_{2-x}N_x$ Photocatalysts and Their Transformation at the Nanoscale*, *J. Phys. Chem. B* **2004**, *108*, 1230–1240.

[45]F. Tessier, P. Maillard, F. Cheviré, K. Domen, S. Kikkawa, *Optical properties of oxynitride powders*, *J. Ceram. Soc. Japan* **2009**, *117*, 1–5.

[46]G. Sierra Gallego, N. Marín Alzate, O. Arnache, *A novel $LaFeO_{3-X}N_X$ oxynitride. Synthesis and characterization*, *J. Alloys Compd.* **2013**, *549*, 163–169.

[47]S. Berendts, M. Huber, M. Weiß, M. Lehmann, T. Ressler, M. Lerch, *Synthese, Charakterisierung und Reaktivität von Molybdänoxidnitriden*, *Z. anorg. allg. Chem.* **2008**, *634*, 2029.

[48]S. Kühn, P. Schmidt-Zhang, A. H. P. Hahn, M. Huber, M. Lerch, T. Ressler, *Structure and properties of molybdenum oxide nitrides as model systems for selective oxidation catalysts*, *Chem. Cent. J.* **2011**, *5*, 42.

[49]X.-J. Wang, R. Nesper, C. Villevieille, P. Novák, *Ammonolyzed MoO_3 Nanobelts as Novel Cathode Material of Rechargeable Li-Ion Batteries*, *Adv. Energy Mater.* **2013**, *3*, 606–614.

[50]W. Ji, R. Shen, R. Yang, G. Yu, X. Guo, L. Peng, W. Ding, *Partially nitrided molybdenum trioxide with promoted performance as an anode material for lithium-ion batteries*, *J. Mater. Chem. A* **2014**, *2*, 699–704.

[51]R. E. Dinnebier, Billinge, S. J. L, *Powder diffraction*. *Theory and practice*, Royal Society of Chemistry, Cambridge, **2008**.

[52]G. Perego, *Characterization of heterogeneous catalysts by X-ray diffraction techniques*, *Catal. Today* **1998**, *41*, 251–259.

[53]L. Spiess, *Moderne Röntgenbeugung*. *Röntgendiffraktometrie für Materialwissenschaftler, Physiker und Chemiker*, Teubner, Wiesbaden, **2005**.

[54]S. R. Bare, T. Ressler, *Characterization of Catalysts in Reactive Atmospheres by X-ray Absorption Spectroscopy* **2009**, *52*, 339–465.

[55]D. C. Koningsberger, R. Prins, *X-ray absorption*. *Principles, applications, techniques of EXAFS, SEXAFS, and XANES*, Wiley, New York, **1988**.

[56]J. F. Haw, *In-situ spectroscopy in heterogeneous catalysis*, Wiley-VCH, Weinheim, **2002**.

[57]J. W. Niemantsverdriet, *Spectroscopy in catalysis*. *An introduction*, Wiley-VCH; [John Wiley, distributor], Weinheim, [Chichester], **2007**.

[58]D. E. Sayers, E. A. Stern, F. W. Lytle, *New Technique for Investigating Noncrystalline Structures: Fourier Analysis of the Extended X-Ray—Absorption Fine Structure*, *Phys. Rev. Lett.* **1971**, *27*, 1204–1207.

[59]J. Yano, V. K. Yachandra, *X-ray absorption spectroscopy*, *Photosynthesis research* **2009**, *102*, 241–254.

[60]D. D. Macdonald, *Reflections on the history of electrochemical impedance spectroscopy*, *Electrochimica Acta* **2006**, *51*, 1376–1388.

[61]A. Ovenston, *AC Electrical Characterization of Heterogeneous Catalysts*, *J. Catal.* **1993**, *140*, 464–480.

[62]E. Barsoukov, J. R. Macdonald, *Impedance spectroscopy*. *Theory, experiment, and applications*, John Wiley & Sons, Hoboken, N.J., **2005**.

[63]M. E. Orazem, B. Tribollet, *Electrochemical impedance spectroscopy*, Wiley, Hoboken, N.J., **2008**.

[64]B. M. Weckhuysen, R. A. Schoonheydt, *Recent progress in diffuse reflectance spectroscopy of supported metal oxide catalysts*, *Catal. Today* **1999**, *49*, 441–451.

[65]G. Kortüm, *Reflexionsspektroskopie; Grundlagen, Methodik, Anwendungen*, Springer-Verlag, Berlin, New York, **1969**.

[66]G. Kubelka, F. Munk, *An article on optics of paint layers*, *Zeitschrift für technische Physik* **1931**, *12*, 593–601.

[67]F. M. Mirabella, *Modern techniques in applied molecular spectroscopy*, Wiley, New York, **1998**.

[68]J. Hagen, *Industrial catalysis*. *A practical approach*, Wiley-VCH, Weinheim, **2006**.

[69]Haber, J., Block, J.H., and Delmon, B. in *Handbook of heterogeneous catalysis* (Eds.: G. Ertl, H. Knözinger, F. Schüth, J. Weitkamp), Wiley-VCH, Weinheim, **2008**.

[70]G. Schomburg, *Gas chromatography*. *A practical course*, VCH, Weinheim, New York, **1990**.

[71]K. Robards, P. R. Haddad, P. E. Jackson, *Principles and practice of modern chromatographic methods*, Academic Press, London, Boston, **1994**.

[72]C. H. Hartmann, *Gas chromatography detectors*, *Anal. Chem.* **1971**, *43*, 113A–125a.

[73]P. W. Atkins, J. d. Paula, *Physikalische Chemie*, Wiley-VCH, Weinheim, **2013**.

[74]M. Hesse, H. Meier, B. Zeeh, *Spektroskopische Methoden in der organischen Chemie*, Thieme, Stuttgart, New York, **2005**.

[75]D. A. Skoog, J. J. Leary, *Instrumentelle Analytik*. *Grundlagen, Geräte, Anwendungen*, Springer, Berlin, **1996**.

[76]P. Hahn-Weinheimer, A. Hirner, K. Weber-Diefenbach, *Röntgenfluoreszenzanalytische Methoden*, Springer Berlin Heidelberg, Berlin, Heidelberg, **1995**.

[77]K. Cammann, *Instrumentelle analytische Chemie*. *Verfahren, Anwendungen, Qualitätssicherung*, Spektrum Akad. Verl, Heidelberg, **2010**.

[78]Sing, K. S. W., *Reporting physisorption data for gas/solid systems with special reference to the determination of surface area and porosity (Recommendations 1984)*, *Pure and Applied Chemistry* **1985**, *57*.

[79]S. Brunauer, P. H. Emmett, E. Teller, *Adsorption of Gases in Multimolecular Layers*, *J. Am. Chem. Soc.* **1938**, *60*, 309–319.

[80]J. C. Volta, *Structure sensitivity of MoO3 in mild oxidation of propylene*, *J. Catal.* **1985**, *93*, 467–470.

[81]G. Mestl, B. Herzog, R. Schlögl, H. Knoezinger, *Mechanically Activated MoO_3. 1. Particle Size, Crystallinity, and Morphology*, *Langmuir* **1995**, *11*, 3027–3034.

[82]G. Mestl, N. F. D. Verbruggen, H. Knoezinger, *Mechanically Activated MoO_3. 2. Characterization of Defect Structures*, *Langmuir* **1995**, *11*, 3035–3041.

[83]G. Mestl, T. K. K. Srinivasan, H. Knoezinger, *Mechanically Activated MoO_3. 3. Characterization by Vibrational Spectroscopy*, *Langmuir* **1995**, *11*, 3795–3804.

[84]G. Mestl, N. F. D. Verbruggen, F. C. Lange, B. Tesche, H. Knözinger, *Mechanically Activated MoO_3. 4. In Situ Characterization of Physical Mixtures with Al_2O_3*, *Langmuir* **1996**, *12*, 1817–1829.

[85]J. M. Huber, *Oxidnitride als Katalysatoren zur Methanaktivierung*, Dissertation, TU Berlin, Berlin, **2011**.

[86]H. M. Rietveld, *A profile refinement method for nuclear and magnetic structures*, *J. Appl. Crystallogr.* **1969**, *2*, 65–71.

[87]J. Rodriguez-Carvajal, *FULLPROF: A Program for Rietveld Refinement and Pattern Matching Analysis.*, *Abstracts of the Satellite Meeting on Powder Diffraction of the XV Congress of the IUCr* **1990**, 127.

[88]T. Ressler, *WinXAS: a Program for X-ray Absorption Spectroscopy Data Analysis under MS-Windows*, *J. Synchrotron Radiat.* **1998**, *5*, 118–122.

[89]D. Balzar, H. Ledbetter, *Voigt-function modeling in Fourier analysis of size- and strain-broadened X-ray diffraction peaks*, *J. Appl. Crystallogr.* **1993**, *26*, 97–103.

[90]D. Balzar, *BREADTH – a program for analyzing diffraction line broadening*, *J. Appl. Crystallogr.* **1995**, *28*, 244–245.

[91]H. Sitepu, B. H. O'Connor, D. Li, *Comparative evaluation of the March and generalized spherical harmonic preferred orientation models using X-ray diffraction data for molybdite and calcite powders*, *J. Appl. Crystallogr.* **2005**, *38*, 158–167.

[92]L. W. Finger, D. E. Cox, A. P. Jephcoat, *A correction for powder diffraction peak asymmetry due to axial divergence*, *J. Appl. Crystallogr.* **1994**, *27*, 892–900.

[93]X. Sha, L. Chen, A. C. Cooper, G. P. Pez, H. Cheng, *Hydrogen Absorption and Diffusion in Bulk α-MoO_3*, *J. Phys. Chem. C* **2009**, *113*, 11399–11407.

[94]D. Logvinovich, R. Aguiar, R. Robert, M. Trottmann, S. Ebbinghaus, A. Reller, A. Weidenkaff, *Synthesis, Mo-valence state, thermal stability and thermoelectric properties of $SrMoO_{3-x}N_x$ (x>1) oxynitride perovskites*, *J. Solid State Chem.* **2007**, *180*, 2649–2654.

[95]Y.-I. Kim, P. M. Woodward, *Syntheses and characterizations of complex perovskite oxynitrides $LaMg_{1/3}Ta_{2/3}O_2N$, $LaMg_{1/2}Ta_{1/2}O_{5/2}N_{1/2}$, and $BaSc_{0.05}Ta_{0.95}O_{2.1}N_{0.9}$*, *J. Solid State Chem.* **2007**, *180*, 3224–3233.

[96]E. J. Mittemeijer, U. Welzel, *The "state of the art" of the diffraction analysis of crystallite size and lattice strain*, *Z. Kristallogr.* **2008**, *223*, 552–560.

[97]L. Q. Mai, B. Hu, W. Chen, Y. Y. Qi, C. S. Lao, R. S. Yang, Y. Dai, Z. L. Wang, *Lithiated MoO_3 Nanobelts with Greatly Improved Performance for Lithium Batteries*, *Adv. Mater.* **2007**, *19*, 3712–3716.

[98]F. Sánchez-Bajo, F. L. Cumbrera, *The Use of the Pseudo-Voigt Function in the Variance Method of X-ray Line-Broadening Analysis*, *J. Appl. Crystallogr.* **1997**, *30*, 427–430.

[99]T. Ida, M. Ando, H. Toraya, *Extended pseudo-Voigt function for approximating the Voigt profile*, *J Appl Crystallogr* **2000**, *33*, 1311–1316.

[100] T. H. de Keijser, E. J. Mittemeijer, H. C. F. Rozendaal, *The determination of crystallite-size and lattice-strain parameters in conjunction with the profile-refinement*

method for the determination of crystal structures, *J. Appl. Crystallogr.* **1983**, *16*, 309–316.

[101] C. E. Kril, R. Birringer, *Estimating grain-size distributions in nanocrystalline materials from X-ray diffraction profile analysis*, *Philos. Mag. A* **1998**, *77*, 621–640.

[102] L. Seguin, M. Figlarz, R. Cavagnat, J.-C. Lassègues, *Infrared and Raman spectra of MoO_3molybdenum trioxides and $MoO_3 \cdot xH_2O$ molybdenum trioxide hydrates*, *Spectrochim. Acta, Part A* **1995**, *51*, 1323–1344.

[103] M. A. Py, K. Maschke, *Intra- and interlayer contributions to the lattice vibrations in MoO_3*, *Physica B+C* **1981**, *105*, 370–374.

[104] D. Martin, D. Duprez, *Mobility of Surface Species on Oxides. 1. Isotopic Exchange of $^{18}O_2$ with ^{16}O of SiO_2, Al_2O_3 , ZrO_2 , MgO, CeO_2 , and CeO_2-Al_2O_3 . Activation by Noble Metals. Correlation with Oxide Basicity †*, *J. Phys. Chem.* **1996**, *100*, 9429–9438.

[105] G. Socrates, *Infrared and raman characteristic group frequencies*. *Tables and charts*, John Wiley & Sons, West Sussex, **2007**.

[106] N. Sotani, K. Eda, M. Sadamatu, S. Takagi, *Preparation and characterization of hydrogen molybdenum bronzes, H_xMoO_3*, *Bull. Chem. Soc. Jpn.* **1989**, *62*, 903–907.

[107] K. Eda, *Infrared spectra of hydrogen molybdenum bronze, $H_{0.34}MoO_3$*, *Journal of Solid State Chemistry* **1989**, *83*, 292–303.

[108] F. A. Kröger, H. J. Vink, *Relations between the concentrations of imperfections in crystalline solids*, *Solid state physics* **1956**, *3*, 307–435.

[109] J. M. Polfus, T. Norby, R. Haugsrud, *The defect chemistry of nitrogen in oxides: A review of experimental and theoretical studies*, *Journal of Solid State Chemistry* **2013**, *198*, 65–76.

[110] R. Weber, *Effect of Local Structure on the UV-Visible Absorption Edges of Molybdenum Oxide Clusters and Supported Molybdenum Oxides*, *J. Catal.* **1995**, *151*, 470–474.

[111] M. V. Sivak, A. N. Streletskii, I. V. Kolbanev, A. V. Leonov, E. N. Degtyarev, D. G. Permenov, *Defect structure of nanosized mechanically activated MoO_3*, *Colloid J* **2015**, *77*, 333–340.

[112] M. T. Greiner, L. Chai, M. G. Helander, W.-M. Tang, Z.-H. Lu, *Metal/Metal-Oxide Interfaces: How Metal Contacts Affect the Work Function and Band Structure of MoO_3*, *Adv. Funct. Mater.* **2013**, *23*, 215–226.

[113] L. O. Alemán-Vázquez, E. Torres-García, J. R. Villagómez-Ibarra, J. L. Cano-Domínguez, *Effect of the particle size on the activity of MoO_xC_y catalysts for the isomerization of heptane*, *Catal. Lett.* **2005**, *100*, 219–226.

[114] M. R. Tubbs, *MoO_3 layers — optical properties, colour centres, and holographic recording*, *Phys. Stat. Sol. (a)* **1974**, *21*, 253–260.

[115] S. K. Deb, *Optical Properties and Color-Center Formation in Thin Films of Molybdenum Trioxide*, *J. Appl. Phys.* **1966**, *37*, 4818.

[116] D. Tinet, P. Canesson, H. Estrade, J. J. Fripiat, *Electronic properties of hydrogen molybdenum bronze*, *Journal of Physics and Chemistry of Solids* **1980**, *41*, 583–589.

[117] S. Phadungdhitidhada, P. Mangkorntong, S. Choopun, N. Mangkorntong, *Raman scattering and electrical conductivity of nitrogen implanted MoO_3 whiskers*, *Ceram. Int.* **2008**, *34*, 1121–1125.

[118] M. Shoar Abouzari, F. Berkemeier, G. Schmitz, D. Wilmer, *On the physical interpretation of constant phase elements*, *Solid State Ionics* **2009**, *180*, 922–927.

[119] S. Sunu, E. Prabhu, V. Jayaraman, K. Gnanasekar, T. Seshagiri, T. Gnanasekaran, *Electrical conductivity and gas sensing properties of MoO_3*, *Sensors and Actuators B: Chemical* **2004**, *101*, 161–174.

[120] T. He, J. Yao, *Photochromism of molybdenum oxide*, *Journal of Photochemistry and Photobiology C: Photochemistry Reviews* **2003**, *4*, 125–143.

[121] Z. Zhang, X. E. Verykios, M. Baerns, *Effect of Electronic Properties of Catalysts for the Oxidative Coupling of Methane on Their Selectivity and Activity*, *Catalysis Reviews* **2006**, *36*, 507–556.

[122] J. Zhou, S. Z. Deng, N. S. Xu, J. Chen, J. C. She, *Synthesis and field-emission properties of aligned MoO_3 nanowires*, *Appl. Phys. Lett.* **2003**, *83*, 2653.

[123] A. J. Medford, A. Vojvodic, J. S. Hummelshøj, J. Voss, F. Abild-Pedersen, F. Studt, T. Bligaard, A. Nilsson, J. K. Nørskov, *From the Sabatier principle to a predictive theory of transition-metal heterogeneous catalysis*, *J. Catal.* **2015**, *328*, 36–42.

[124] H. Baussart, R. Delobel, M. Le Bras, J. M. Leroy, *Oxidation of propene on mixed oxides of copper and cobalt*, *J. Chem. Soc., Faraday Trans. 1* **1979**, *75*, 1337.

[125] T. Ressler, R. E. Jentoft, J. Wienold, M. M. Günter, O. Timpe, *In Situ XAS and XRD Studies on the Formation of Mo Suboxides during Reduction of MoO_3*, *J. Phys. Chem. B* **2000**, *104*, 6360–6370.

[126] E. Lalik, W. I. F. David, P. Barnes, J. F. C. Turner, *Mechanisms of Reduction of MoO_3 to MoO_2 Reconciled?*, *J. Phys. Chem. B* **2001**, *105*, 9153–9156.

[127] S. Åsbrink, L. Kihlborg, L. M. Jackman, D. R. Sparrow, *A Study of the Crystal Symmetry and Structure of Orthorhombic Mo_4O_{11} by Least-squares Techniques*, *Acta Chem. Scand.* **1964**, *18*, 1571–1573.

[128] R. Knorr, U. Müller, *h-Mo_4O_{11} und $Mg_2Mo_3O_8$: eine neue Synthese und Verfeinerung ihrer Kristallstrukturen*, *Z. anorg. allg. Chem.* **1995**, *621*, 541–545.

[129] B. G. Brandt, A. C. Skapski, E. Thom, E. Stoll, G. Eriksson, R. Blinc, S. Paušak, L. Ehrenberg, J. Dumanović, *A Refinement of the Crystal Structure of Molybdenum Dioxide*, *Acta Chem. Scand.* **1967**, *21*, 661–672.

[130] H. E. Kissinger, *Variation of peak temperature with heating rate in differential thermal analysis*, *J. Res. Natl. Bur. Stan.* **1956**, *57*, 217.

[131] G. Munteanu, L. Ilieva, D. Andreeva, *Kinetic parameters obtained from TPR data for α-Fe_2O_3 and Au/a-Fe_2O_3 systems*, *Thermochim Acta* **1997**, *291*, 171–177.

[132] C. Chen, *Size Dependence of Structural Metastability in Semiconductor Nanocrystals*, *Science* **1997**, *276*, 398–401.

[133] S. Vyazovkin, C. A. Wight, *Kinetics in solids*, *Annual review of physical chemistry* **1997**, *48*, 125–149.

[134] F. Liu, F. Sommer, C. Bos, E. J. Mittemeijer, *Analysis of solid state phase transformation kinetics: models and recipes*, *International Materials Reviews* **2007**, *52*, 193–212.

[135] M. M. Hossain, S. Ahmed, *Cu-based mixed metal oxide catalysts for WGSR: Reduction kinetics and catalytic activity*, *Can. J. Chem. Eng.* **2013**, *91*, 1450–1458.

[136] J. D. Sewry, M. E. Brown, *“Model-free” kinetic analysis?*, *Thermochim Acta* **2002**, *390*, 217–225.

[137] A. Khawam, D. R. Flanagan, *Solid-state kinetic models: basics and mathematical fundamentals*, *The journal of physical chemistry. B* **2006**, *110*, 17315–17328.

[138] L. Engelke, M. Schaefer, M. Schur, W. Bensch, *In Situ X-ray Diffraction Studies of the Crystallization of Layered Manganese Thioantimonates(III) under Hydrothermal Conditions*, *Chem. Mater.* **2001**, *13*, 1383–1390.

[139] N. Koga, J. M. Criado, *Kinetic Analyses of Solid-State Reactions with a Particle-Size Distribution*, *Journal of the American Ceramic Society* **1998**, *81*, 2901–2909.

[140] M. M. Lin, *Selective oxidation of propane to acrylic acid with molecular oxygen*, *Appl. Catal., A* **2001**, *207*, 1–16.

[141] M. Bettahar, G. Costentin, L. Savary, J. Lavalley, *On the partial oxidation of propane and propylene on mixed metal oxide catalysts*, *Appl. Catal., A* **1996**, *145*, 1–48.

[142] V. K. Sabhapathi, O. M. Hussain, P. S. Reddy, Reddy, K. T. Ramakrishna, S. Uthanna, B. S. Naidu, P. J. Reddy, *Optical absorption studies in molybdenum trioxide thin films*, *Phys. Stat. Sol. (a)* **1995**, *148*, 167–173.

[143] S. Knobl, *The synthesis and structure of a single-phase, nanocrystalline MoVW mixed-oxide catalyst of the Mo_5O_{14} type*, *J. Catal.* **2003**, *215*, 177–187.

[144] R. Schlögl, A. Knop-Gericke, M. Hävecker, U. Wild, D. Frickel, T. Ressler, R. E. Jentoft, J. Wienold, G. Mestl, A. Blume et al., *In situ analysis of metal-oxide systems used for selective oxidation catalysis: how essential is chemical complexity?*, *Top. Catal.* **2001**, *15*, 219–228.

[145] F. Portemer, M. Sundberg, L. Kihlborg, M. Figlarz, *Homologues of Mo_4O_{11}(mon) in the Mo-W-O System Prepared by Soft Chemistry*, *J. Solid State Chem.* **1993**, *103*, 403–414.

[146] Troitskaya, N.V., Pinsker, Z.G, *Kristallografiya* **1959**, 33.

[147] M. A. G. Aranda, E. R. Losilla, A. Cabeza, S. Bruque, *Effective Correction of Peak Asymmetry: Rietveld Refinement of High-Resolution Synchrotron Powder Data of $Li_{1.8}(Hf_{1.2}Fe_{0.8})(PO_4)_3$*, *J. Appl. Crystallogr.* **1998**, *31*, 16–21.

[148] E. Prince, B. H. Toby, *A comparison of methods for modeling the effect of axial divergence in powder diffraction*, *J. Appl. Crystallogr.* **2005**, *38*, 804–807.

[149] A. G. de La Torre, S. Bruque, M. A. G. Aranda, *Rietveld quantitative amorphous content analysis*, *J. Appl. Crystallogr.*, *34*, 196–202.

[150] M. Armand, Arroyo y de Dompablo, M. E., *Benefits of N for O substitution in polyoxoanionic electrode materials: a first principles investigation of the electrochemical properties of $Li_2FeSiO_{4-y}N_y$ (y = 0, 0.5, 1)*, *J. Mater. Chem.* **2011**, *21*, 10026.

[151] G. Williamson, W. Hall, *X-ray line broadening from filed aluminium and wolfram*, *Acta Metall.* **1953**, *1*, 22–31.

[152] N. Gonçalves, J. Carvalho, Z. Lima, J. Sasaki, *Size–strain study of NiO nanoparticles by X-ray powder diffraction line broadening*, *Mater. Lett.* **2012**, *72*, 36–38.

[153] K. Venkateswarlu, A. Chandra Bose, N. Rameshbabu, *X-ray peak broadening studies of nanocrystalline hydroxyapatite by Williamson–Hall analysis*, *Phys. B* **2010**, *405*, 4256–4261.

[154] T. Y. Kardash, D. I. Kochubei, L. M. Plyasova, V. M. Bondareva, *EXAFS study of the local structure and cation distribution in V-Mo-Nb oxide*, *J. Struct. Chem.* **2008**, *49*, 116–123.

[155] M. T. Schulberg, *Aspects of nitrogen surface chemistry relevant to TiN chemical vapor deposition*, *J. Vac. Sci. Technol. A* **1996**, *14*, 3228.

[156] I. A. Bakare, S. A. Mohamed, S. Al-Ghamdi, S. A. Razzak, M. M. Hossain, de Lasa, Hugo I., *Fluidized bed ODH of ethane to ethylene over VO_x–MoO_x/γ-Al_2O_3 catalyst: Desorption kinetics and catalytic activity*, *Chem. Eng. J.* **2014**.

[157] S. G. Ebbinghaus, H.-P. Abicht, R. Dronskowski, T. Müller, A. Reller, A. Weidenkaff, *Perovskite-related oxynitrides – Recent developments in synthesis, characterisation and investigations of physical properties*, *Prog. Solid State Chem.* **2009**, *37*, 173–205.

[158] D. Haskel, Z. Islam, J. Lang, C. Kmety, G. Srajer, K. Pokhodnya, A. Epstein, J. Miller, *Local structural order in the disordered vanadium tetracyanoethylene room-temperature molecule-based magnet*, *Phys. Rev. B* **2004**, *70*.

[159] F. Cariati, J. Bart, A. Sgamellotti, *Spectroscopic analysis of mixed valence molybdenum oxides*, *Inorg. Chim. Acta* **1981**, *48*, 97–103.

[160] S. Ishikawa, T. Murayama, S. Ohmura, M. Sadakane, W. Ueda, *Synthesis of Novel Orthorhombic Mo and V Based Complex Oxides Coordinating Alkylammonium Cation in Its Heptagonal Channel and Their Application as a Catalyst*, *Chem. Mater.* **2013**, *25*, 2211–2219.

[161] P. Botella, *The Preparation, Characterization, and Catalytic Behavior of MoVTeNbO Catalysts Prepared by Hydrothermal Synthesis*, *J. Catal.* **2002**, *209*, 445–455.

[162] R. B. Watson, U. S. Ozkan, *Propane and propylene adsorption effects over MoO_x-based catalysts induced by low levels of alkali doping*, *J. Mol. Catal. A: Chem.* **2003**, *194*, 115–135.

[163] X. Wang, L. Andrews, R. Lindh, V. Veryazov, B. O. Roos, *A Combined Theoretical and Experimental Study of Simple Terminal Group 6 Nitride and Phosphide $N{=}MX_3$ and $P{=}MX_3$ Molecules*, *J. Phys. Chem. A* **2008**, *112*, 8030–8037.

[164] A. Pantazidis, A. Auroux, J.-M. Herrmann, C. Mirodatos, *Role of acid—base, redox and structural properties of VMgO catalysts in the oxidative dehydrogenation of propane*, *Catal. Today* **1996**, *32*, 81–88.

[165] L. Y. Margolis, A. A. Firsova, *Modification of catalysts*, *Int. Rev. Phys. Chem.* **2008**, *8*, 1–20.

[166] M. Ram, *Synthesis and electrical properties of $(LiCo_{3/5}Fe_{1/5}Mn_{1/5})VO_4$ ceramics*, *Solid State Sciences* **2010**, *12*, 350–354.

[167] A. K. Jonscher, *The 'universal' dielectric response*, *Nature* **1977**, *267*, 673–679.

[168] C. Sekar, R. K. Selvan, S. T. Senthilkumar, B. Senthilkumar, C. Sanjeeviraja, *Combustion synthesis and characterization of spherical α-$MnMoO_4$ nanoparticles*, *Powder Technol.* **2012**, *215-216*, 98–103.

[169] F. Sallemi, B. Louati, K. Guidara, *Electrical conductivity and dielectric behavior in sodium zinc divanadates*, *Phys. B* **2014**, *452*, 142–147.

[170] A. Simon, E. V. Kondratenko, *Investigation of the electrical and catalytic properties of materials with $Cs_x(Mo,Nb)_5O_{14}$ composition*, *Appl. Catal., A* **2011**, *392*, 199–207.

[171] S. Nakhal, W. Hermes, T. Ressler, R. Pöttgen, M. Lerch, *Synthesis, Crystal Structure, and Magnetic Properties of a Vanadium Oxide Nitride with Pseudobrookite-type Structure*, *Z. anorg. allg. Chem.* **2009**, *635*, 2016–2020.

[172] K. Lai, Y. Zhu, J. Lu, Y. Dai, B. Huang, *N- and Mo-doping Bi_2WO_6 in photocatalytic water splitting*, *Computational Materials Science* **2013**, *67*, 88–92.

[173] F. Cavani, F. Trifirò, *Selective oxidation of light alkanes: interaction between the catalyst and the gas phase on different classes of catalytic materials*, *Catal. Today* **1999**, *51*, 561–580.

[174] T. Ressler, *Application of time-resolved in-situ X-ray absorption spectroscopy in solid-state chemistry*, *Anal. Bioanal. Chem.* **2003**, *376*, 584–593.

[175] T. Franzke, F. Rosowski, M. Muhler, *Redox-Zyklen zur Charakterisierung von Modellkatalysatoren für die selektive Propenoxidation*, *Chem. Ing. Tech.* **2011**, *83*, 1705–1710.

[176] L. F. Liotta, M. Ousmane, G. Di Carlo, G. Pantaleo, G. Deganello, G. Marcì, L. Retailleau, A. Giroir-Fendler, *Total oxidation of propene at low temperature over Co_3O_4–CeO_2 mixed oxides: Role of surface oxygen vacancies and bulk oxygen mobility in the catalytic activity*, *Appl. Catal., A* **2008**, *347*, 81–88.

[177] T. Ressler, J. Wienold, R. E. Jentoft, *Formation of bronzes during temperature-programmed reduction of MoO_3 with hydrogen—an in situ XRD and XAFS study*, *Solid State Ionics* **2001**, *141-142*, 243–251.

[178] M. Olea, M. Florea, I. Sack, R. Pradasilvy, E. Gaigneaux, G. Marin, P. Grange, *Evidence for the participation of lattice nitrogen from vanadium aluminum oxynitrides in propane ammoxidation*, *J. Catal.* **2005**, *232*, 152–160.

[179] J. Haber, W. Turek, *Kinetic Studies as a Method to Differentiate between Oxygen Species Involved in the Oxidation of Propene*, *J. Catal.* **2000**, *190*, 320–326.

[180] R. Zubrzycki, J. D. Epping, T. Ressler, *Role of Vanadium and Phosphorus in Substituted Keggin-Type Heteropolyoxo Molybdates Supported on Silica SBA-15 in Selective Propene Oxidation*, *ChemCatChem* **2015**, *7*, 1112–1121.

[181] A. N. Desikan, W. M. Zhang, S. T. Oyama, *The Effect of Acid-Base Properties of Supported Molybdenum Oxide in Propylene Oxidation*, *J. Catal.* **1995**, *157*, 740–748.

[182] J. Scholz, A. Walter, T. Ressler, *Influence of MgO-modified SBA-15 on the structure and catalytic activity of supported vanadium oxide catalysts*, *J. Catal.* **2014**, *309*, 105–114.

[183] E. Heracleous, *Surface Properties and Reactivity of Al_2O_3-Supported MoO_3 Catalysts in Ethane Oxidative Dehydrogenation*, *Catal. Lett.* **2003**, *88*, 47–53.

[184] H. Liu, *Structure and support effects on the selective oxidation of dimethyl ether to formaldehyde catalyzed by MoO_x domains*, *J. Catal.* **2003**.

10 Table captions

11 Appendix

A1 Characterization of ball-milled MoO_3 and its oxide nitrides

Table A 1-1: *Results of Rietveld refinements of ball-milled MoO_3.*

	MO	MO60	MO120	MO180	MO240
a / Å	3.9618(1)	3.9632(1)	3.9622(1)	3.9630(1)	3.9621(1)
b / Å	13.8593(3)	13.8656(3)	13.8688(3)	13.8673(4)	13.8661(4)
c / Å	3.6964(1)	3.6979(1)	3.6968(1)	3.6971(1)	3.6965(1)
V / Å^3	203.0	203.2	203.1	203.2	203.1
GOF	1.4	1.2	1.2	1.4	1.4
Chi^2	2.0	1.7	1.5	1.9	2.0

Table A 1-2: *Results of Rietveld refinements of MoO_3-type oxide nitrides with various crystallinity.*

	MON	MON60	MON120	MON180	MON240
a / Å	3.9619(1)	3.9632(1)	3.9604(1)	3.9599(1)	3.9583(1)
b / Å	13.8630(5)	13.8656(4)	13.8857(4)	13.8768(5)	13.8872(6)
c / Å	3.6995(1)	3.6994(1)	3.6977(1)	3.6979(1)	3.6983(1)
V / Å^3	203.2	203.2	203.3	203.2	203.3
GOF	1.3	1.4	1.6	1.3	1.4
Chi^2	1.6	1.9	2.4	2.0	1.8

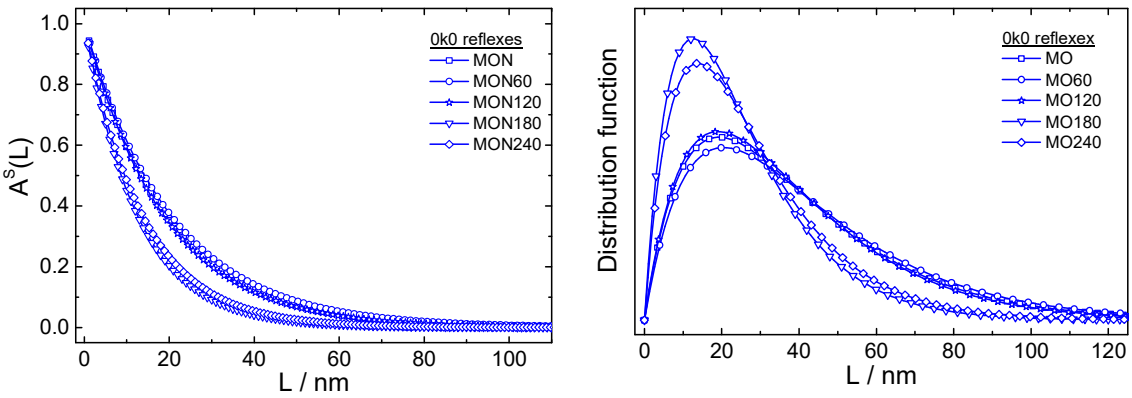

Figure A 1-1: *Left: Size Fourier coefficients as a function of column length calculated from 0k0 diffraction peaks. Right: Distribution function of averaged distances in real space of MoO_3-type oxide nitrides from 0k0 diffraction peaks.*

Table A 1-3: *Positions and assignments of FTIR bands of ball-milled MoO_3 and its corresponding oxide nitrides [102,103].*

	δOMo₂	δOMo₃	δOMo₃	δOMo₃	δO=Mo	νOMo₃	νOMo₃	νOMo₂	νOMo₂	νO=Mo
MO	228	300	330	350	375	487	598	818	867	989
MON	227	296	327	349	374	485	595	817	866	989
MO60	228	301	331	351	376	485	603	819	875	989
MON60	227	299	328	350	375	483	602	816	873	991
MO120	227	301	330	351	376	484	603	818	876	989
MON120	227	300	329	350	375	481	602	817	874	989
MO180	226	301	328	350	374	484	604	818	879	989
MON180	226	298	328	350	371	478	604	817	876	989
MO240	227	300	330	351	376	481	605	817	877	989
MON240	226	298	327	350	374	477	604	817	873	987

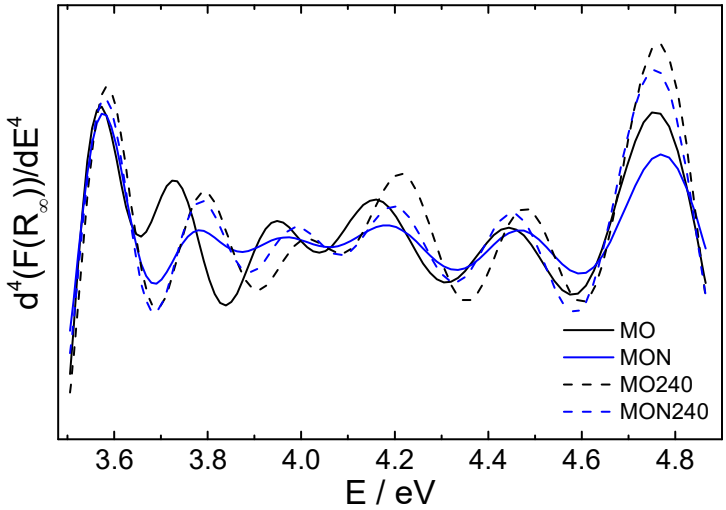

Figure A 1-2: *Fourth derivation of DR/UV-Vis spectra of non-milled MoO_3, MO240 and its corresponding oxide nitrides.*

A2 Reducibility ball-milled molybdenum oxides and oxide nitrides

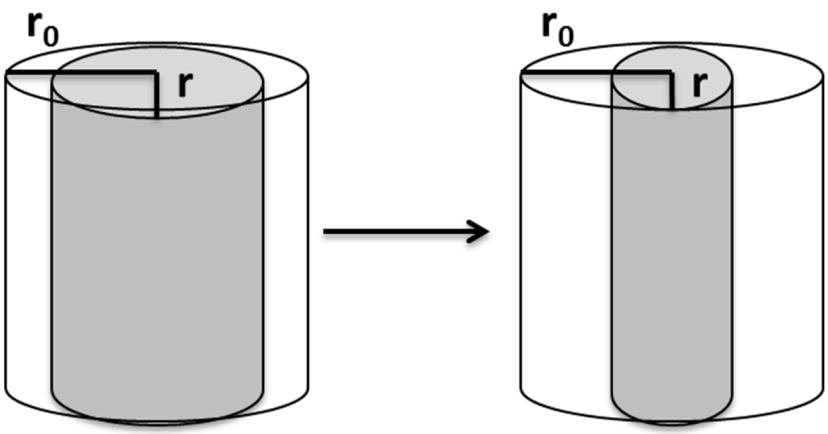

Figure A 2-1: *Schematic presentation of cylindrical particle shape according to contracting are model (R2) and assumed progress during reaction.*

A3 Characterization of mixed molybdenum oxide nitrides

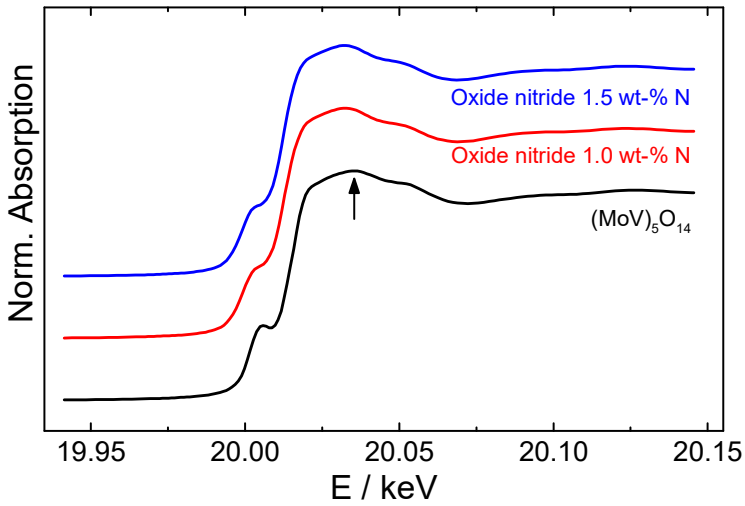

Figure A 3-1: *Normalized Mo-XANES spectra of $(MoV)_5O_{14}$ and two oxide nitrides with different nitrogen contents at 298 K.*

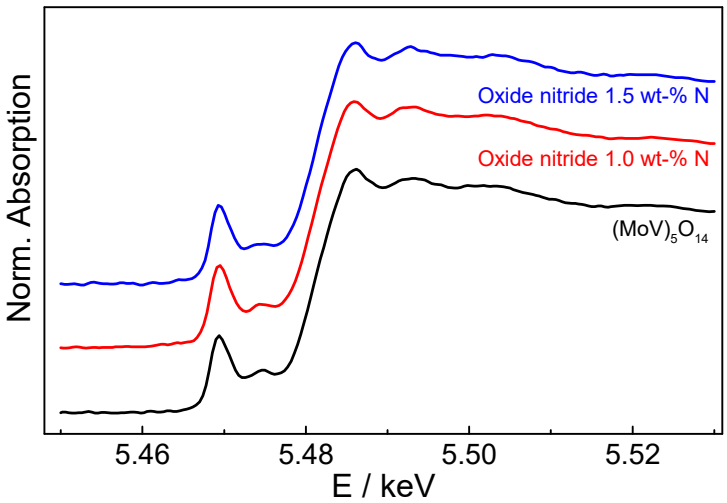

Figure A 3-2: *Normalized V-XANES spectra of $(MoV)_5O_{14}$ and two oxide nitrides with different nitrogen contents at 298 K.*

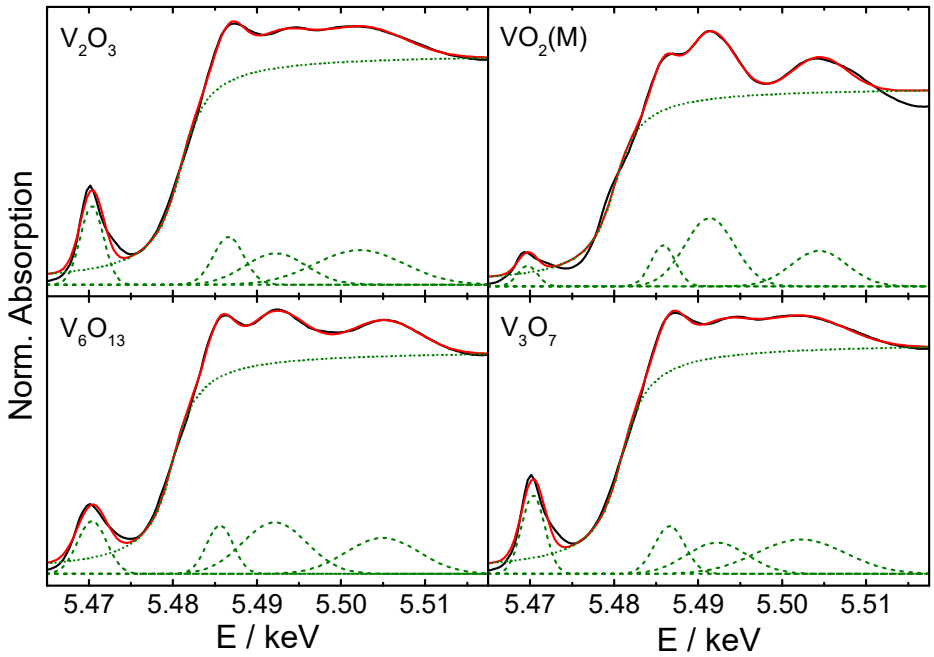

Figure A 3-3: *Refinements of XANES data for V K edge using four Gaussian functions and one arctangent function of vanadium oxide references.*

A4 *In situ* characterization of mixed molybdenum oxide nitrides

Table A 4-1: *Type, number (N), and XAFS disorder parameter (σ^2) of atoms at a distance R from the Mo atoms in reduced $(MoV)_5O_{14}$ and oxide nitrides with different nitrogen contents. Experimental distances and disorder parameters were obtained from refinement of a monoclinic MoO_2 model structure (k range from 3 to 14 $Å^{-1}$, R range from 1.07 to 3.96 Å, N_{ind} =10 , N_{free} = 3 - 10)*

Type	Oxide			Oxide nitride 1 wt.-% N			Oxide nitride 1.5 wt.-% N		
	N	R / Å	σ^2 / Å²	N	R / Å	σ^2 / Å²	N	R / Å	σ^2 / Å²
Mo-O	2_f	1.952	0.00138_c	2_f	1.952	0.00149_c	2_f	1.951	0.00159_c
Mo-O	2_f	1.992	0.00138_c	2_f	1.990	0.00149_c	2_f	1.992	0.00159_c
Mo-O	2_f	2.054	0.00138_c	2_f	2.054	0.00149_c	2_f	2.053	0.00159_c
Mo-Mo	1_f	2.531	0.00138_c	1_f	2.530	0.00149_c	1_f	2.529	0.00159_c
Mo-Mo	1_f	3.116	0.00473	1_f	3.114	0.00498	1_f	3.116	0.00512
Mo-Mo	6_f	3.710	0.00217_C	6_f	3.708	0.00241_C	6_f	3.707	0.00265_C
Mo-Mo	2_f	3.885	0.00217_c	2_f	3.887	0.00241_c	2_f	3.887	0.00265_c
Residual	6.4			6.3			6.2		
E_0 / eV	-1.63			-1.49			-1.81		

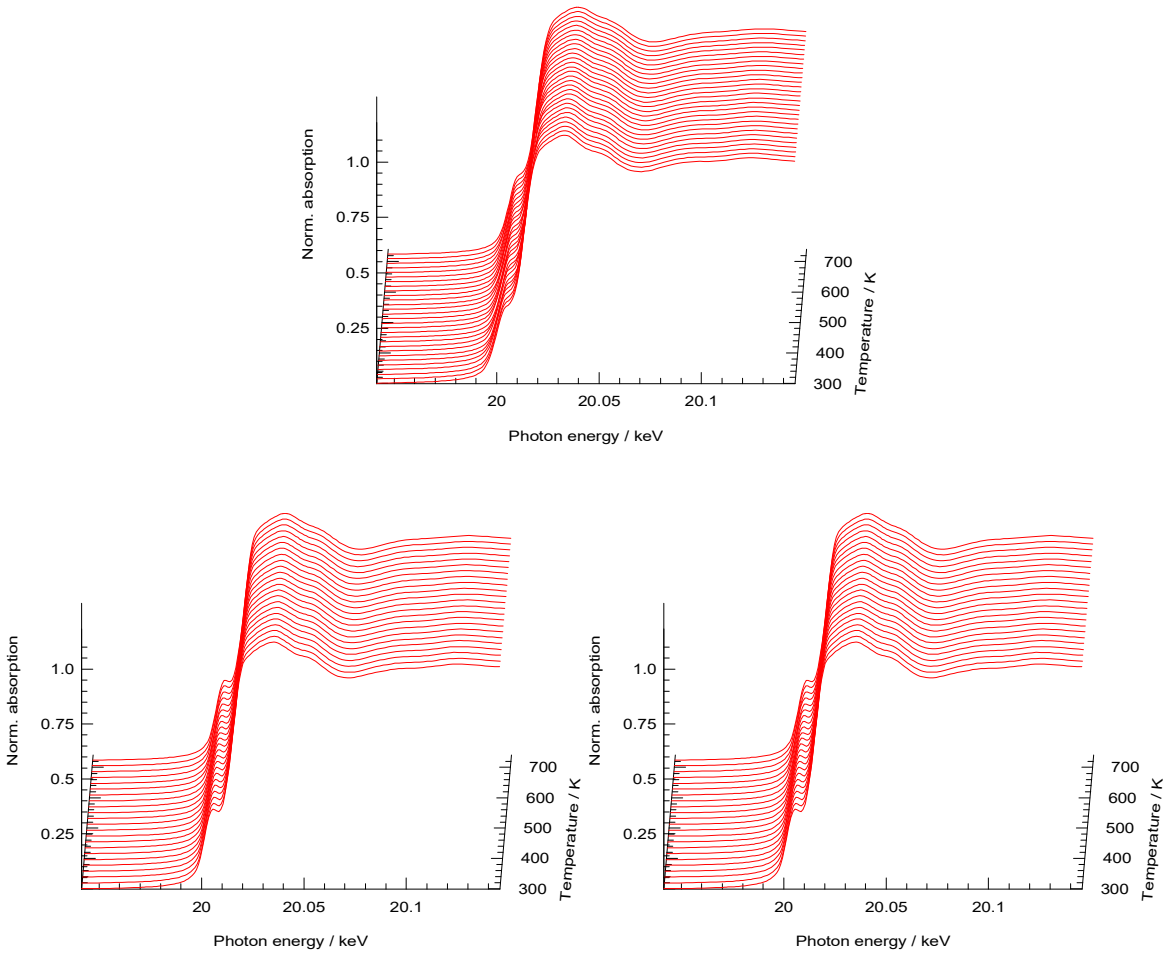

Figure A 4-1: *Evolution of XANES spectra of $(MoV)_5O_{14}$ (top) and (MoV) oxide nitrides with 1.0 (bottom, left) and 1.5 wt% (bottom, right) N during treatment (5% propene, 5% oxygen in helium) in a temperature range from 300 K to 723 K.*

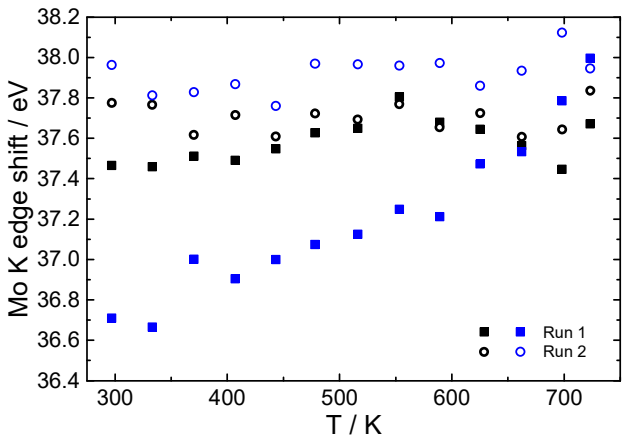

Figure A 4-2: *Evolution of relative Mo K edge position during treatment of non-milled MoO_3 and its corresponding oxide nitride in 5% propene, 5% oxygen in helium up to 723 K.*

Epilogue

Publications

S. Kühn, D. Weber, M. Lerch, T. Ressler, Effects of anion substitution in $(Mo,V)_5O_{14}$ on catalytic performance in selective propene oxidation to acrolein, ChemCatChem ***2016****, 8, 758-766.*

S. Kühn, D. Weber, M. Lerch, T. Ressler, Preparation of (Mo, V) Oxide Nitrides with Mo_5O_{14} Structure as Model Catalysts for Selective Propene Oxidation, Z. anorg. allg. Chemie ***2012****, 638, 1587.*

S. Kühn, P. Schmidt-Zhang, A.H.P. Hahn, M. Huber, M. Lerch, T. Ressler, Structure and properties of molybdenum oxide nitrides as model systems for selective oxidation catalysts, Chemistry Central Journal ***2011****, 5, 42.*

S. Kühn, A. Stys, P. Schmidt-Zhang, M. Huber, S. Berendts, M. Lerch, T. Ressler, Structure and reactivity of molybdenum oxide nitrides as selective oxidation catalysts, Z. anorg. allg. Chemie ***2010****, 636, 2097.*

Talks

S. Kühn, D. Weber, M. Lerch, T. Ressler, Effects of anion substitution in $(MoV)_5O_{14}$ on catalytic performance in selective oxidation of propene to acrolein, Tag der Chemie, June 18th ***2015****, Berlin, Germany.*

S. Kühn, D. Weber, M. Lerch, T. Ressler, Effects of anion substitution in $(MoV)_5O_{14}$ on catalytic performance in propene oxidation to acrolein, 4. Berliner Chemie Symposium (GDCh, JCF), April 9th ***2014****, Berlin, Germany.*

Poster

S. Kühn, D. Weber, M. Lerch, T. Ressler, Effects of anion substitution in $(MoV)_5O_{14}$ on catalytic performance in selective oxidation of propene to acrolein, Tag der Chemie, June 18th ***2015****, Berlin, Germany.*

S. Kühn, D. Weber, M. Lerch, T. Ressler, Effects of anion substitution in $(MoV)_5O_{14}$ on catalytic performance in propene oxidation to acrolein, 48. Jahrestreffen Deutscher Katalytiker, March 11th-13th ***2015****, Weimar, Germany.*

M. Diekmann, S. Kühn, M. König, G. Koch, T. Ressler, Structural and functional characterization of CuO/SBA-15 for selective oxidation of propene, 48. Jahrestreffen Deutscher Katalytiker, March 11th-13th ***2015****, Weimar, Germany.*

S.Kühn, C.D. Feldt, S. Orthmann, M. Lerch, T. Ressler, In situ characterization of mechanically treated MoO_3 and its oxide nitrides as model catalysts for selective propene oxidation, 22nd Annual Conference of the German Crystallographic Society (DGK), March 17th-20th ***2014****, Berlin, Germany.*

S. Kühn, D. Weber, M. Lerch, T. Ressler, Catalytic performance of (Mo,V) oxide nitrides with Mo_5O_{14} structure in selective propene oxidation, 47. Jahrestreffen Deutscher Katalytiker, March 12th-14th ***2014****, Weimar, Germany.*

S. Kühn, D. Weber, M. Lerch, T. Ressler, (Mo,V) oxide nitrides with Mo_5O_{14} structure prepared by ammonolysis as model catalysts for selective propene oxidation, 46. Jahrestreffen Deutscher Katalytiker, March 13th-15th ***2013****, Weimar, Germany.*

S. Kühn, D. Weber, M. Lerch, T. Ressler, Preparation of (Mo, V) Oxide Nitrides with Mo_5O_{14} Structure as Model Catalysts for Selective Propene Oxidation, 16. Vortragstagung der Fachgruppe Festkörperchemie und Materialforschung (GDCh), September 17th-19th ***2012****, Darmstadt, Germany.*

S. Kühn, M. Huber, M. Lerch, T. Ressler, Influence of mechanical activation on the reactivity of molybdenum trioxide, 45. Jahrestreffen Deutscher Katalytiker, March 14th-16th ***2012****, Weimar, Germany.*

S. Kühn, M. Huber, M. Lerch, T. Ressler, Structure and reactivity of molybdenum oxide nitrides as selective oxidation catalysts, 44. Jahrestreffen Deutscher Katalytiker, March 16th-18th ***2011****, Weimar, Germany.*

S. Kühn, A. Stys, P. Schmidt-Zhang, M. Huber, S. Berendts, M. Lerch, T. Ressler, Structure and reactivity of molybdenum oxide nitrides as selective oxidation catalysts, 15. Vortragstagung der Fachgruppe Festkörperchemie und Materialforschung (GDCh), September 20th-22nd ***2010****, Berlin, Germany.*

Danksagung

Ich bedanke mich bei Herrn Prof. Dr. Thorsten Ressler für die interessante wissenschaftliche Thematik und die Möglichkeit diese selbstständig zu bearbeiten. Insbesondere danke ich ihm auch für die exzellente fachliche Betreuung während der gesamten Zeit meiner Forschungstätigkeit in seinem Arbeitskreis. Ich danke außerdem Herrn Prof. Dr. Peter Strauch für die Anfertigung des Zweitgutachtens und Herrn Dr. Thomas Friedrich für die Übernahme des Vorsitzes im Promotionsausschuss.

Mein besonderer Dank gilt der gesamten Arbeitsgruppe Ressler die angenehme und freundliche Arbeitsatmosphäre. Ich danke vor allem Dr. Gregor Koch, Dr. Alexander Müller, Dr. Rafael Zubrzycki und Dr. Juliane Scholz für ihre stete Diskussionsbereitschaft und Zusammenarbeit bei der Durchführung von Experimenten und Messzeiten. Ein weiter Dank gilt Alexander Hahn und Dr. Thomas Christoph Rödel für die technische Unterstützung bei zahlreichen Experimenten. Semiha Schwarz möchte ich für ihre zahlreichen Ratschläge danken. Besonders bedanken möchte ich mich auch bei Dr. Peter Schmidt-Zhang und Dr. Anke Walter, die mich im Rahmen meines Forschungspraktikums und meiner Diplomarbeit in viele Methoden der instrumentellen Analytik eingearbeitet und betreut haben. Ebenso möchte ich mich für die Unterstützung im Rahmen ihrer Bachelorarbeiten und Praktika bedanken bei Maika Stöbe, Christoph David Feldt, Nina Sharmen Genz, Gökhan Kurt, Marek Diekmann und Michaela König.

Dem gesamten Arbeitskreis Lerch danke ich für die Aufnahmen der Weitwinkelbeugungsdaten. Insbesondere möchte ich Dr. Dominik Weber, Dr. Suliman Nakhal sowie Steven Orthmann für die Unterstützung bei der Synthese der verwendeten Proben danken. Zu Dank verpflichtet bin ich auch allen anderen Mitgliedern des Instituts für Chemie der TU Berlin, die mich bei meiner Arbeit unterstützt haben.

Dem DESY und dem HASYLAB in Hamburg sei für die Bereitstellung zahlreicher Messzeiten gedankt. Bei der Deutschen Forschungsgemeinschaft (DFG) bedanke ich mich für die finanzielle Unterstützung.

Ich danke meiner Familie und meinen Freunden Kerstin, Timo, Katharina, Haiko und Anna für den steten Rückhalt neben dem Forschungsalltag und die uneingeschränkte Unterstützung in allen Phasen der Entstehung dieser Arbeit.

Eidesstattliche Erklärung

Hiermit versichere ich an Eides statt, dass ich die vorliegende Arbeit selbstständig verfasst und keine anderen als die in der Dissertation angegebenen Quellen und Hilfsmittel benutzt habe. Alle Ausführungen, die anderen veröffentlichten oder nicht veröffentlichten Schriften wörtlich oder sinngemäß entnommen wurden, habe ich kenntlich gemacht.

Die Arbeit hat in gleicher oder ähnlicher Fassung noch keiner anderen Prüfungsbehörde vorgelegen.

_____ _____

Ort, Datum Unterschrift